SURFACE OPTOFLUIDIC IMPLEMENTATIONS

TOWARDS THE DEVELOPMENT OF A BIOSENSOR

Thesis by

Jae-Woo Choi

In Partial Fulfillment of the Requirements

for the Degree of

Doctor of Philosophy

California Institute of Technology

Pasadena, California

2011

(Defended March 16, 2011)

Acknowledgements

First, I would like to thank my advisor, Demetri Psaltis. I am indebted to him for accepting me into the group when I had very little experience in experimental optics. I learned a lot about research as well as life and he knew when to inspire confidence and crack jokes along with the occasional motivational speeches. I benefited greatly from his vision and creativity and I was very lucky to be in such an exciting intellectual environment.

Within the lab, there are several members who acted as mentors and as good friends. James Adleman was one of the first members that I learned a lot from, who was always available for extensive discussions. Allen Pu taught me the ways of being a good doctoral student in the group and I am extremely grateful for his guidance during my early years. Mathias Dietzel, who was extremely patient with regards to all my questions regarding fluidics. Chia-Lung Hsieh, a good friend who always knew the right questions to ask. I also acknowledge the many discussions with Wuzhou Song, the endless of enthusiasm of Rachel Grange and the infinite curiosity of Xin Yang. Additionally, I cannot forget research undergraduate/masters students, Philip Munoz, Grace Cheung, Daniel Yanisse and Gregoire Laporte, for whom I tried to emphasize the enjoyment of the research process. I cannot forget Yayun Liu, who kept the lab equipment running and told me on the first day to not be intimidated. Very special thanks to Lucinda Acosta, her amazing administrative skills and enthusiastic personality. She could make a gloomy day become sunny with her positive attitude. I would like to acknowledge my various discussions with Martin Centurion, David Erickson, Troy Rockwood, Mankei Tseng, Ye

Pu, Zhenyu Li, Fai Mok, Ted Dikaliotis, Christos Santis, Shai Barak, Helge Eggert, Felix Kuhnert, Andreas Vasdekis, Kostas Makris, Ioannis Papadopoulous, Hang Xu, Alexandre Goy, Julien Cuennet, and Jianhang Yang. And our administrative assistant, Carole Berthet, who acts like a mother and worries about us, helping us get medicine when we are sick with a cold.

I would also like to thank my collaborators: Herb Shea and his group, especially Samuel Rosset, Muhamed Niklaus and Luc Maffli, provided valuable technology for the microfluidic devices; and Karsten Buse and his group, especially Daniel Schutze and Bastian Knabe, for providing valuable insight into lithium niobate.

I don't think I can acknowledge all the people whose friendship was valuable during my studies: Caltech ultimate frisbee, the Ballistic Photons, the Caltech Korean graduate students association and the various athletic events especially the weekly Wednesday evening tennis group. In Lausanne, the Flyhigh ultimate club who served as a means of practicing my French every week.

Finally, I'd like to acknowledge my parents. My mother has always been there and loves me unconditionally. My father, a big idol in my life, I am forever grateful for his constant support and gentle nudging towards things that pique my interest.

Abstract

Microfluidics is a multidisciplinary field that uses minute volumes of liquids to attempt complex functionalities. These complicated functionalities often require manipulating interfaces through external forces. In addition, optics have become a fundamental necessity for most microfluidic devices. We combine these two concepts and call it surface optofluidics. Here, we focus on the advantages of surface optofluidics for the development of a biosensor, specifically focusing on the flexibility and adaptability offered by these techniques.

To introduce the advantages presented by surface optofluidics, devices using droplet electrowetting techniques are discussed. We then discuss biosensing through structured electrodes on surfaces. The electrodes are used to align asymmetric bacteria. The aligned bacteria are detected optically. This method of detection is improved by incorporating two different surface optofluidic methods. Concentration and motion control of the bacterium is demonstrated with electric fields on three dimensionally structured electrodes and an optothermal nanoparticle carpet. Finally, we show preliminary work in the study of single bacterium behavior using nanoparticles as labels to detect its specific alignment in space.

Table of Contents

Table of Figures

I. Introduction

A. Biosensing

Biosensing requires the interaction of a biological or chemical sample of interest within a testing device. These devices are used to provide information to the user about the analyte. Current development focuses on miniaturization of devices, resulting in lab-on-a-chip devices. A lab-on-a-chip device is a few square millimeters-to-centimeters in size and can perform biological and chemical experiments performed normally in a fully functional laboratory [1]. Integration of several biological and chemical reactions into microfluidic systems has resulted in commercial devices of varying success in daily life, such as pregnancy tests [2]. These tests start by looking at key biochemical markers in urine that indicate whether pregnancy may have occurred. As these markers become functionalized, a color change occurs which results in the end user determining the result of the test in an optical manner. An example of a prototypical pregnancy test is shown in Figure 1. It integrates fluidics and optics, a topic called optofluidics [3].

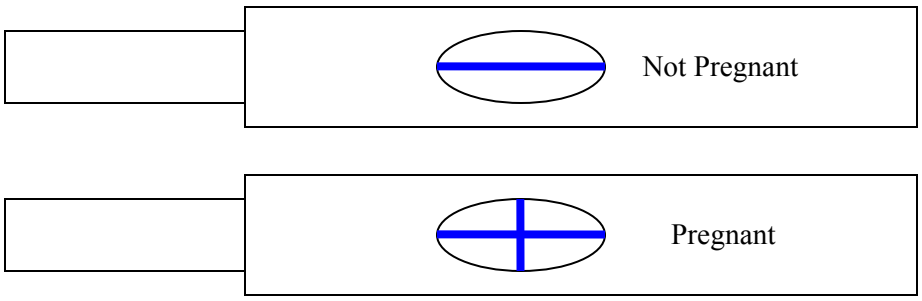

Figure 1. A prototypical lab-on-a-chip device. The image shown above is a diagram of the inner workings of a typical pregnancy test [2]. Fluid is placed onto the left-hand side of the device. The fluid moves into the detection window in the middle of the device. A specific chemical is detected in the urine at the detection window which results in an optical change in the detection window from white to colored (a single line to a crossed line).

B. Optofluidics

The motivation for the development of optofluidics comes from the integration of fluidics into traditional optical devices. Optimal performance of these devices within a changing fluidic environment requires the ability to adapt. The reconfiguration within the fluidics of the devices occurs due to external forces and results in an optical and/or fluidic modification within the device.

In a general sense, optofluidics can be classified into three categories. First, an external means of control modifies the fluid. The fluid modification results in a changing optical property of the device. Second, optical means are used to control the fluid. Finally, external means of control for either the optics or fluids are integrated directly within a microfluidic structure. In this case, the structuring of the microfluidics becomes a key component of the device. Typical optofluidic devices include on-chip dye lasers [4], microscopes [5], sensors [6], mass transport [7], and catalysis [8]. In each of these examples of optofluidics, surfaces play a key role as a means of delivering external control.

C. Surface optofluidics

Surfaces in optofluidic devices have a significant impact on their biological, chemical, mechanical and electrical properties [9]. Within this thesis, we will narrow our topics to three specific types of surfaces. First, we discuss surface coatings that can change the wetting properties for specific liquids [10]. Second, microstructuring of electrodes is a method to define the external control of the device. Lastly, monolayers are a simple method of coating substrates or fluidic channels with plasmonic nanoparticles [8] or biological/chemical compounds [11].

First, droplet electrowetting serves as an example of surface optofluidics. Teflon, a fluorinated substrate, can be used to make the surface hydrophobic. For polar liquids like water, an electrode can be used to change the wetting properties and decrease the contact angle. Devices with adaptable optical properties using electric fields are shown.

Next, microstructuring is a technique that is readily compatible to mass production. Structured electrodes can be used for various purposes. Applying electric fields allows the user to align and attract/repel samples of interest by taking advantage of the difference in the dielectric permittivity between the sample and the media. Bacteria manipulation such as detection, alignment, and concentration are critical to the development of a biosensor.

Finally, a monolayer is used to define optothermal converters. When a laser light shines upon plasmonic nanoparticles resonant at that specific wavelength of light, they generate heat. Within a fluidic environment, the heat causes the liquid to undergo vapor

pressure differences. Fluidic manipulation such as distillation, switching, bidirectional flow, and chemical gradient generation are used within the context of bacteria manipulation.

D. Thesis organization

The thesis is organized as follows: Chapter II focuses on droplet electrowetting and its potential usages in biological and chemical multiplexing and sensing; Chapter III focuses on bacteria detection by optical scattering and using patterned electrodes to align the bacteria; Chapter IV focuses on plasmonic nanoparticles on the surfaces to act as thermal sources when laser light resonant at the wavelength is used, and its integration to bacteria motion control; and Chapter V focuses on using second harmonic nanoparticles and their applicability to long term bacterial experiments.

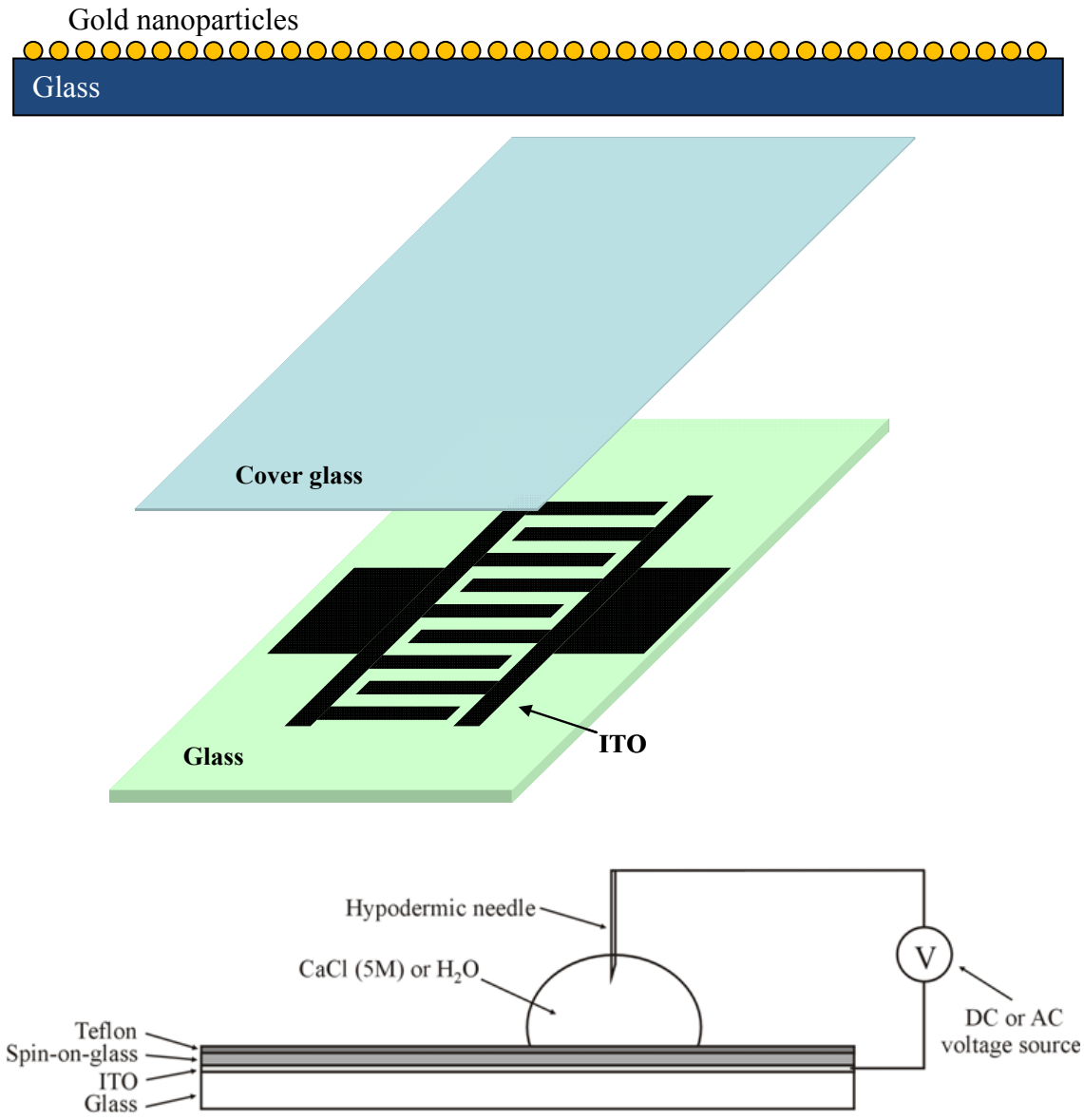

Figure 2. Three different forms of modified surfaces for optofluidics. On top, there is nanostructuring using self-assembled gold nanoparticles on a glass substrate. In the middle, there is microstructuring of electrodes on glass slides using photolithography. And on the bottom, there is changing of surface wetting properties using different materials.

E. References

1. Andersson H, van den Berg A. Microfluidic devices for cellomics: a review. Sensors and Actuators B: Chemical 92, 315–325 (2003).
2. Clearblue Easy +/- Results Pregnancy Test with color change tip, http://www.clearblue.com.
3. Psaltis D, Quake SR, Yang CH. Developing optofluidic technology through the fusion of microfluidics and optics. Nature 442, 381–386 (2006).
4. Song W, Vasdekis AE, Li ZY, Psaltis D. Low order distributed feedback optofluidic dye laser with reduced threshold. Applied Physics Letters 94, 051117 (2009).
5. Heng X, Erickson D, Baugh LR, Yaqoob Z, Sternberg PW, Psaltis D, Yang CH. Optofluidic microscopy — a method for implementing a high resolution optical microscope on a chip. Lab on a Chip 6, 1274–1276 (2006).
6. Lim C, Hong J, Chung BG, deMello AJ, Choo J. Optofluidic platforms based on surface-enhanced Raman scattering. The Analyst 135, 837–844 (2010).
7. Liu GL, Kim J, Lu Y, Lee LP. Optofluidic control using photothermal nanoparticles. Nature Materials 5, 27–32 (2006).
8. Adleman JR, Boyd DA, Goodwin DG, Psaltis D. Heterogeneous catalysis mediated by plasmon heating. Nano Letters 9, 4417–4423 (2009).
9. Vasdekis AE, Cuennet JG, Song W, Choi JW, De Sio L, O'Neil CP, Hubbell JA, Psaltis D. Surface optofluidics. Proceedings of SPIE 7762, 776224 (2010).
10. Choi SK, Moon H, Kim CJ. Creating, transporting, cutting and merging liquid droplets by electrowetting based actuation for digital microfluidic circuits. Journal of Microelectromechanical Systems 12, 70–80 (2003).
11. Vasdekis AE, O'Neil CP, Hubbell JA, Psaltis D. Microfluidic assays for DNA manipulation based on block copolymer immobilization strategy. Biomacromolecules 11, 827–831 (2010).

II. Electrowetting

A. Introduction

An example of optofluidics is the application of electrical forces to modify liquids resulting in a change of the optical property. Examples of devices with transitory behavior due to electrical forces are a ubiquitous component of our lives. A primary example is display devices: rotating turnstile bi-stable billboards, light emitting diodes, and liquid crystal displays. In this section, we look at changing the hydrophobicity of a surface by applying electric fields. These devices act as a means of controlling the light source.

1. Electrowetting

In 1875, Gabriel Lippmann described the behavior of metallic and polar liquids on surfaces with various charges. This effect of changing the wetting behavior of liquids on surfaces with an applied electric field is called electrowetting. This technique can be used for varying optical properties and is appropriate to the concept of surface optofluidics. The liquid itself is modified by the applied electric fields on the surface and results in varying optical properties of the device. A simple example of electrowetting is shown in Figure 3 and Figure 4.

The electrowetting effect is maximized by having a superhydrophobic surface while using an extremely polar liquid, as shown in Figure 5. [1] This is due to the fact that the applied electric field causes a change in the equilibrium solid-liquid-air contact angle. This change is maximized if the contact angle is extremely large to begin with, as an applied electric field can only decrease this contact angle. That is, the contact angle due to an applied electric field goes from a phobic state to a philic state for most surfaces. Therefore, most electrowetting devices utilize amorphous fluoropolymers such as Cytonix, CYTOP (Asahi), and Teflon AF (DuPont).

A rough explanation of the relationship between surface tension and contact angle before saturation voltage is given below [2]:

$$\gamma_{ws} = \gamma_{ws}^{0} - \frac{CV^2}{2}.$$

The equation relates the change in surface tension by an applied electric field. γ_{ws} describes the surface tension between the solvent (w for water), the substrate (s for solid), and the surrounding air. Without an applied electric field, there is an initial surface tension state. This can be thought of as the phobic state where the solvent prefers to remain together and minimize its surface area with the substrate. This initial state is described in the following equation. Increasing the applied electric field results in a decrease of surface tension. Therefore, the solvent will relax and gradually increase its contact area with the substrate.

$$\gamma_{ws} = \gamma_s + \gamma_w \cos(\theta)$$

This equation relates the contact angle at the interface between the solvent, substrate, and air to the surface tensions between each component. The surface tension is dependent on the preference of the solvent and the substrate. For phobic substrates, the substrate has a certain preference to the surrounding air, which is fixed. Additionally, there is a relationship of the solvent to the air which is a modifiable value with respect to the contact angle.

$$\theta = \cos^{-1}\left(\frac{\gamma_{ws}^{0} - \gamma_s - \frac{CV^2}{2}}{\gamma_w}\right)$$

The previous two equations relate the change in contact angle to an applied voltage. As the voltage is increased, the contact angle decreases. This leads to a wetting state. These techniques will be used to produce a general class of display devices.

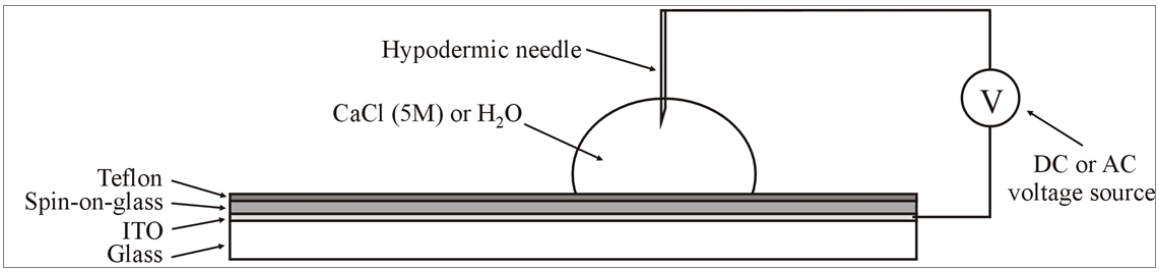

Figure 3. Schematic of electrowetting. The substrate is a glass slide coated with an ITO electrode layer. It is coated with a 100 nm layer of spin-on-glass with ~ 1-micron-thick Teflon layer. A droplet of water (usually with extra salt) is placed upon this hydrophobic substrate with a grounding electrode made of a hypodermic needle.

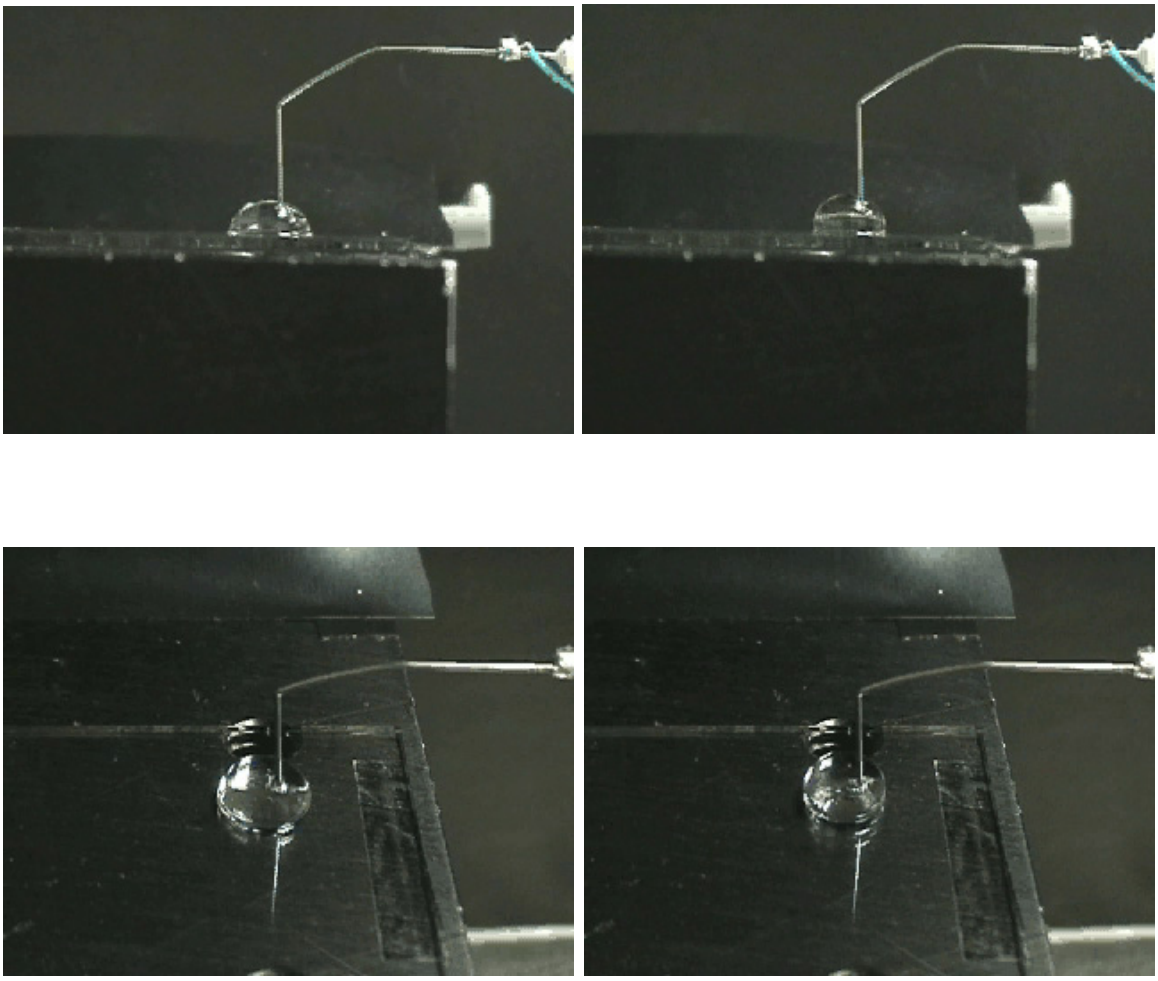

Figure 4. Images of electrowetting from the side and the top. Images show the two states of the droplet, the left side shows when there is voltage applied and the contact angle is decreased, whereas the right side shows when there is no voltage applied and the contact angle is at its normal, hydrophobic state.

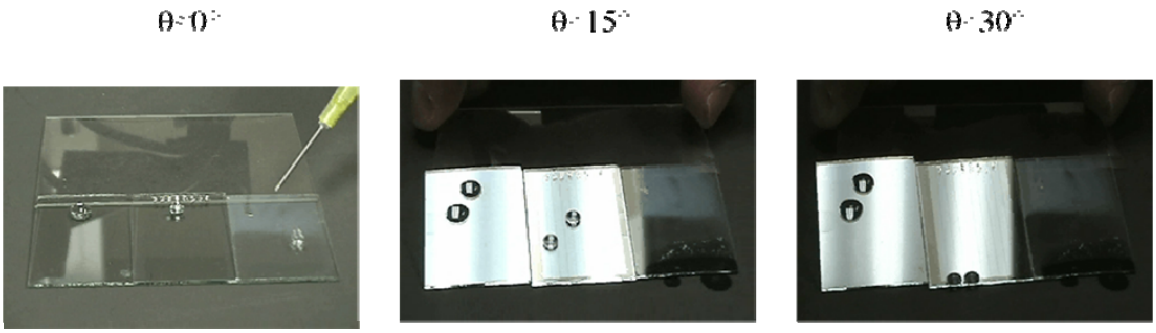

Figure 5. Images showing droplets on substrates with different hydrophobocity being tilted. The surface on the left side is a bare glass slide which is naturally hydrophilic (~ 30 degrees). The surface in the middle is a smooth Teflon-coated substrate which is slightly hydrophobic (~ 100 degrees). The surface on the right side is a rough Teflon-coated substrate which is superhydrophobic (~ 130 degrees). As the substrates are tilted at larger and larger angles, the droplets drop to the ground due to the competition between the friction forces and gravity. For the superhydrophobic substrate, the droplets drop at an angle slightly greater than 0 degrees. For the hydrophobic substrate, the droplets start to drop at an angle greater than 15 degrees. For the hydrophilic substrate, the droplets move at 30 degrees, although they prefer to spread out more than drop.

2. Droplet electrowetting

Electrowetting on dielectric [3] for lab-on-a-chip diagnostics has several advantages: increased automation, faster analysis, and high throughput [4–10]. Since electrowetting utilizes AC frequencies, it can be biologically and chemically compatible. In this section, we start with the principles of electrowetting display devices and show their advantages over traditional devices.

B. Electrowetting devices

1. Introduction

Electrowetting on dielectric demands similar fabrication capabilities as required for liquid crystal displays (LCDs). In an LCD display, there are several million pixels filled with liquid crystal molecules. Each pixel in a display typically includes three sub-pixels, one for each color (red, green, and blue). The display is backlit by a light source. Each pixel is controlled by electrodes on both substrates. These electrodes control the liquid crystal molecule.

In droplet electrowetting, a matrix of electrodes is used. Each would control different droplets. These techniques have been used to manipulate the liquids, controlling the phobicity of the solvent on the substrate.

There are several advantages of using LCD-compatible techniques for biosensing. By 2008, worldwide sales of televisions with LCDs had surpassed the sale of CRT units, indicating that mass fabrication is not a concern. [11] In a LCD, there are two polarizers in a crossed state as well as a color filter [12]. Similar techniques could be used for biosensing in detection polarized colloids, as well as filtering laser light.

Various devices have been developed using electrowetting as a means of manipulating phobicity of solvents [2, 14–15]. In the Philips prototype displays, electrowetting is used to move a colored oil layer away from a white background. The oil covers a hydrophobic layer, separating it from a water layer on top. Interaction of the oil,

water, and the hydrophobic layer is controlled by an electric field. Application of an electric field across the layers causes water to contact the hydrophobic layer, displacing the oil, and the colored pixel is replaced by a white background.

Electrowetting can be used as lensing devices [16, 17]. Two immiscible liquids are confined in a space between two substrates. Under the control of an electric field, the interface between the two liquids is changed. Light passing through the two immiscible liquids interacts with the interface and can be modified to focus or defocus depending on the applied electric field.

2. Electrowetting display device

In this section, an individual pixel that allows light to be transmitted is demonstrated. A fluid droplet is placed between two substrates and serves as an electrically controlled waveguide between a light guiding substrate and a display cover. Electrodes modulate the amount of light conducted through the fluid droplets from the substrate into the cover by controlling the contact area between the droplet and the light guiding substrate through the electrowetting principle.

A schematic and images of the device are shown in Figure 6 through 8. Both layers of the substrate are made hydrophobic using Teflon. Certain areas of the hydrophobic layer are etched to create hydrophilic regions. Fluid droplets will collect and remain within the hydrophilic regions. There are patterned electrodes on only one of the substrates. There are two distinct regimes of on and off of the display device. When there is no voltage applied, the droplet remains within the hydrophilic region of the top substrate. When there is a voltage of 100 V at 1 kHz applied, the droplet spreads to the hydrophobic region. In the first case, the droplet is connected to the bottom substrate which allows light to pass through the droplet. In the second case, the droplet is disconnected from the bottom substrate which does not allow light to pass through the droplet due to total internal reflection conditions.

Some unique features of this design are the capability to position the fluid droplets by creating hydrophilic regions within a hydrophobic substrate. Micropatterning using photolithography of hydrophobic Teflon is oxygen plasma etched with photoresist

as a sacrificial layer. After the hydrophobic layer is removed in certain regions, the sacrificial layer is removed to expose the hydrophobic regions. This is dipped into a liquid solution and the hydrophobic regions repel the liquids while the hydrophilic regions attract the liquids. This is further demonstrated in Figure 5 where a slight angle is enough to cause the gravity force to be greater than the surface tension forces required to keep the droplet on the hydrophobic substrate. This method can be used to obtain droplets of few bacteria or other objects across a large area.

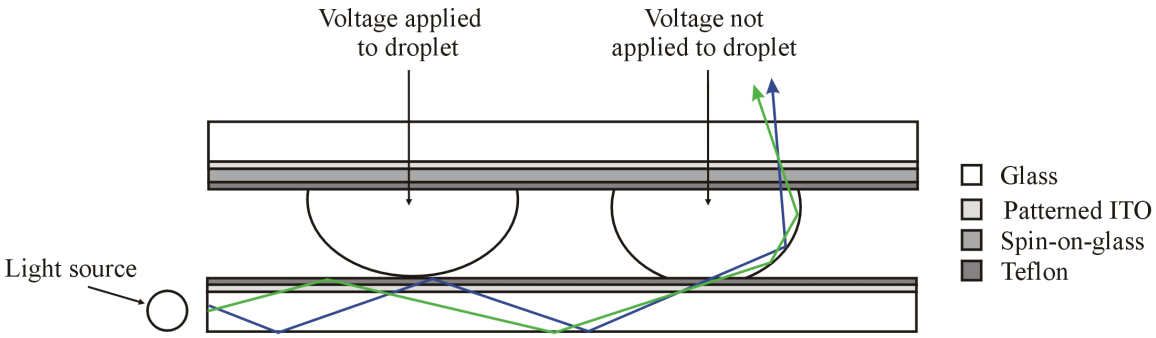

Figure 6. Schematic of electrowetting display. Both layers are hydrophobic due to Teflon. One layer contains patterned areas of hydrophilicity where the droplets of liquid remain. The electrodes are patterned such so that when the voltage is applied, the liquid preferentially spreads out on one of the substrates. By this method, the total internal reflection conditions of the light source can be controlled, enabling the display of light.

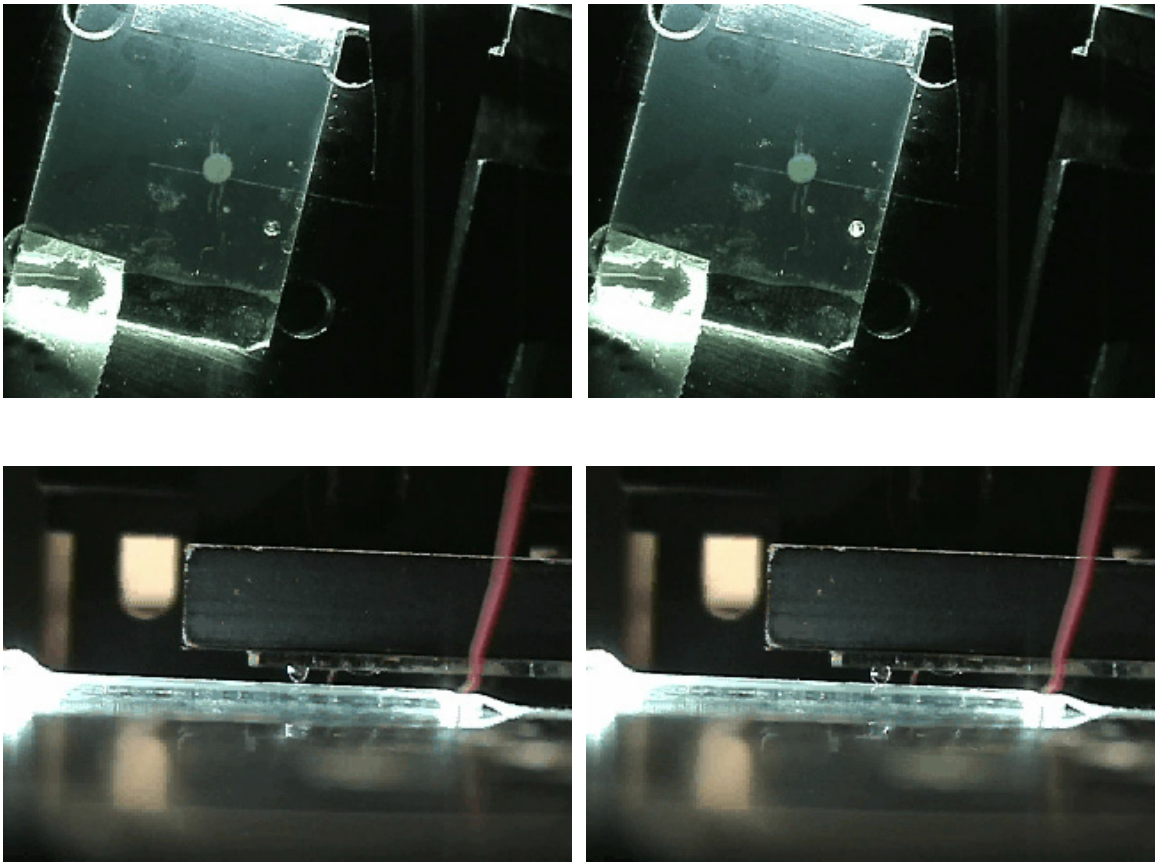

Figure 7. Image of a single droplet electrowetting display device. On the left, there is voltage applied and there are total internal reflection conditions for the light source. Therefore, there is light displayed through the droplet. On the right, there is no voltage applied and the light source is reflected to the viewer. This can be visualized on the top images.

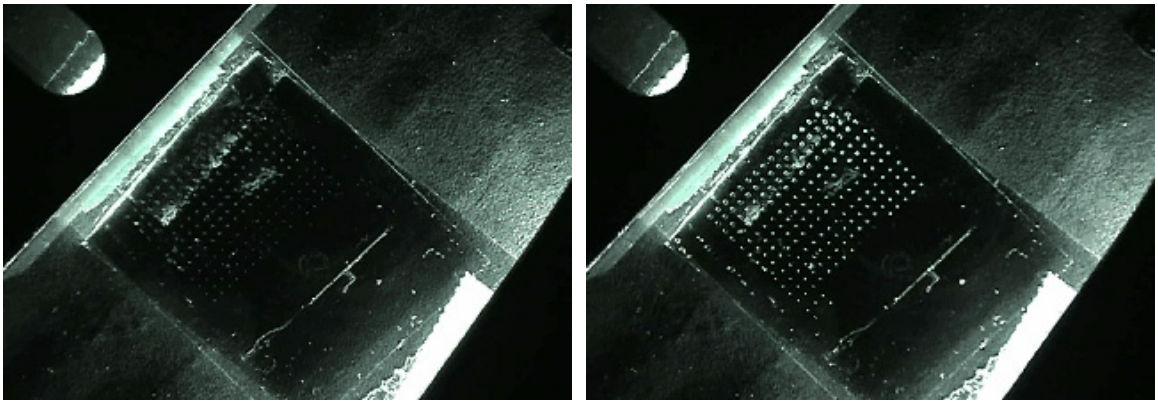

Figure 8. Image of a multiple-droplet electrowetting display device. Multiple droplets, approximately 100 microns in radius, are controlled at the same time and the two images shows the contrast between the two different states of the display device.

3. Grating electrowetting

These ideas can be further expanded to create a variable iris as shown in Figure 9 and Figure 10. In this concept, there are electrodes on each substrate. Rather than ambient air, oil is used as the other phase of the two-phase system. The conductive electrode substrate attracts the polar liquid and the hydrophobic-coated electrode substrate attracts the oil. There is a surrounding rubber spacer which attracts the oil. As an electric field is applied, the hydrophobic substrate will attract the water and the oil is displaced towards the rubber spacer. Since the oil is colored and absorbing, there is a variable iris which forms due to the clear liquid in colored, absorbing oil. With patterned electrodes on the hydrophobic substrate with clear liquids and clear oils of different refractive indices [18, 19], electrically variable devices are created as shown in Figure 11.

Figure 11 describes grating effects within a two-phase electrowetting system. This serves as a useful means to study two immiscible liquids as well as any molecules or particles on this interface. [20] Since electrowetting is readily affected by the relative changes in surface tensions at the interface, the change in the temporal or spatial profile of the grating electrowetting device describes the interfacial change.

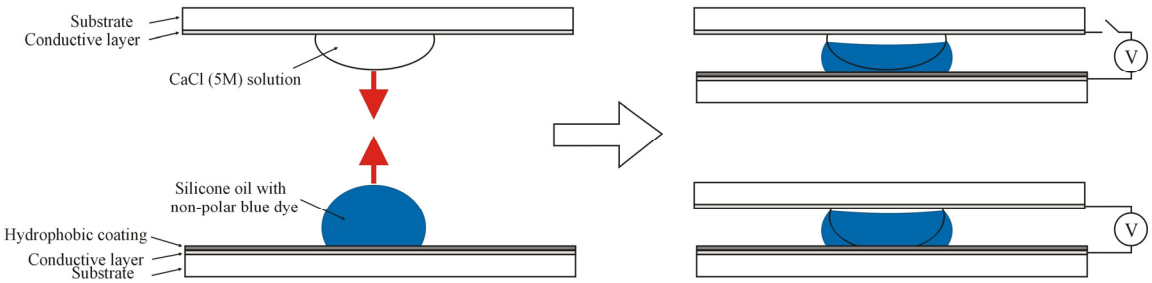

Figure 9. Schematic of the electrically adjustable iris. The oil is colored with blue, absorbing dye. Without a voltage, the clear, salty water does not quite reach the other substrate and there remains a thin, absorbing oil layer. When the voltage is applied, the water spreads onto the substrate, displacing the oil layer which opens up the iris.

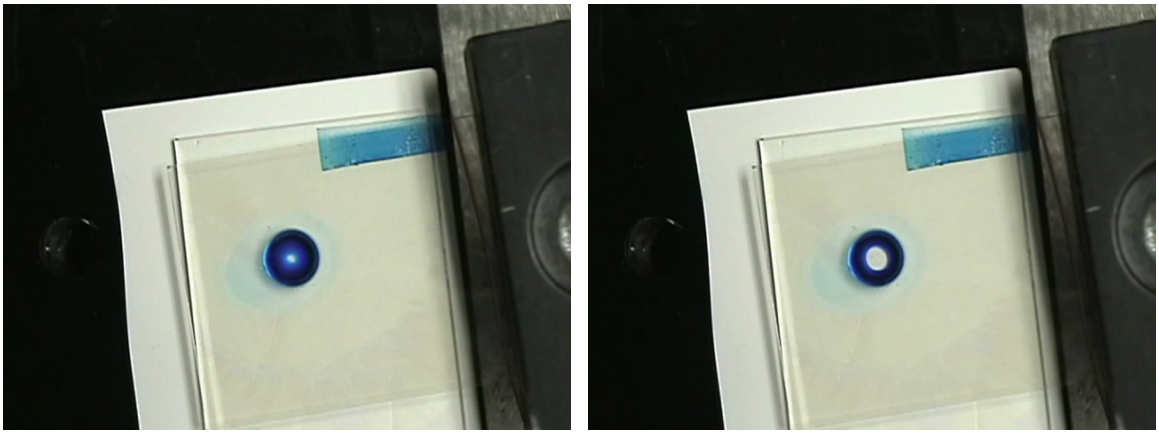

Figure 10. Image of the electrically adjustable iris. When the voltage is not applied, the iris is small as shown on the left. On the right, the voltage is applied and the iris opens up.

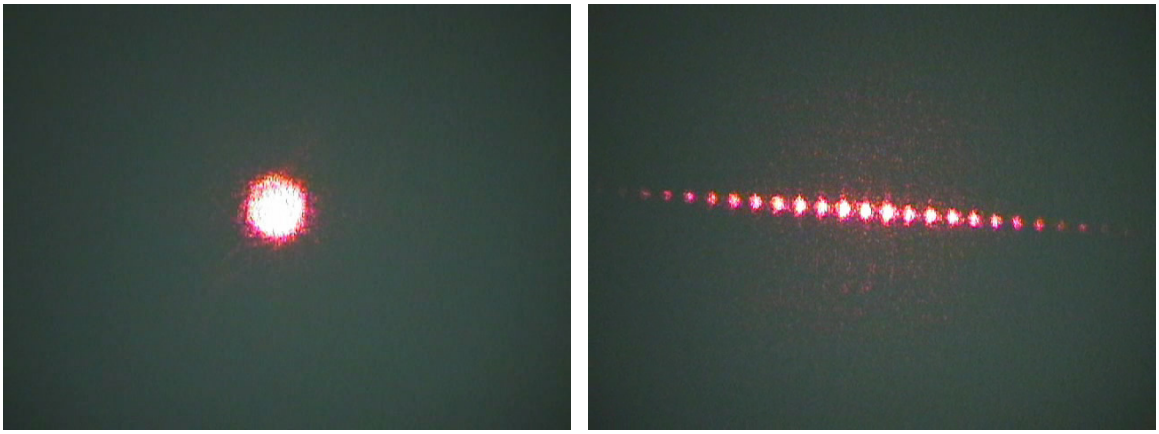

Figure 11. Electrowetting with patterned electrodes. Using the electrode structure shown in Figure 16, a sinusoidal pattern in the oil-water interface can be achieved by applying an electric field. On the left, when there is no applied electric field, the interface is slightly focusing and defocused at the sample plane shown. On the right, the applied electric field causes a ripple in the interface which corresponds to the electrode structure. This causes the grating to show up.

4. Electrically adjustable iris

In Figure 12, the initial design is modified to have a two-phase system with oil and water. This type of system can have better control of evaporation and is compatible with backlit display technologies. In this embodiment, a voltage of 1 Vpp is applied to the electrodes which wet both substrates causing a capillary bridge to form. At voltages higher than 10 Vpp, the capillary bridge separates into two separate droplets [21, 22]. In the situation where colored, absorbing oil is used, this can be used as a display device. However, with clear oil, lenses are created from the capillary bridge leading to high-focal-length changes in an extremely compact device.

Therefore, this is an electrically adjustable iris where it is possible to go from a single droplet state to a connected capillary bridge to a separated droplet state. The separated droplet state is interesting for using one of the droplets as a lens for imaging objects within the second object. However, the strength of the applied electric fields acts as a limitation on the objects which may be imaged.

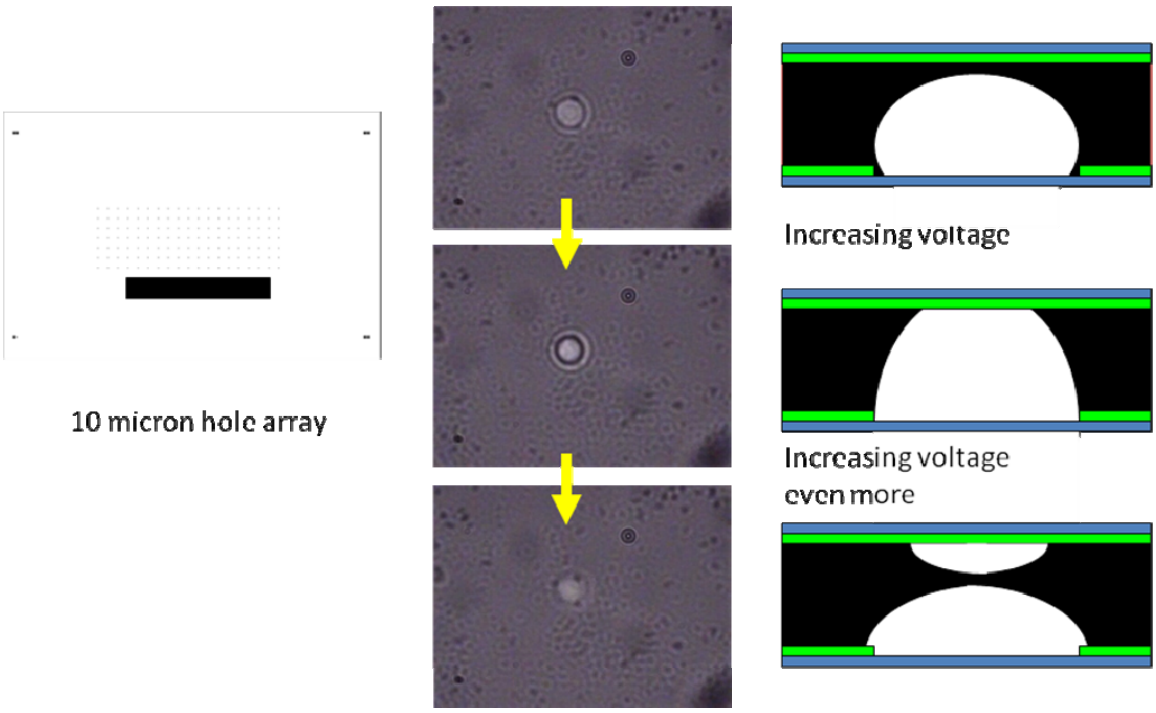

Figure 12. Miniaturized electrically adjustable iris. The iris has been miniaturized to 10 microns. In this scenario, as voltage is increased further and further, the capillary bridge may be separated into two droplets. The highest transparency is achieved when the capillary bridge is connected. The effect of separating the capillary bridge is not readily apparent for larger droplet sizes due to dielectric breakdown for the higher electric fields required at larger droplet sizes to achieve similar effects.

5. Mechano-optofluidic device

In this device, one of the substrates has a flexible plastic backing. This allows for the substrate to flex, dependent on contact with the liquid due to surface tension forces. These types of substrates are explored for bistability with regard to optical and tactile feedback.

Two substrates are used, a bottom substrate containing a glass slide with patterned electrodes covered by a patterned superhydrophobic layer such that the liquid remains in the relatively hydrophilic regions of the substrate. The top layer contains a grounded electrode layer without any extra coatings. In the unconnected state, the liquid remains on the bottom, solid substrate region just barely touching the top, flexible substrate. In the connected state, the liquid between the bottom and top substrate is connected and the top, flexible substrate flexes down. Both states are stable without additional external forces. There is only one means by which to switch from the unconnected state to the connected state; however, there are two means by which to switch from the connected state to the unconnected state. For the first scenario, a mechanical means must be used. In the mechanical method, the flexible substrate is pushed down until there is contact with the liquid and the contact angle increases beyond the stable point. In the second scenario, a mechanical or electrical means may be used. Similar to before, mechanically, the two substrates are separated until the flexible substrate is below the stable point contact angle. By the electrical method, there is a voltage applied such that the liquid spreads out on the bottom, flat substrate. Then, the liquid may go below the stable point contact angle. This second method is dependent on the size of the device. It can be achieved with relative

ease for smaller devices, however, for larger devices, a larger force is required which means that a larger voltage may exceed the breakdown voltage of the dielectric between the liquid and conductive layer. [23]

As a tactile device, such a device is imagined to be capable of having a pattern of raised and lower surfaces. This device can be reset, leaving all the flexible substrates flexed down mechanically. Then, using electrical means, the substrate may be changed to have certain regions flexed up. We imagine this may be useful to provide tactile feedback for touchscreen devices or display devices where it can provide additional stimulation with regard to buttons. There is an ultimate limitation in the speed of such devices as there is a mechanical component to the liquid. We imagine that changes on the order of 1 second are possible.

When there is minimal contact between the liquid droplet and the top, flexible substrate, there are total internal reflection conditions. Therefore, the viewer sees no light. When there is contact between the liquid droplet and the top, flexible substrate, there is transmission of light. This can act as a bi-stable display since the two distinct states require no energy to remain stable. As a device, it is too slow to act as a video playing display; however, for slower display applications such as billboards or advertisements, this may be an interesting alternative to current methods of display, especially during low-light conditions. Current methods of display rely on the reflection of light during low-light conditions. This display would be capable of being back-lit and would be much more effective during low-light conditions.

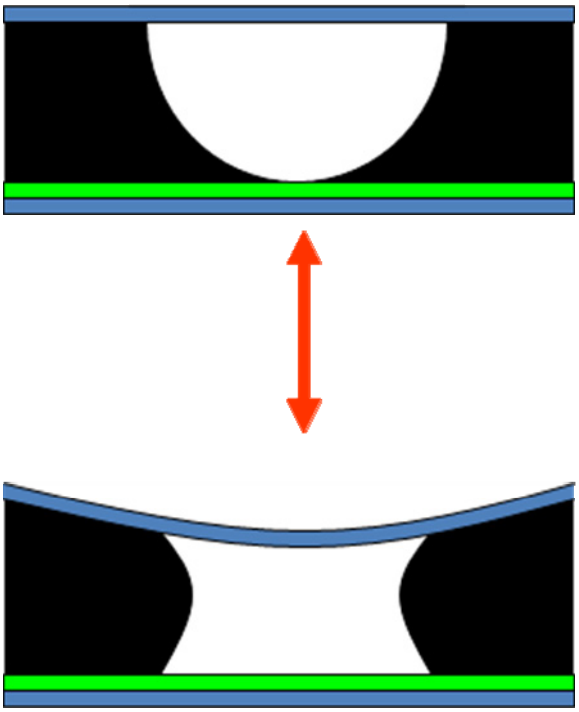

Figure 13. Electrowetting with a flexible substrate. The top substrate is a flexible plastic. Initially, when there is no capillary bridge, there is no connection between the top and bottom substrates. Therefore, the flexible substrate remains flat. When the capillary bridges are connected, the flexible substrate flexes to try to maintain the same contact angle between the substrate, air, and liquid as the bottom substrate. These two states are so bi-stable that each may be modified through mechanical and electrical means.

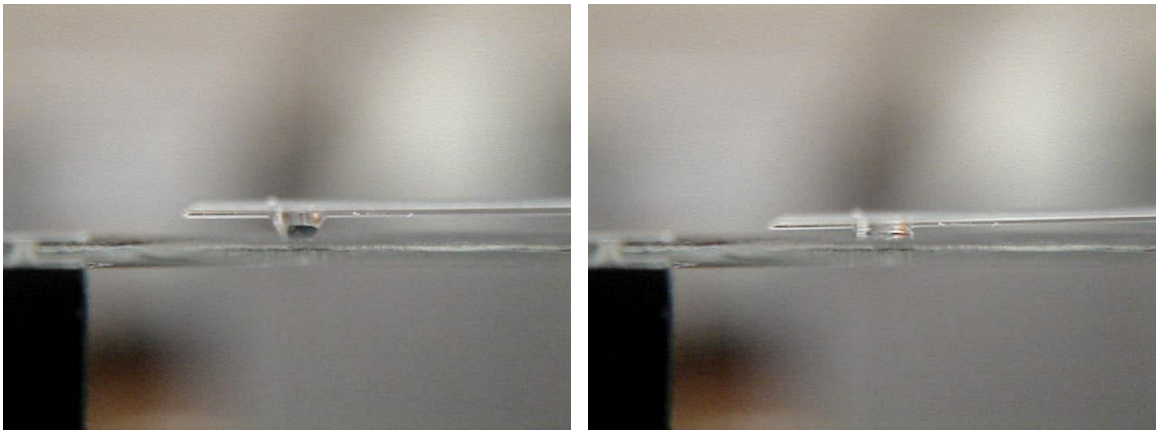

Figure 14. Image of electrowetting with a flexible substrate. A single droplet is shown. On the left, the droplet is connected only to the top. When the droplet is connected to form a capillary bridge, the top substrate flexes down. Note the distance between the top and bottom substrate is the same.

A. References

1. Berge, B. Electrocapillarity and wetting of insulator films by water. CRAS 317, 157–163 (1993).
2. Mugele F, Baret JC. Electrowetting from basics to applications. J Physics: CM 17 (2005).
3. Cho SK, Moon H, Kim CJ. Creating, transporting, cutting and merging liquid droplets by electrowetting based actuation for digital microfluidic circuits. J Microelectromechanical Systems 12, 70–80 (2003).
4. Fair RB, Khlystov A, Tailor TD, Ivanov V, Evans RD, Griffin PB, Srinivasan V, Pamula VK, Pollack MG, Zhou J. Chemical and biological applications of digital microfluidic devices. IEEE Circuits and Systems 24, 10–24 (2007).
5. Song H, Chen DL, Ismagilov RF. Reactions in droplets in microfluidic channels. Angewandte Chemie 45, 7336–7356 (2006).
6. Zhao Y, Cho SK. Microparticle sampling by electrowetting-actuated droplet sweeping. Lab on a Chip 6, 137–144 (2006).
7. Srinivasan V, Pamul VK, Fair RB. An integrated digital microfluidic lab-on-a-chip for clinical diagnostics on human physiological fluids. Lab on a Chip 4, 310–315 (2004).
8. Moon H, Wheeler AR, Garrell RL, Loo JA, Kim CJ. An integrated digital microfluidic chip for multiplexed proteomic sample preparation and analysis by MALDI-MS. Lab on a Chip 6, 1213–1219 (2006).
9. Dubois P, Marchand G, Fouillet Y, Berthier J, Douki T, Hassine F, Gmouh S, Valutier M. Ionic liquid droplet as e-microreactor. Anal Chem 78, 4909–4917 (2006).
10. Paik P, Pamul VK, Fair RB. Rapid droplet mixers for digital microfluidic systems. Lab on a Chip 3, 253–259 (2003).
11. http://www.displaysearch.com.
12. http://en.wikipedia.org/wiki/Liquid_crystal_display.
13. Hayes RA, Feenstra BJ. Video-speed electronic paper based on electrowetting. Nature 425, 383–385 (2003).
14. You H, Steckl AJ. Three color electrowetting display devices for electronic paper. Applied Physics Letters 97, 023514 (2010).
15. Heikenfeld J, Steckl AJ. Intense switchable fluorescence in light wave coupled electrowetting devices. Applied Physics Letters 86, 011105 (2005).
16. Berge B, Peseux J. Variable focal lens controlled by an external voltage: an application of electrowetting. Eur. Phys. JE 3, 159–163 (2000).

17. Quilliet C,Berge B. Electrowetting: a recent outbreak. Curr. Opin. in Colloid and Interface Science 6, 34–39 (2001).

18. Staicu A, Mugele F. Electrowetting induced oil film entrapment and instability. Phys. Rev. Lett. 97, 167801 (2006).

19. Brown CV, Wells GG, Newton MI, McHale G. Voltage programmable liquid optical interface. Nat. Photonics 3, 403–405 (2009).

20. De Aguiar HB, De Beer AGF, Strader ML, Roke S. The interfacial tension of nanoscopic oil droplets in water is hardly affected by SDS surfactant. JACS Communications 132, 2122–2123 (2010).

21. Klinger A, Herminghaus S, Mugele F. Self excited oscillatory dynamics of capillary bridges in electric fields. Appl. Phys. Lett. 82, 4187 (2003).

22. Mugele F, Baret JC, Steinhauser D. Microfluidic mixing through electrowetting induced droplet oscillations. Appl. Phys. Lett. 88, 204106 (2006).

23. Klinger A, Buehrle J, Mugele F. Capillary bridges in electric fields. Langmuir 20, 6770–6777 (2004).

III. Bacteria detection

A. Introduction

The adaptability provided by surface optofluidic techniques is compatible with biosensing. Both topics deal with a change in the sample of interest. Normally, the sample of interest is in a fluidic environment. Optical means of identifying the sample of interest is one of the possible methods of biosensing. In the following section, we motivate and review traditional methods and some current optical means of biosensing.

B. Motivation

According to the World Health Organization, in 2003, infectious diseases were the cause of 25.9% of total estimated annual deaths. [1] These infectious diseases are caused by bacteria, viruses, and other microorganisms. Specifically, bacteria pathogens have become one of the most important causes of disease. In the United States, foodborne pathogens such as *Escherichia coli* and Salmonella have become quite infamous for their ability to cause widespread panic to the public.

1. Conventional methods of detection

Conventionally, the sample of bacteria is placed in various growth media and allowed to multiply at optimal conditions. The cells are allowed to grow into colonies for up to 72 hours. Afterwards, visual colony counts are performed by a lab technician to obtain the number of organisms. These tests are usually not definitive with regards to the specificity of bacteria. [2, 3] These limitations have resulted in the development of more complicated instruments for bacteria identification.

2. Bacteria identification using optical instruments

First, the necessity of a lab technician can be eliminated through visual recognition software by a camera counting cells on a microscope. [4] Another method adds a pre-labeling step by mixing the cells with fluorescent markers and counting the number of cells by flow cytometry. [5] However, both techniques still require preparation of the sample including colony growth of the cells, modification of the solution, and loading the sample into the microscope or device.

Many methods that have high specificity rely on pre-labeling techniques whereby an additional marker is attached to the sample of interest to increase identification abilities. In this section, some previous works involving pre-labeling which rely on optical methods for detection are discussed. The additional markers are attached to surfaces to change the refractive index. These would be detected with a waveguide [6], surface plasmon resonance [7] , or interferometers [8].

In [6], a thin film waveguide is placed below a fluidic channel with the sample of interest. The evanescent field penetrates into the fluidic channel approximately 100 nm. The surface of the waveguide is immobilized with the appropriate antibody to detect the fluorescently labeled sample of interest. As these fluorescently labeled samples attach to the surface, the intensity can be detected to determine the concentration.

In [7], the optical setup is under a total internal reflection setup. The sample holder is a glass cell with a fluidic channel placed upon a thin gold film. The gold film is immobilized with the appropriate antibody as before. Similar to before, after the samples

attach to the interface, the refractive index is changed. By monitoring the reflected light, the device can determine the concentration of samples on the interface. This data can be determined by either scanning across different angles or by looking at the changing reflectivity.

In [8], two separate light beams interfere with each other before the detector. One of the light sources acts as a control. The other light source interacts with the sample of interest evanescently. As the refractive index is changed for one of the light sources, the phase of the light changes, which results in intensity change after the interference of the two beams.

In these surface-immobilized evanescent sensors, a high level of specificity can be obtained by utilizing the proper antigens. However, they suffer from false positives which occur when contaminants attach to the functionalized surface.

For label-free detection of bacteria, light scattering can be utilized to determine the size and refractive index [9, 10]. Scattering properties of objects are dependent on the size of the sample and the refractive index difference between the sample and the medium. This method can suffer from large noise as anything in the medium itself will cause scattering. In the following section, we describe the ability to apply electric fields to create two data sets, one as a control and the other as a crystallized state with all the samples of interest aligned to the externally applied electric field.

3. Light scattering of bacteria

Light scattering is one of the techniques utilized to determine the properties of a single bacterium [10], cells [11], and tissues [12]. For bacteria, Rayleigh-Debye-Gans approximation can predict the optical scattering [9]. This approximation has the following requirements: the refractive index difference between the bacteria and media must be small and the phase shift of the light must be small. For bacteria, both these conditions generally hold true [10].

In the Rayleigh-Debye-Gans approximation, the two requirements allow for the assumption that the particle does not perturb the incident field. Therefore, the scattering field is generated by the independent dipoles within the particle that are excited by the incident wave. In the next chapter, we will use similar terminology to describe scattering from gold nanoparticles much smaller than the wavelength of light. For asymmetric particles, the optical scattering for ellipsoids in media has been calculated [13]. The equation assumes two things: the solution is dilute such that the secondary scattering effects may be ignored and the solvent scattering can be accounted for separately.

In asymmetric bacteria such as *E coli*, the bacteria are rod-shaped with a longer axis, approximately 2 to 5 microns long, and two shorter axes, approximately 1 micron wide as shown in Figure 15. If the bacteria are assumed to be lying solely in a single plane, the scattering pattern is dependent on the waist of the *E coli*, which is proportional to its angle in the plane. In a solution with many asymmetric bacteria, due to the randomness of the bacteria orientations, the scattering pattern is an average over all the

different possibilities. If all the asymmetric bacteria are aligned, the scattering response is similar to that for a single bacterium.

In the following section, we describe using electric fields to align the bacteria. This allows us to detect asymmetric bacteria even in solutions that are contaminated with other scatters. The difference in optical scattering between the unaligned/random state and the aligned state determines the number of asymmetric particles in the solution.

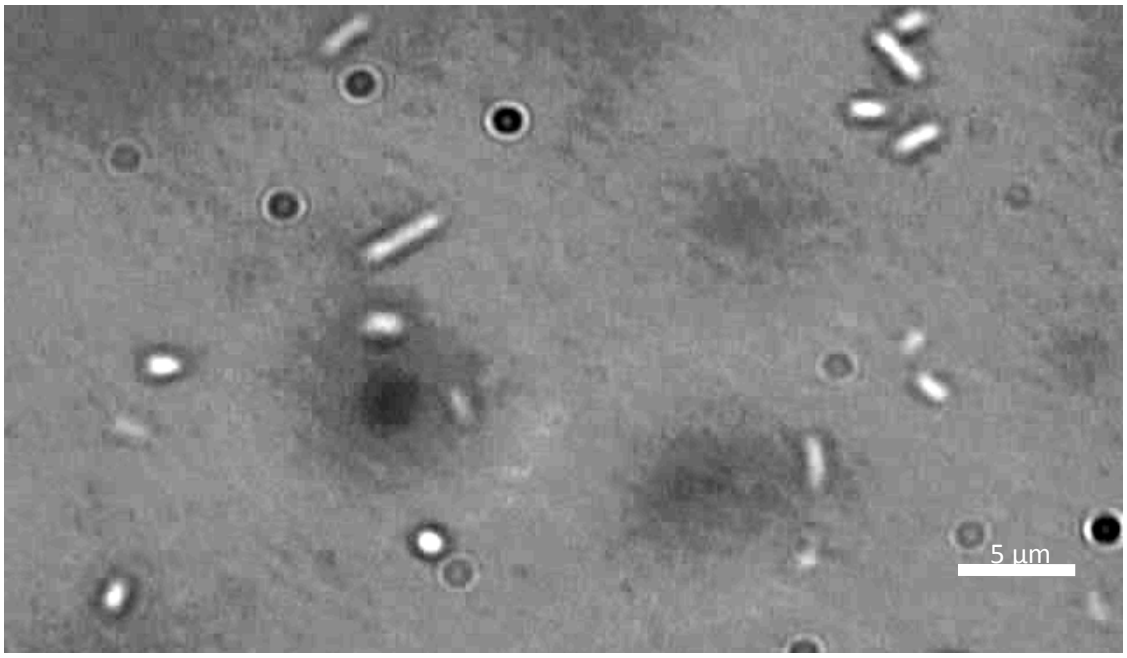

Figure 15. *E. coli* bacteria under 500x magnification. The bacteria are rod-shaped with diameters of approximately 1 micron and lengths ranging from 2 to 5 microns

C. Optical scattering of bacteria

1. Device and optical setup

The optical setup, shown in Figure 16, consists of a 5 mW HeNe laser which illuminates a transparent specimen holder consisting of a 1-mm-thick glass plate with a conductive electrode pattern in indium tin oxide (ITO) and a thin cover glass, separated by a 20 μm spacer. The void between the glass plates holds approximately 2 μL of test specimen. The laser beam has a diameter of approximately 1.5 mm resulting in an interaction volume of approximately 150 nL. An array of photodiodes at different angles or a simple optical power detector (UDT S370) at a continuous variable angle is used to measure the optical scattering. The specimen holder is connected to a signal generator to provide an alternating voltage of ±10 V.

An alternating voltage was chosen to eliminate electrolysis in the test specimen at the electrodes. Electrolysis causes bubbles of hydrogen and oxygen gas to form at the boundary of the electrode and liquid. To avoid the creation of bubbles without decreasing the applied voltage, a frequency greater than 1 MHz was necessary. Under observation through the microscope, the asymmetric bacteria aligned to the electric field most efficiently at 10 MHz.

The specimen holder, as shown in Figure 17, is fabricated using contact photo lithography. First, we obtain ITO-coated glass plates (Aldrich) rated at 30–60 Ω/square. Next, positive photoresist (S1813) is spin-coated onto the plates. A pattern is exposed

using a UV mask aligner and developed. Finally, the ITO is etched to create the electrode pattern.

The conductive electrode pattern is inter-digitated as shown in Figure 16 and Figure 18. In determining the optimal electrode spacing and width for optical scattering, there are three factors to consider. First, it has been observed that bacteria do not align over the electrodes. Therefore, the electrode width should be minimized. Second, the spacing between electrodes should be minimized to increase the electric field strength. Third, the electrode width should be maximized to decrease the resistance of the electrode. By testing the performance of different electrode spacing and widths from 10 microns to 500 microns, the optimal electrode spacing and width was determined to be 200 microns and 100 microns, respectively.

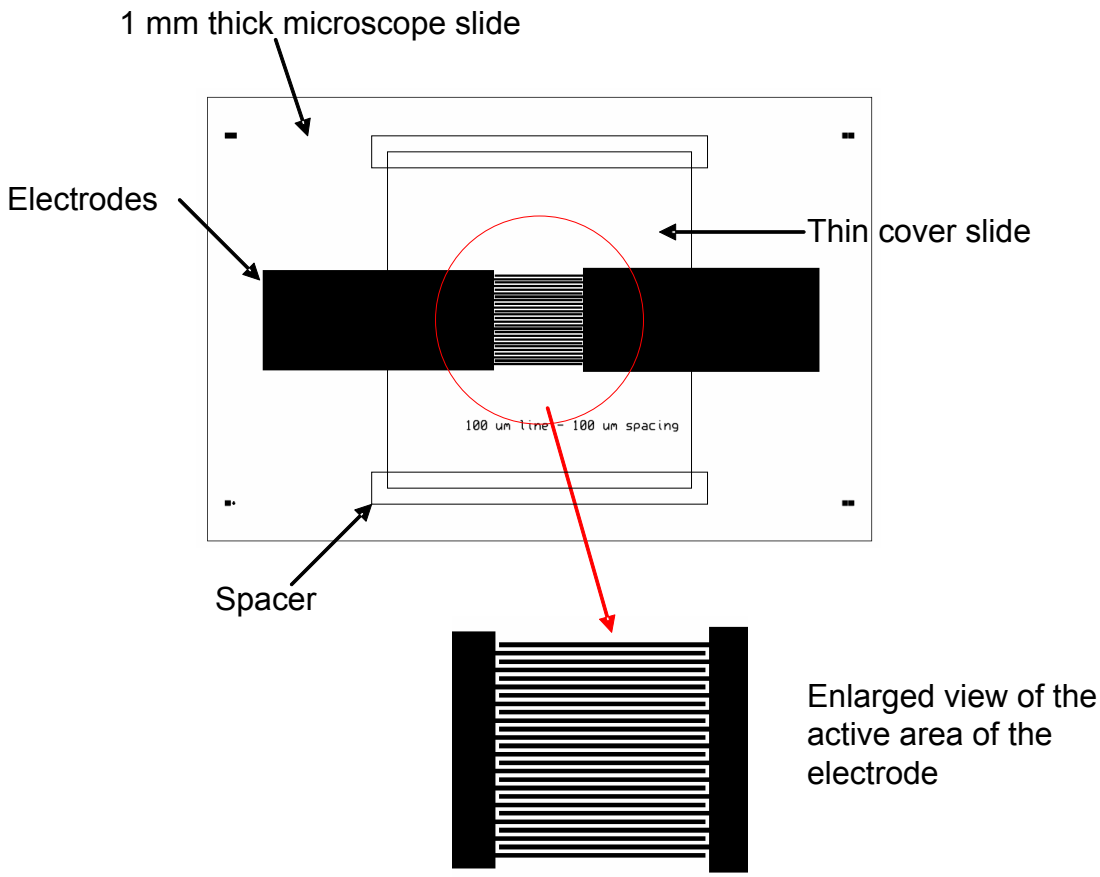

Figure 16. Schematic of the electrode pattern. The pattern is two combs facing each other. The electrodes are 100 microns wide separated by 100 microns. A vertical electric field is generated by this electrode pattern. A spacer can be used before placing a cover slide. Scotch tape measuring 50 microns in thickness were used as spacers.

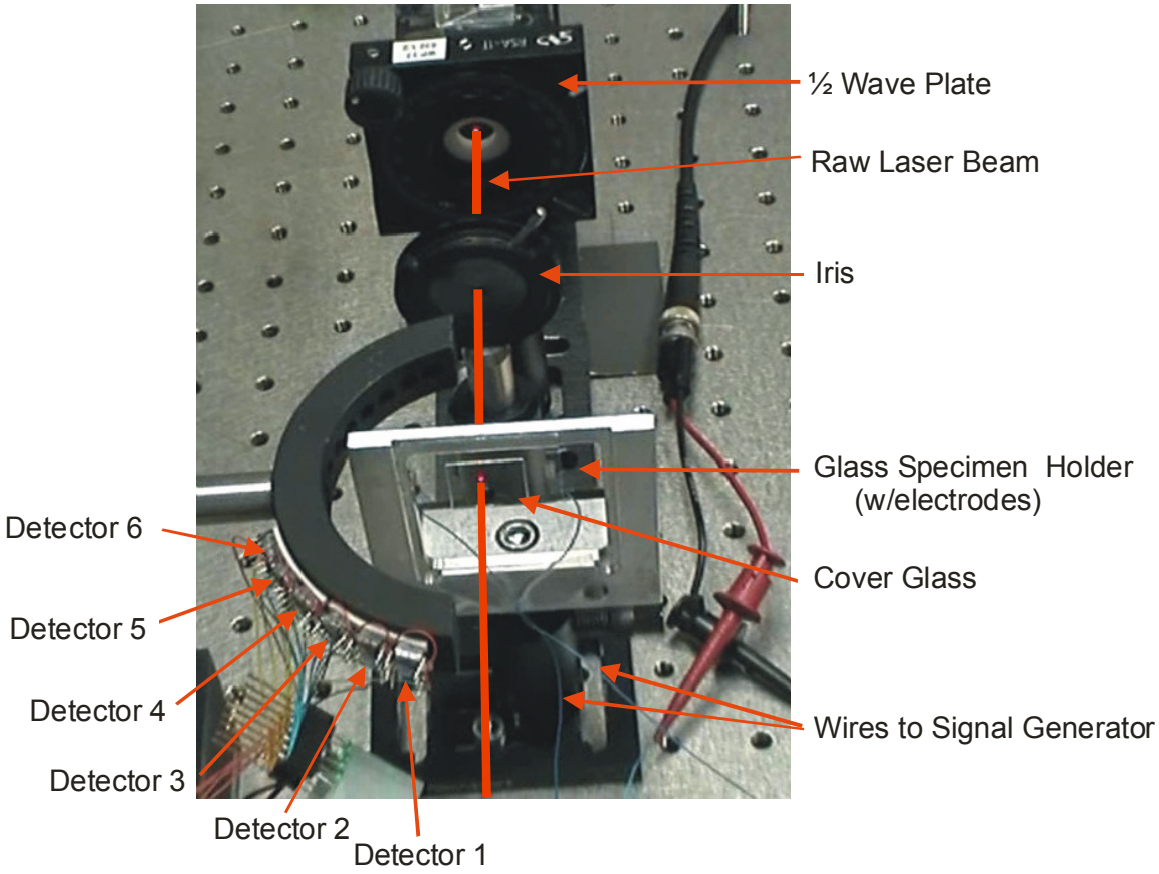

Figure 17. Diagram of the optical setup of bacteria scattering. A 633 nm laser from the top of the image is going towards the bottom of the image. The laser output is polarized and the half-wave plate is utilized to pick the proper polarization. The specimen holder is placed perpendicular to the laser beam. The detectors are placed at an angle, on the same plane as the laser beam.

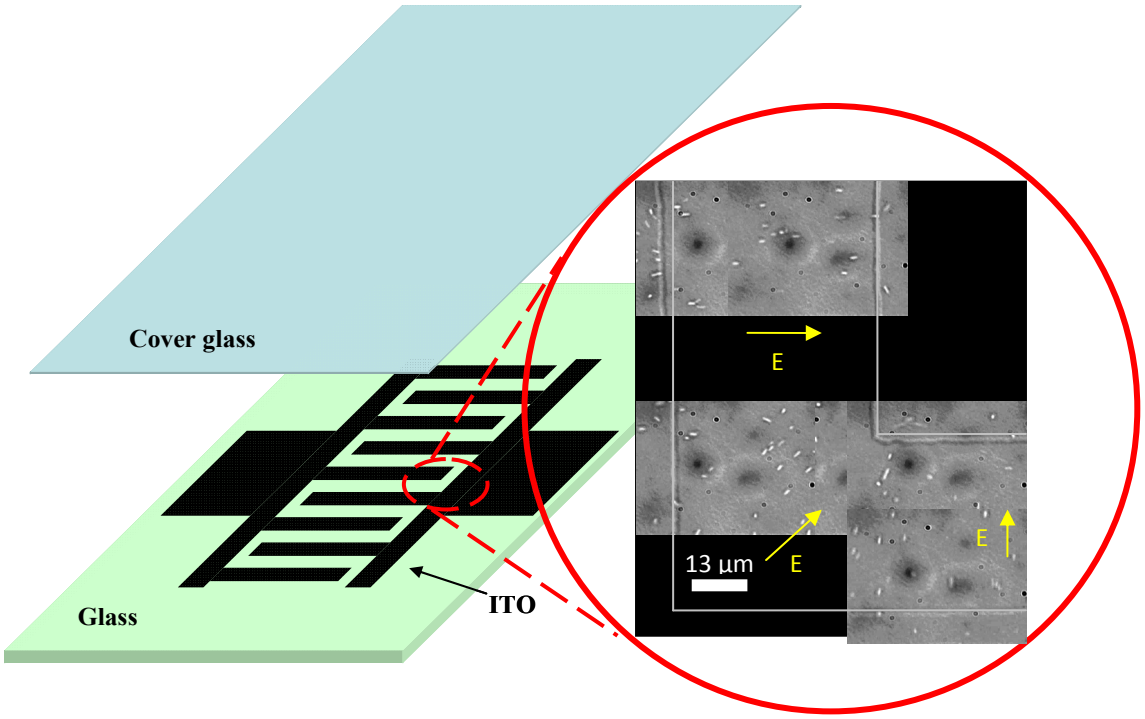

Figure 18. Schematic diagram of the specimen holder. A 1-mm-thick glass plate with a conductive electrode pattern in indium tin oxide (ITO) is separated from a thin cover glass with a spacer. The inset shows a sample of *E. coli* in urine aligned to the applied electric field between the electrodes.

2. Aligned bacteria

To visualize the effects of the electric field on asymmetric bacteria in solution, the specimen holder is placed under a microscope. Our sample of bacteria is *Escherichia coli* (*E. coli* K12), which are rod-shaped bacteria. When no electric field is applied, live *E. coli* move randomly and are aligned randomly as shown in Figure 19(a). When the electric field is applied, live *E. coli* align to the field as shown in Figure 19(b); we observe the shorter *E. coli* aligning rapidly and the longer *E. coli* aligning slowly. Even at the corners of the electrodes, *E. coli* align to the field lines, as shown in the inset of Figure 18. When the electric field is turned off, live *E. coli* move to orient themselves randomly. Note that dead *E. coli* and other symmetric particles do not move or change orientations with respect to the electric field and appear stuck to either the glass plate or cover slide.

The orientation of the bacteria need not be parallel to the image plane. The orientation of the bacteria may be in and out of the image. By stacking two glass plates with ITO as shown in Figure 20, we were able to align bacteria perpendicular to the plane of the device. Bacteria that are located just outside of the electrode boundary do not align and remain in random orientations.

The ability to detect bacteria through an automated process without expensive and bulky equipment such as an optical microscope would be beneficial for many reasons. First, untrained technicians could operate the equipment. Second, the results may be obtained rapidly. Third, the system could be made small and inexpensive.

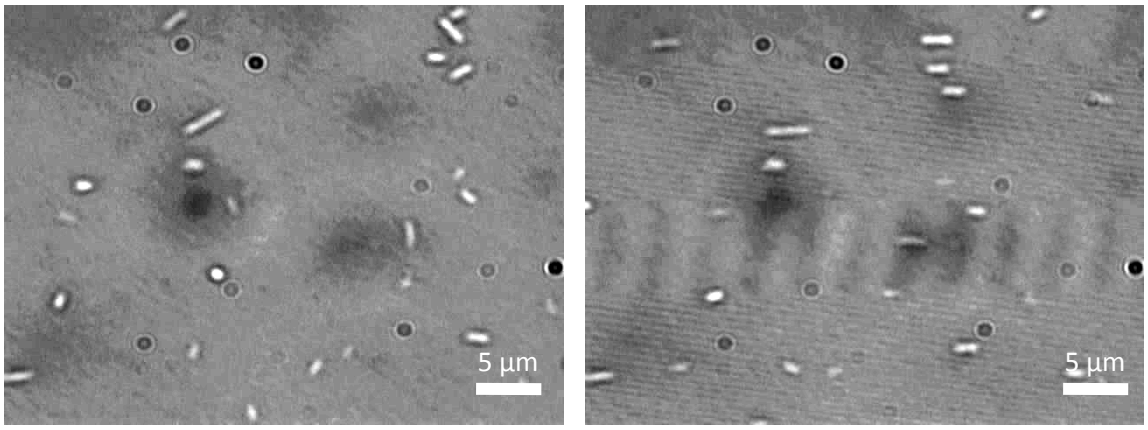

(a) (b)

Figure 19. Live *E. coli* bacteria under 500x magnification. (a) No electric field. The bacteria are aligned randomly. (b) Applied electric field in the horizontal direction. The bacteria are aligned to the electric field. Larger bacteria align slower than the smaller bacteria.

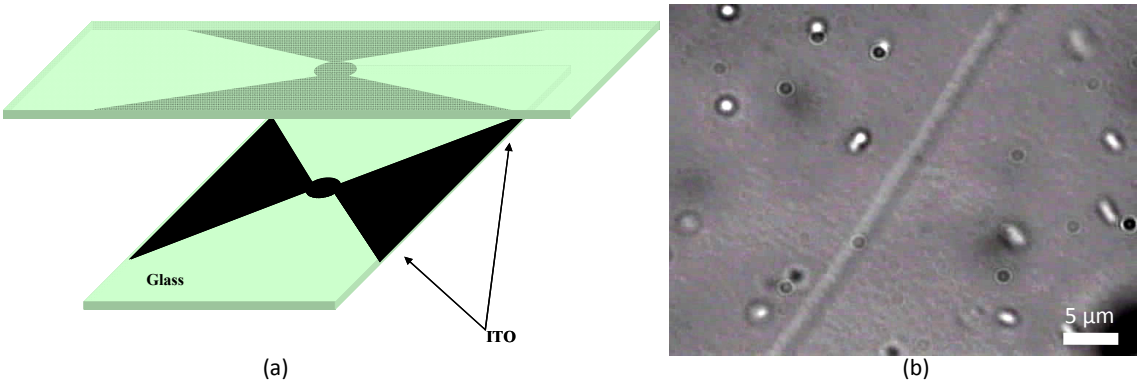

Figure 20. Specimen holder which aligns bacteria in and out of the plane. (a) Schematic diagram of the parallel plate specimen holder. (b) Applied electric field normal to the image plane. Note the line from the upper right to the lower left of the image. The two electrodes are stacked on top of each other and are located to the left of this boundary. Bacteria to the left of this boundary align to the electric field, normal to the image plane, and appear as points. Bacteria that are immediately to the right of this boundary orient to the fringe fields from the electrodes, from the upper left to the lower right of the image.

To eliminate the need for an imaging system, we have investigated optical scattering as a means to detect the presence of live bacteria. Randomly oriented rod-shaped bacteria have optical scattering measurements with peaks as a function of a scattering angle corresponding to the bacteria's radius and length [9, 10]. Aligned rod-shaped bacteria have optical scattering measurements with peaks as a function of scattering angle corresponding to either the bacteria's radius or length. In our scheme, the automated detection compares the optical scattering of randomly oriented bacteria versus aligned bacteria.

3. Optical scattering data of aligned bacteria

Figure 21 shows the optical scattering for samples of $5 \cdot 10^7$ colony-forming units (CFU)/mL live *E. coli* in urine, and no live *E. coli* in urine. When the electric field is turned on (between the dashed green lines), we notice that the sample of $5 \cdot 10^7$ CFU/mL live *E. coli* in urine has a scattered power increase of 20%. A control experiment with filtered and sterilized urine that contained dead *E. coli* showed no change in the amount of scattered power with an applied electric field.

The optical scattering measurement shows different rise and fall times when the electric field is turned on and off. We noticed that bacteria of different sizes align at different speeds to the electric field. For our particular sample of $5 \cdot 10^7$ CFU/mL live *E. coli*, we have a rise time measurement of approximately 500 milliseconds and a fall time measurement of approximately 1.5 seconds, as shown in Figure 22. The different rise and fall times of bacteria may be due to their different sizes, dielectric constant, or polarizability. Therefore, through calibration, we may be able to distinguish the types of different bacteria in our test sample.

Figure 23 shows optical scattering measurements with varying bacteria concentration and angle of the detector. Figure 23(a) shows similar measurements as shown in Figure 21. On average, the scattering measurements indicate that there is about a 20% increase when the electric field is turned on for $5 \cdot 10^7$ CFU/mL live *E. coli* in urine. Figure 23(b) shows measurement data for $5 \cdot 10^6$ CFU/mL live *E. coli* in urine. There is about a 5% increase when the electric field is turned on. We note that the threshold of the

optical scattering measurement for detecting bacteria occurs at a concentration which is on the order of magnitude 10^6 CFU/mL live *E. coli* in urine. Additional improvements to the detection scheme would rely on pre-concentration within a microfluidic circuit [14].

This threshold of bacteria detection is on the same order of magnitude as current bacteria detection methods such as urine cultures [15] and biosensor techniques that detect antigen-antibody, enzyme-substrate, or receptor-ligand complexes by measuring fluorescent light, surface reflection, and electrical properties [16–19]. Unlike these methods, we have demonstrated a bacteria detection scheme that uses no biochemical markers and has the potential to be small, inexpensive, and easy to use for untrained technicians, and provides rapid results.

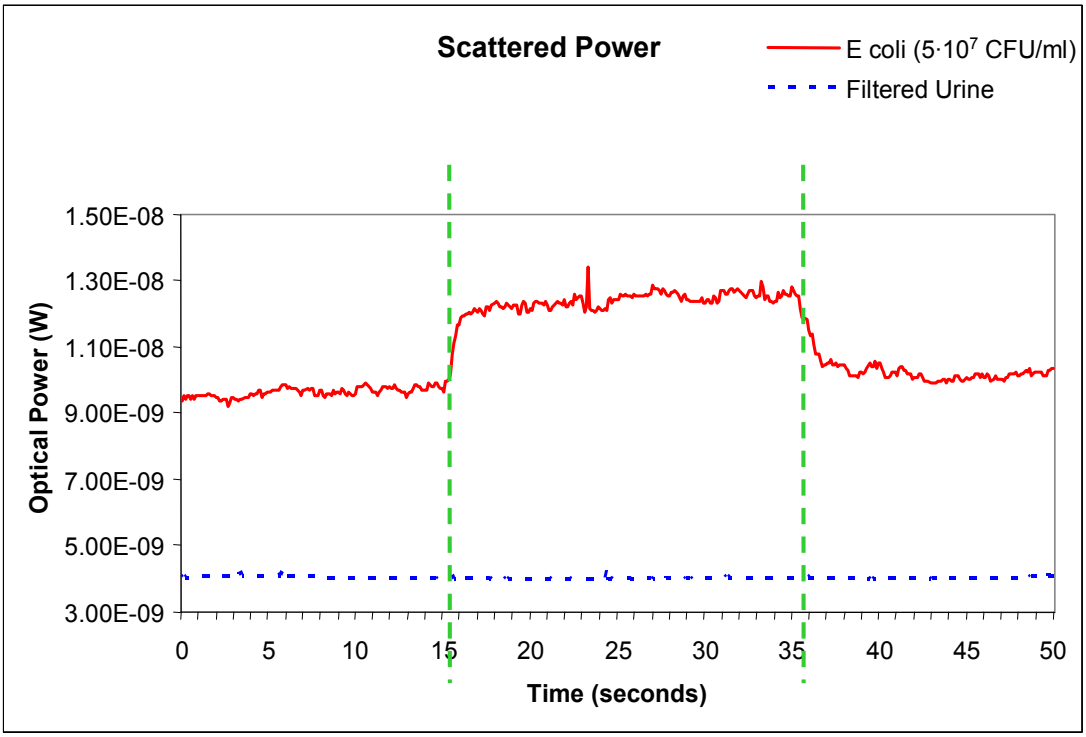

Figure 21. Optical scattering measurements at an angle of approximately 33 degrees. The solid curve shows the increase in the optical scattering when the electric field is turned on (between the vertically dashed lines) for $5 \cdot 10^7$ CFU/mL live *E. coli* in urine. The dashed curve shows the same measurement for filtered and sterilized urine with dead *E. coli*.

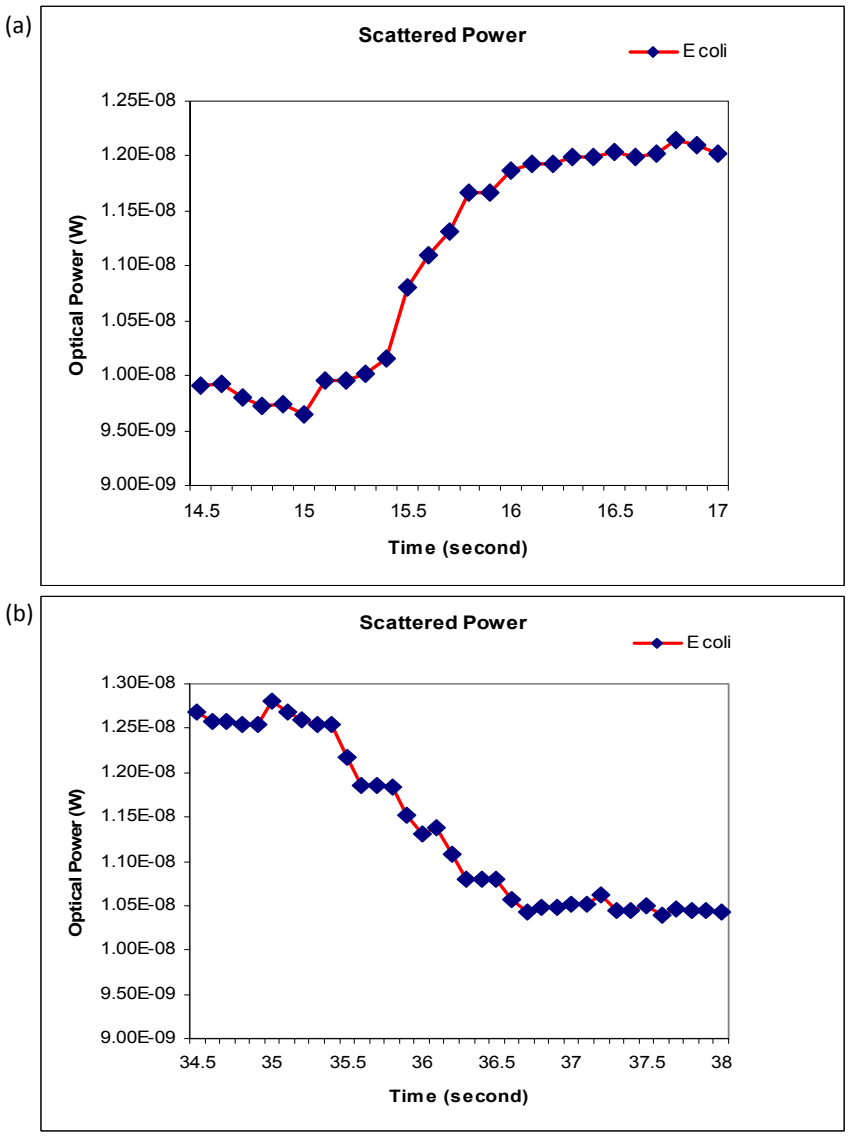

Figure 22. Rise and fall time of the optical scattering measurement at an angle of approximately 33 degrees. (a) Rise time of the bacteria alignment to the electric field is approximately 500 milliseconds. (b) Fall time of the bacteria alignment to the electric field is approximately 1.5 seconds.

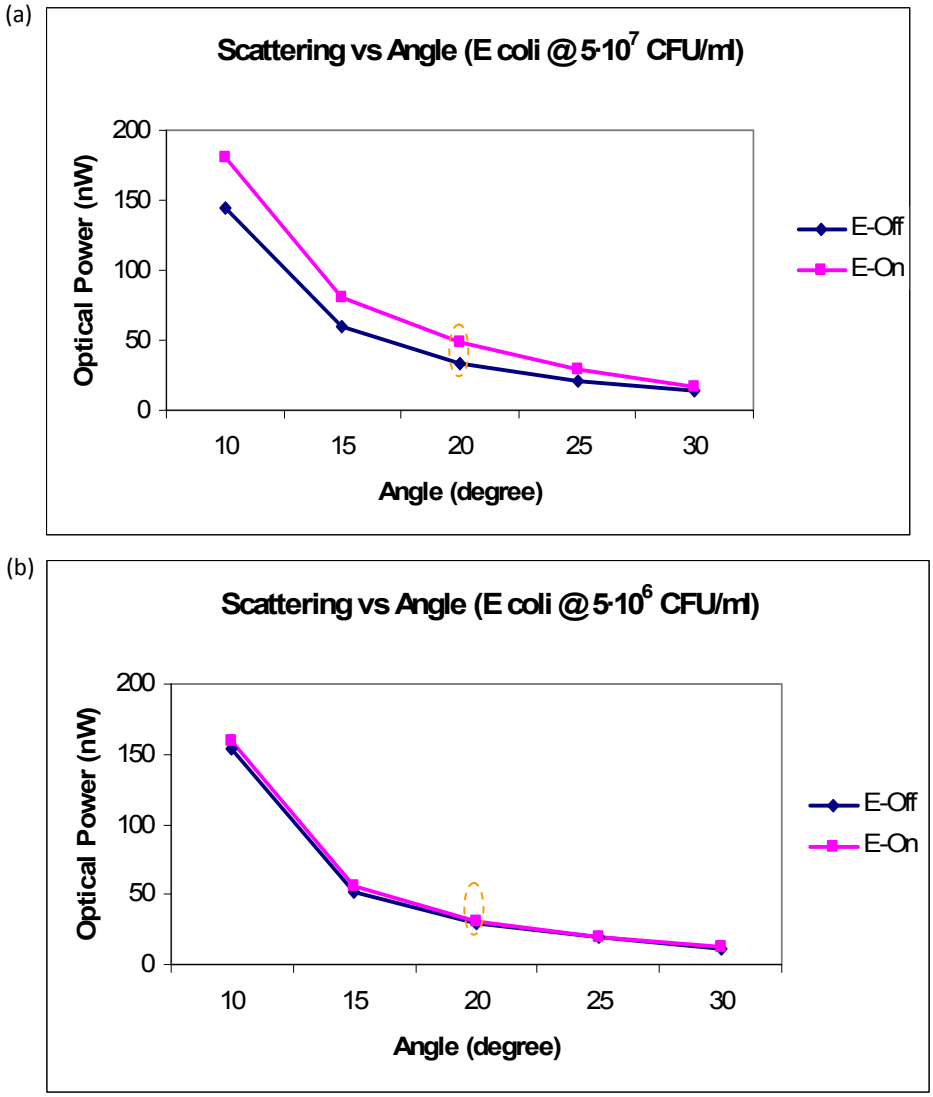

Figure 23. Optical scattering with respect to bacteria concentration and angle of detector. (a) The measurement with $5 \cdot 10^7$ CFU/mL live *E. coli*. On average, there is approximately a 20% signal increase with the electric field on versus off. At the detector angle of 20 degrees, the signal increase is approximately 44%. (b) The measurement with $5 \cdot 10^6$ CFU/mL live *E. coli*. On average, there is approximately a 5% signal increase with the electric field on versus off. At the detector angle of 15 degrees, the signal increase is approximately 8%.

D. Electrode patterning

1. Introduction

A critical component of many lab-on-a-chip applications is controlling particles within liquids [20, 21]. The detection scheme demonstrated in the previous section would benefit greatly from concentration and alignment of particles within liquids. For most applications, an external force is applied to accurately and reliably control particles through the microfluidic channel. Such forces have been demonstrated utilizing mechanical, electrical, thermal, and optical methods [22–29]. Electrical methods require the integration of electrodes to the microfluidic chip. If an electric field is applied between two electrodes on the same plane, a nonuniform electric field distribution is formed within the channel and the directionality and adaptability of the field is limited. Electrodes on all walls of microfluidic channels would be very beneficial in order to generate electric fields of any alignment for dielectrophoretic and electro-orientation purposes [30, 31]. This is explored in greater detail in section 3.

Dielectrophoresis (DEP) and electro-orientation allow for the manipulation and differentiation of different samples of interest through size, dielectric properties, and size asymmetry [32]. Recent studies of dielectrophoresis show its capability to separate different beads based on size and determine the dielectric properties of biological samples such as yeast, blood cells, and bacteria [30–35]. Recent studies of electro-orientation have revealed its ability to orient bacteria and nanowires [36–38]. Dielectrophoresis

provides for concentration and sorting capabilities [30–31, 35] and electro-orientation allows for the alignment of asymmetric particles on a macro scale [39].

Several methods for integration of electrodes with microfluidic channels have been developed. Electrodes forming the channel were demonstrated using highly doped silicon [40]. Electrodes on the walls of an elliptical microfluidic channel were demonstrated using multi-step optical lithography involving glass wet etching and metal deposition [41]. Vertical electrodes in the sidewall of a rectangular micro- or nano-fluidic channel were demonstrated using multi-step optical lithography involving SU-8 with metal deposition and electroplating [31, 42]. Single-step optical lithographic fabrication of microfluidic channels has been demonstrated [43] and simplicity in fabrication of electrodes has been demonstrated as well [44]. In this paper, we demonstrate a novel technique for the fabrication of electrodes in all four walls of the channel without increasing the complexity of its fabrication.

Electrodes are implanted onto the sidewall and topwall of the polydimethylsiloxane (PDMS) microfluidic channel through an ion-implanting process [45, 46]. The electrodes are connected across the borders by implanting into the PDMS at an angle and exhibit optical transparency over 35% [46]. Potential applications utilizing these electrodes within microfluidic channels are demonstrated by aligning and concentrating *E. coli* using electro-orientation and dielectrophoresis.

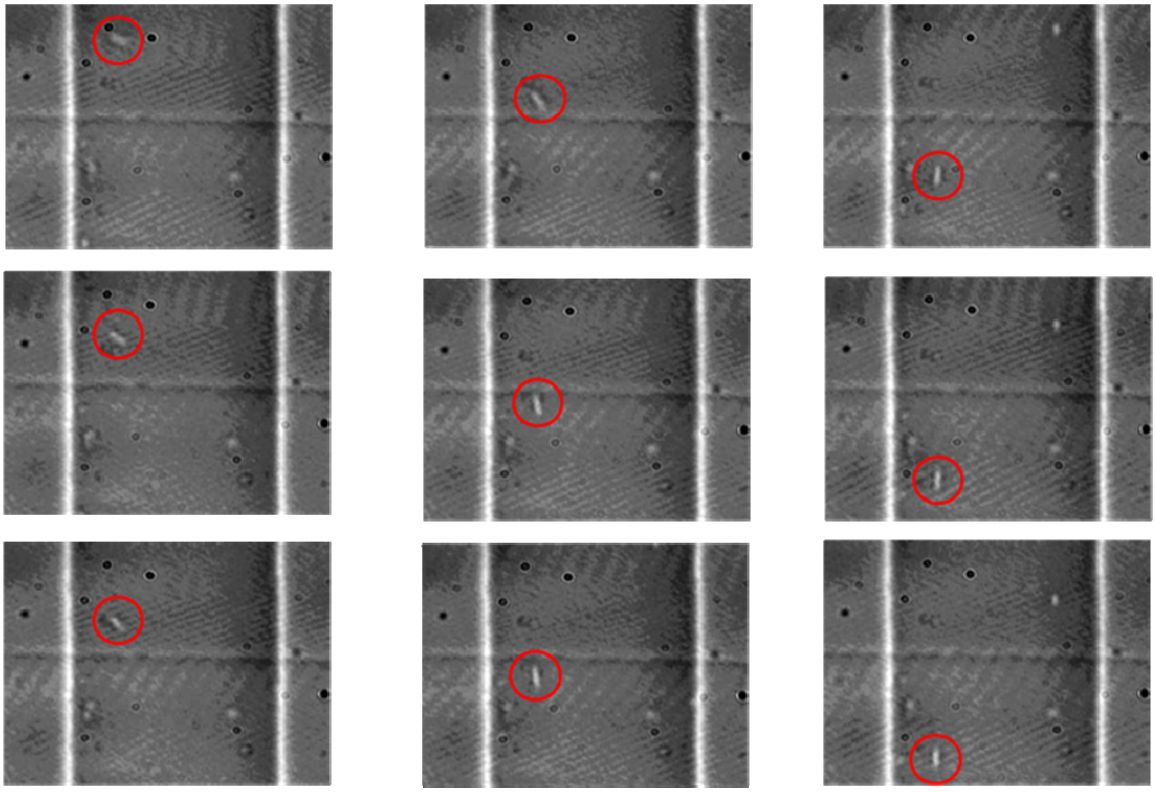

Figure 24. Bacteria in a microfluidic channel aligning to an electric field. The polydimethylsiloxane (PDMS) chip is placed on top of patterned electrodes. There is an electrode in the top of the image and another electrode below the image. The electric field is vertical. There is a very weak electric field on top of the electrode as most of the field lines are between the two electrodes. Initially, the bacteria are on top of an electrode (top left image). As the bacteria move into the area between the two electrodes (read each image down the first column, then second column and finally exits in the third column), they align to the electric field.

2. Chip design

A rectangular microfluidic channel of 100 μm in width, 70 μm in height, and approximately 2 cm in length is fabricated using the replica molding technique. A master mold is produced utilizing ultraviolet (UV) lithography with SU-8 (GM-1070, Gerstelec) on a silicon wafer. After trimethylchlorosilane (Sigma Aldrich) treatment of the master mold for 5 minutes, the PDMS (Dow Corning Sylgard 184) is poured onto the mold with a 10:1 base-to-curing agent ratio. After curing in an oven at 80ºC for 1 hour, the silicone is released from the mold. Next, we use low-energy metal ion implantation from a Filtered Cathode Voltage Arc (FCVA) source to coat the inside of the microfluidic channel with gold ions through a steel shadow mask, as shown in Figure 25. The ions form a layer of gold nanoparticles in the top 50 nm of the PDMS [45]. The main advantage of the implantation process is the excellent adhesion of the gold electrodes to the PDMS, since they are implanted a few nm below the surface. This adhesion can be verified by using Scotch tape on a PDMS surface with both sputtered and implanted gold. The Scotch tape will readily remove the sputtered gold from the PDMS surface while no noticeable change will occur to the implanted gold. The FCVA deposition is pulsed at 1 Hz. For each pulse, an arc is initiated between the gold cathode and the trigger electrode, creating adense plasma between the cathode and anode. After being filtered, the plasma is accelerated towards the sample, held at a bias of 2.5 keV. The gold ions are doubly charged, and the ion energy varies from 5 keV at the beginning of the pulse to 50 eV at the end of the pulse. The implantation process is explained in detail in references [45] and [46]. This procedure is repeated twice at a 40° angle to create mirror image electrodes within the fluidic channel, as shown in Figure 26(a). After the implantation, 4 gold

electrodes are sputtered on the surface in the 4 corners of the implanted area to ensure good electrical contact to the implanted layer.

We then lithographically pattern an ITO-coated glass slide (30–60 ohm/square, Sigma Aldrich) to create electrical contact with the gold-implanted region as well as provide electrodes for the open side of the microfluidic channel, as shown in Figure 26(b). Spin-on-glass (Honeywell) is coated onto specific regions of the ITO-coated glass slide to insulate the electrodes for the microfluidic channel from the gold-ion-implanted region of the PDMS. Inlet and outlet ports are punched into the PDMS with a hole-punching machine and the silicone is given the oxygen plasma treatment for 20 seconds at 50 W. Immediately afterwards, the silicone is bonded to the ITO-coated glass slide. The finished device is shown in Figure 27.

The finished chip contains 8 electrodes on the ITO. Half of the electrodes are used to manipulate particles within the microfluidic channel directly from the ITO-coated substrate. The other electrodes are utilized to make contact with the electrodes inside the PDMS microfluidics. When the electrodes on the PDMS walls and on the ITO are utilized independently, the applied electric fields are primarily in a plane parallel to the substrate. Each set of electrodes is capable of producing two separate orthogonal electric fields. Using a combination of the ITO electrodes and PDMS electrodes, the applied electric fields can be orthogonal to the plane of the substrate. In general, with this electrode configuration, we gain great flexibility in specifying the direction and distribution of the electric fields inside the fluidic channel. However, completely arbitrary

alignment of electric fields throughout the fluidic channel may require further structuring (such as arbitrary sidewall angles).

To apply the AC voltages to the electrodes, a function generator (HP 3312A) is utilized to generate frequencies between 1 Hz to 10 MHz at voltages up to 10 Vpp. The output of the function generator is connected to a custom circuit built to control the electrode voltages through a set of relays with the USB-controlled Velleman P8055. By connecting a selected set of electrodes to either output of the function generator through the PC, we can either float the electrode or set it to be one of the active applicators of the electric field. The schematic is shown in Figure 28.

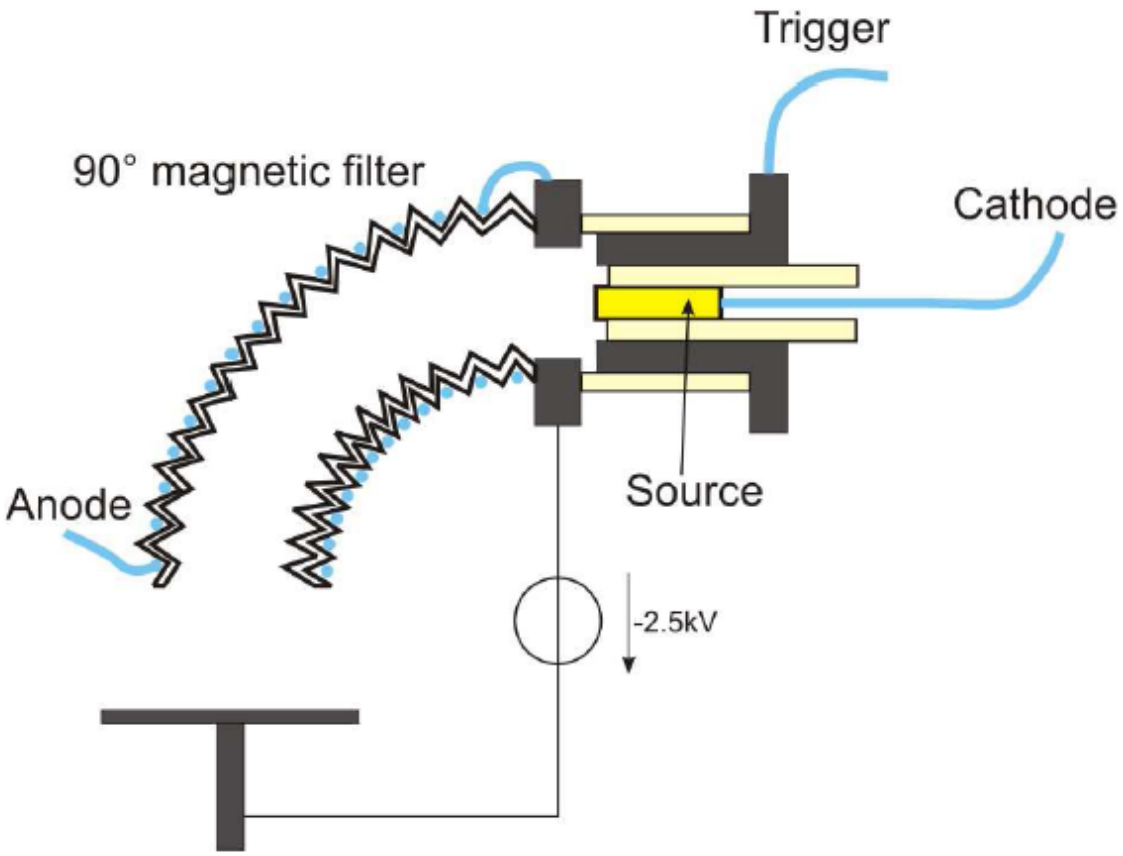

Figure 25. Implantation of metal ions. The source contains solid gold. Gold ions of various sizes are created at the source and the magnetic filter sorts the sizes of the gold ions. They are implanted about 1 to 50 nm into the PDMS surface at 2.5kV. (Source: [45])

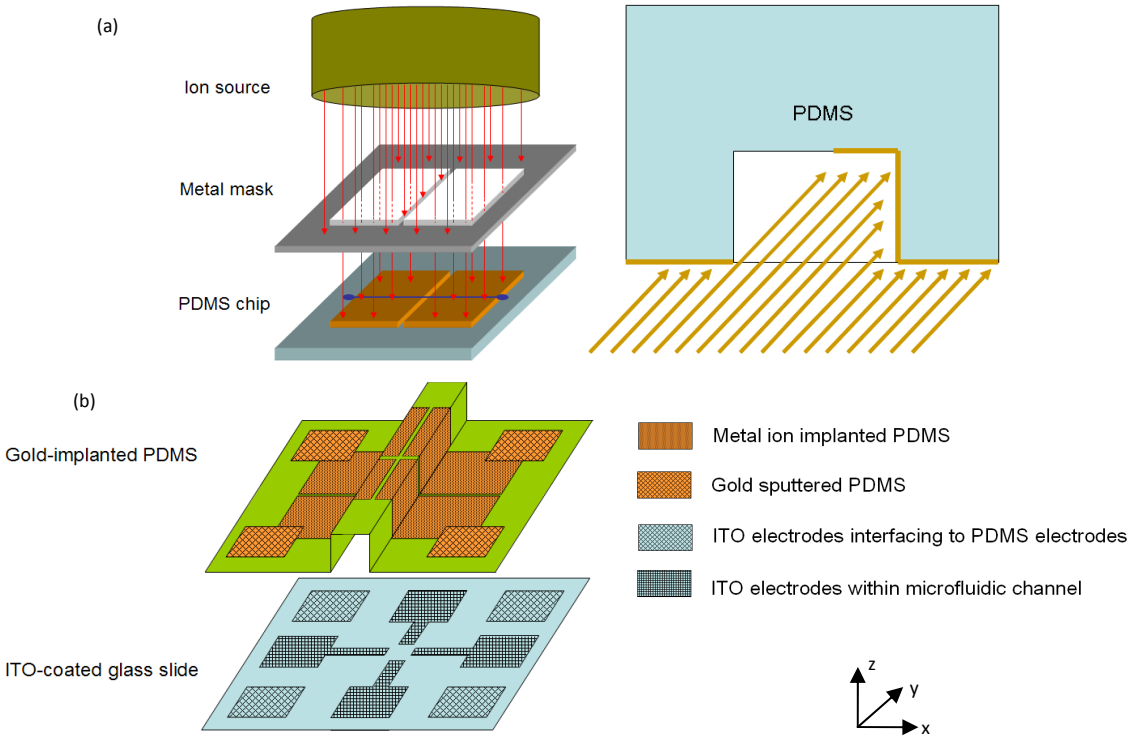

Figure 26. Schematic of the implantation of electrodes on the device. (a) The ions are implanted at an angle to create electrodes on the walls of the fluidic channel. (b) A lithographically patterned ITO-coated glass slide is bonded to the PDMS chip. Half of the electrodes on the ITO-coated glass slide connect to the PDMS electrodes.

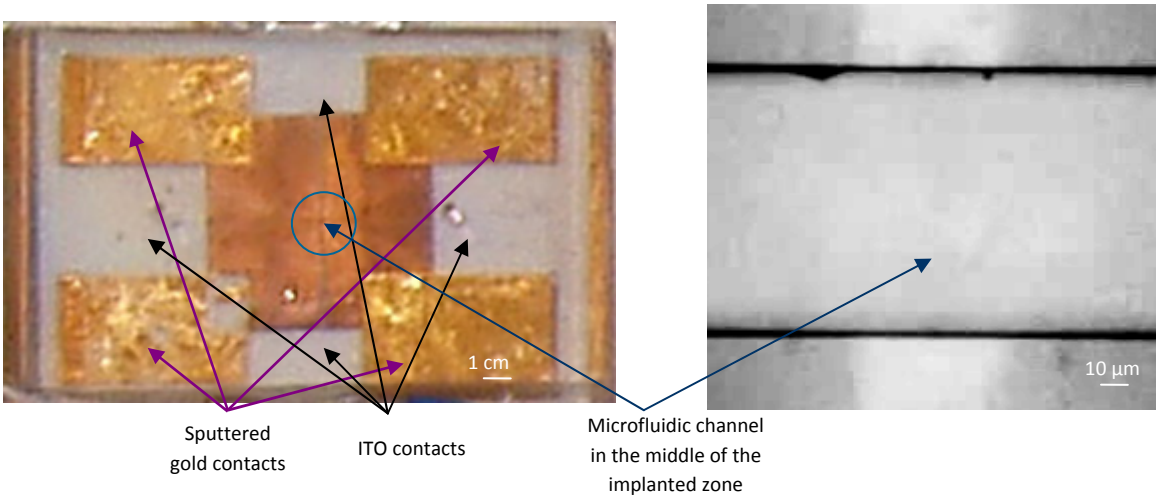

Figure 27. Picture of the device. The finished device and close-up image. In both images, the microfluidic channel runs from left to right between the sputtered gold contacts. In the close-up image, there are implanted gold electrodes on the left and right of the image.

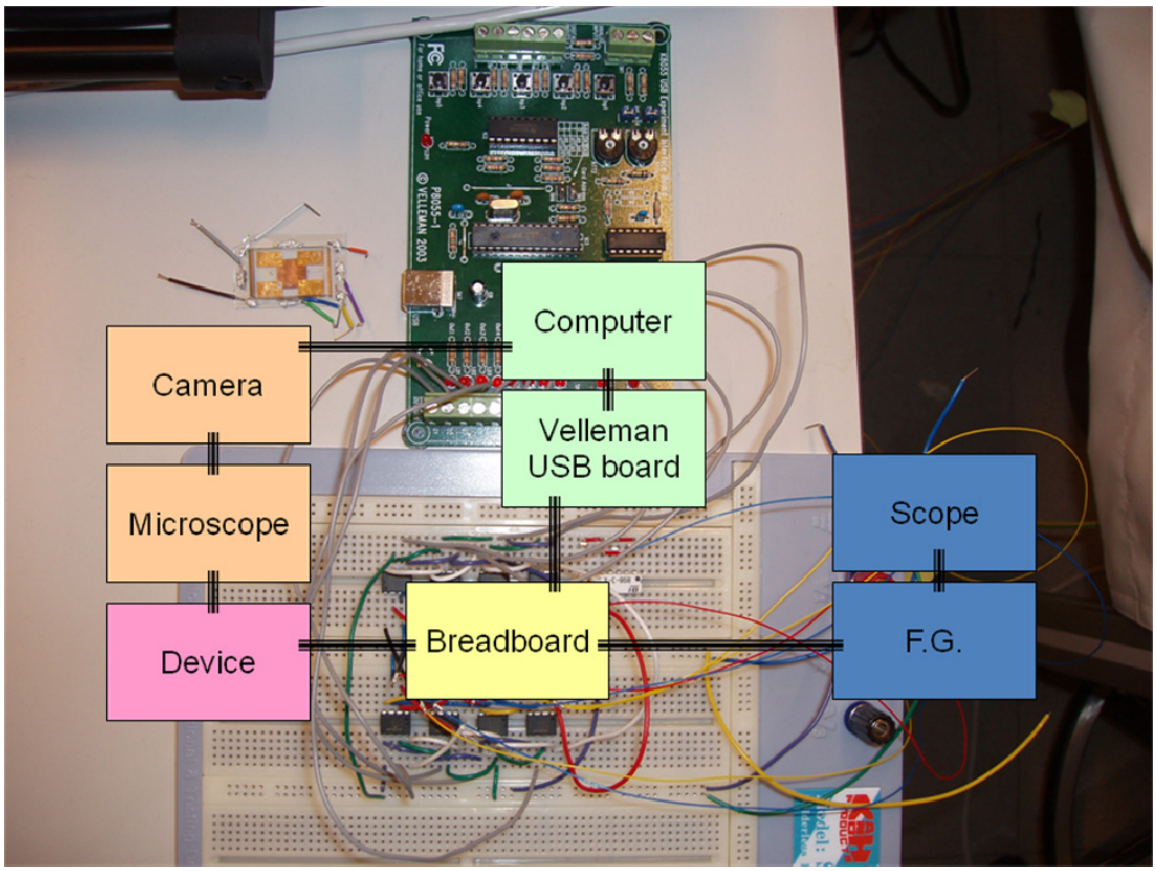

Figure 28. Schematic of setup. Electrical control of the device is done through the computer using a USB controller board. The device controls switches on the breadboard that turns on and off the input voltages from the function generator (F.G.).

3. Simulation

We can investigate the field distributions generated by three-dimensional structuring of electrodes within a fluidic channel through finite element simulations using the COMSOL software package. For a given electrode separation with only electrodes on the substrate, we note that the electric field distribution within the microfluidic channel is similar to the fringing fields of a capacitor. Depending on the height within the channel, the particle sees a significantly different magnitude of the electric field. Particles closer to the electrodes see at least a one-order-of-magnitude-higher electric field than particles closer to the top wall of the microfluidic channel (for a 50 μm channel height, this occurs when the particle's height is at 5 μm versus 45 μm). When the electrodes are coated on the PDMS, the maximum magnitude of the electric field seen by the particle is the same and in general the field itself is more uniform throughout the height of the fluidic channel.

The following parameters were utilized for the simulations: relative static permittivities of 2.8 for PDMS [47], 4.2 for the glass slide (given by COMSOL), and 80.1 for water within the fluidic channel [48] with ITO and gold-ion-implanted PDMS electrical conductivity of $2 \cdot 10^5$ Ω/m. We obtain this value by assuming the ITO is 100 nm thick and the gold-ion-implanted PDMS is 50 nm thick, while measuring the ITO sheet resistance to be 50 ohm/square and the gold-ion-implanted PDMS to be 100 ohm/square. For the first set of simulations, we assume a 100-μm-wide by 70-μm-tall fluidic channel that is 300 μm long. There are two electrodes on the top of the glass substrate that are spaced 100 μm apart. The fluidic channel is placed on top of this gap. There are also electrodes on the PDMS in the same configuration as the actual

implantation. Figure 29(a) shows 3 different slices in the height of the simulation of the electric field when only the electrodes on the substrate are utilized in height. Figure 29(b) shows the simulation of the electric field with all the electrodes utilized. The magnitude of the electric field remains uniform to within 5% throughout the entire height of the fluidic channel.

For the second set of simulations, we take a cross section with the fluidic channel moving liquids in and out of the plane. There is an electrode on the glass substrate as well as two electrodes on the walls of the PDMS. The gap between the two PDMS electrodes is 10 μm. We simulate the electric field generated orthogonal to the fluidic flow. Figure 30 shows the simulation of the electric field for the direction parallel to the substrate. Figure 31 shows the simulation of the electric field in the direction pointing from the substrate to the top of the fluidic chip. The electric field is not completely uniform throughout the microfluidic channel due to the coating of the top wall of the device. This can be visualized in Figure 32 by looking at the negative dielectrophoretic forces, which are the gradient of the electric field. There is a strong force pushing most of the particles in the channel experiencing negative dielectrophoretic forces down and towards the middle of the fluidic channel. There are two additional forces towards the top corners. However, the forces are quite weak in one direction and we visualize few bacteria in this region experimentally. This force will be addressed with greater detail in the experimental section.

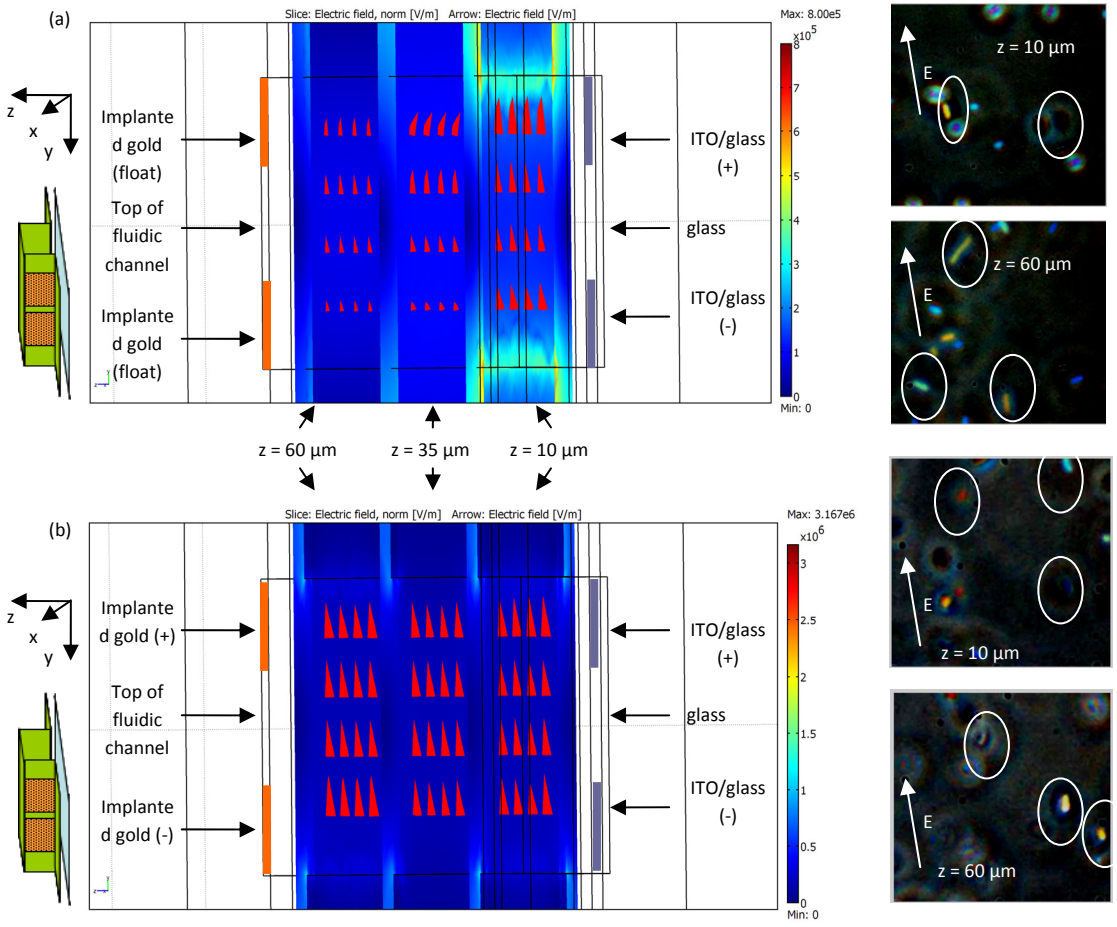

Figure 29. Simulation of electric field within a fluidic channel. PDMS surrounds the microfluidic channel except on the right-hand side of the image where the ITO-coated glass slide is located. (a) With planar electrodes on ITO-coated glass slide substrate only. Images to the right show *E. coli* aligned at different z planes. The ITO/glass is at z=0 µm and the top of the fluidic channel is at z=70 µm. At z=10 µm all the bacteria are aligned. At z=60 µm, the electric field does not orient all the bacteria. Some of the bacteria are on the substrate and do not move. They can be seen moving out of focus. (b) With electrodes on the microfluidic channel as well as the ITO-coated glass slide substrate. At both z=10 µm and z=60 µm, all flowing bacteria are aligned.

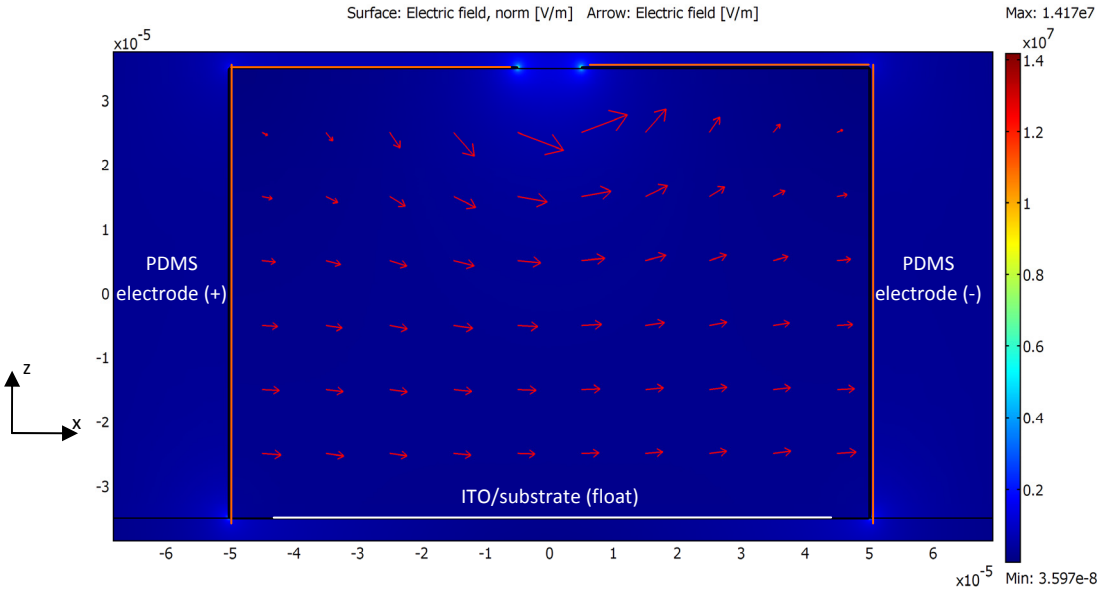

Figure 30. COMSOL simulation of electric field as the electric field is applied across the fluidic channel. The ITO-coated glass is the substrate on the bottom.

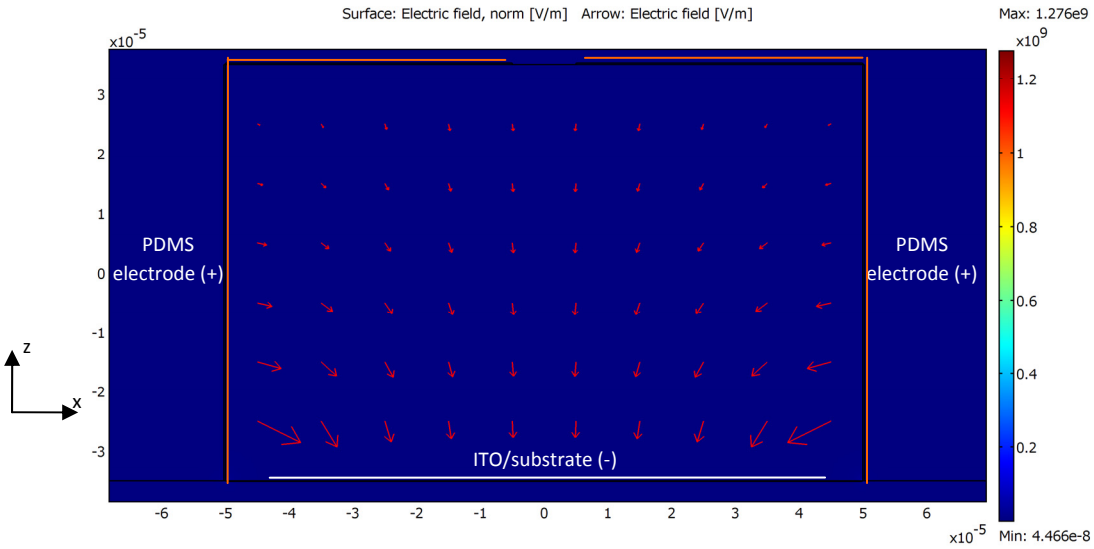

Figure 31. COMSOL simulation of electric field within a fluidic channel as the electric field is applied from the electrodes on the fluidic channel to the ITO-coated glass slide. PDMS is on the top, the left, and the right of the channel. The ITO-coated glass is the substrate on the bottom.

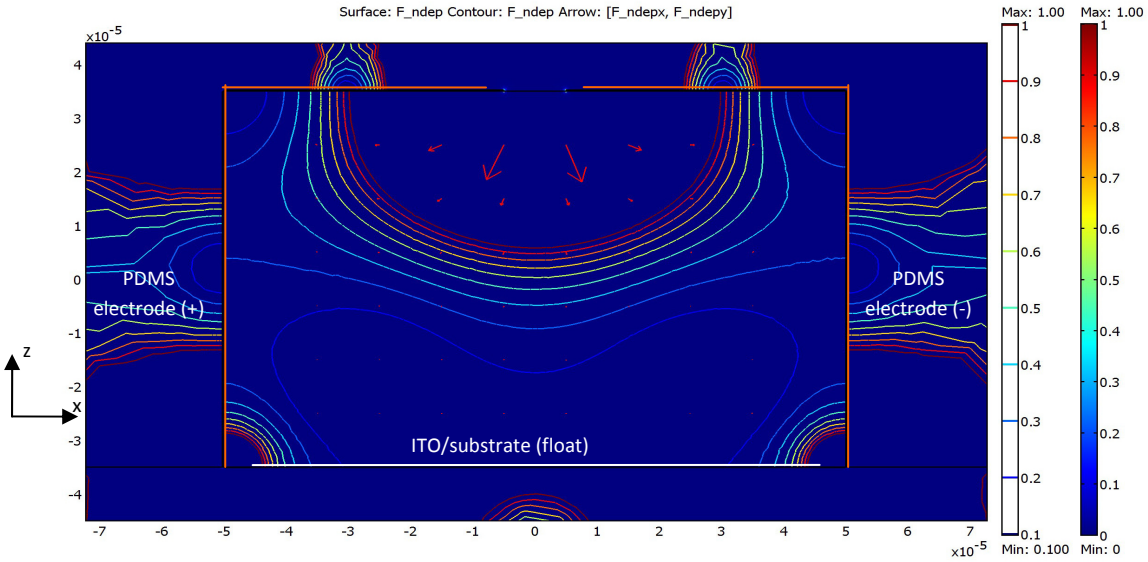

Figure 32. COMSOL simulation of the normalized negative dielectrophoresis forces experienced by a particle when the electric field is applied across the fluidic channel. PDMS is on the top, the left, and the right of the channel. ITO-coated glass is the substrate on the bottom.

4. Electro-orientation within a fluidic channel

Bacterial orientation within a microfluidic channel is possible through the electro-orientation force. This force is exerted on an asymmetric particle within a medium due to the application of an electric field. By applying an AC frequency where the particle has a dielectric permittivity higher than the medium, the particle will align along the field [33]. We can align the bacteria to any of the axial directions by simply applying the electric fields along the proper electrodes. This type of measurement is useful, for example, when an asymmetric sample of interest is located at a known position and the precise height, width and length of the particle need to be determined. Also, it is possible to flow the particle over a sensing structure in a particular orientation if one is interested in a particular viewing angle of the sample of interest, for example, the flagellum. This technique may be especially useful when probing particular entities within a biological cell, in particular, to orient microtubules [49].

We utilize the same parameters as have been shown in the electro-orientation techniques of *E. coli* K12 in filtered urine described in previous work to align the bacteria to the electric field [36]. 10 Vpp at 10 MHz is applied across two electrodes to obtain a preferred alignment. Live bacteria are flowed horizontally from right to left within the microfluidic channel at a rate of 20 μm/sec. Figure 33(a) shows bacteria aligned to a horizontally applied electric field. Figure 33(b) shows bacteria aligned to an electric field with both vertical and horizontal components. Figure 33(c) shows bacteria aligned to an electric field which is applied in and out of the plane. Without an applied electric field, most bacteria prefer to align horizontally along the direction of flow.

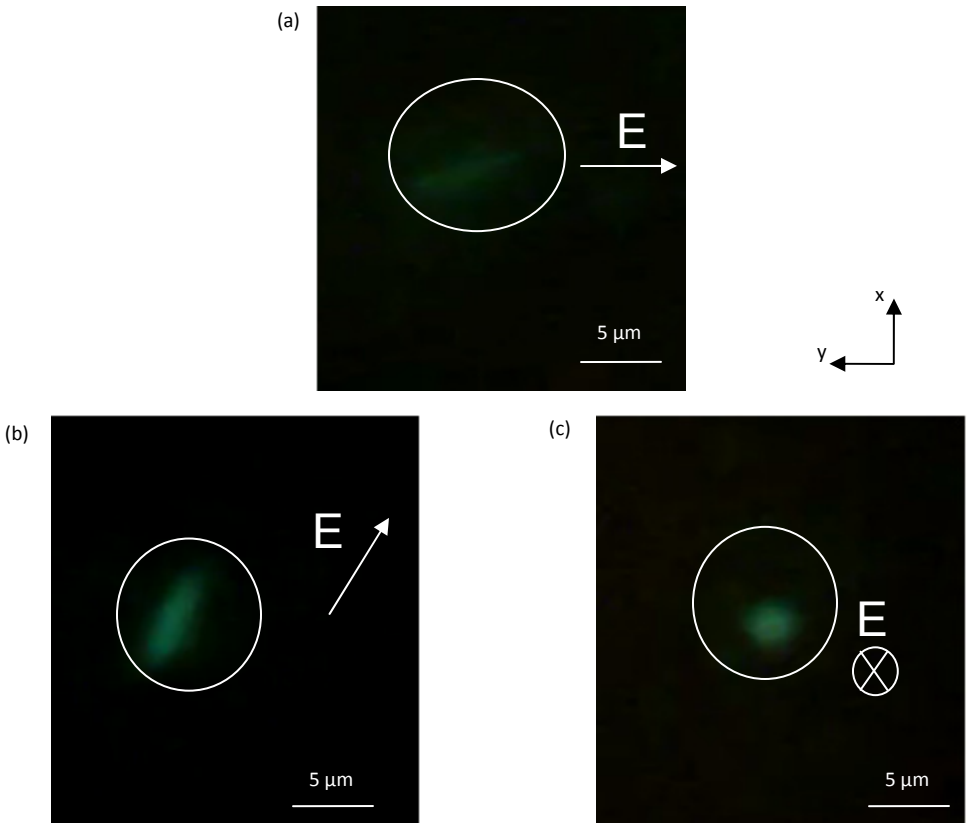

Figure 33. Demonstration of bacteria orientation. The white arrows indicate the direction of the applied electric field. The SYTO 9 fluorescence-labeled bacterium is also aligned in this direction. White circles mark live bacterium which are currently in fluidic channel. (a) The electric field is applied in the horizontal direction. (b) The electric field is applied with both vertical and horizontal components. (c) The electric field is applied in and out of the image plane. Electrodes are not shown.

5. Dielectrophoresis within a fluidic channel

Colloidal focusing within a microfluidic channel is possible through the dielectrophoretic force. This force is exerted on a particle within a medium due to the application of a non-uniform electric field. By utilizing an AC frequency where the particle has a dielectric permittivity lower than the medium, the particle will move towards where the fields are weakest [32, 41]. We utilize this force to move particles to the middle of the rectangular microfluidic channel. This is advantageous where a sample of interest flows over a sampling region which is much smaller than the size of the fluidic channel. This can be especially useful for sparse suspensions as the colloids will be concentrated in the middle of the region. A key advantage of this approach over fluidic flow focusing is the ability to flow colloidal solutions at a slower rate without losing any focusing capability. This may be especially useful for lab-on-a-chip application that combines larger microfluidic channels with smaller structures.

We change the conductivity of the solution from filtered urine (>1 mS/cm) to deionised water with $CaCl_2$ salt (170 μS/cm) and apply a frequency of 1 MHz to obtain negative dielectrophoresis. 10 Vpp is applied across the two PDMS side wall and top wall electrodes. Bacteria flow horizontally from right to left within the microfluidic channel at a rate of 10 micron/sec. Figure 34(a) shows no field applied. Figure 34(b) shows bacteria in the center of the fluidic channel due to the field being applied on the electrodes to the right-hand side. This concentration occurs as the bacteria flow along the channel from the side wall electrodes. Figure 35 shows the bacteria counts for a certain distance from the center of the fluidic channel. We estimate that the bacteria are being

concentrated to within about 25 microns of the center. This corresponds to an increase in the concentration by about 15 times. This is similar to the concentration of microbeads and human leukemia cells with 10 Vpp at 10–100 kHz in [41].

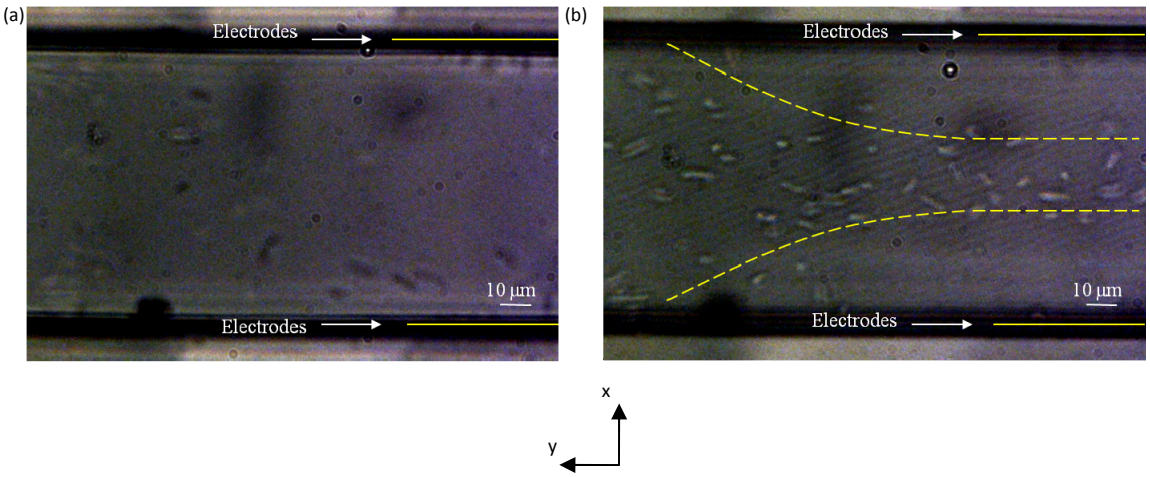

Figure 34. Demonstration of bacteria concentration. The fluidic channel contains 4 electrodes in this picture with the bacterial solution entering from the right. An electric field can be applied on the right-hand-side electrodes from the top of the fluidic channel to the bottom of the fluidic channel. (a) The electric field is not applied. Bacteria come into the picture from the right without preference for focusing within the fluidic channel or focal plane. (b) The electric field is applied on the noted right-hand-side electrodes. Bacteria come into the picture from the right in the center of the fluidic channel at the same focal plane. Note that the electric field is not applied on the left-side electrodes. The bacteria immediately redisperse in both focal plane and within the fluidic channel as marked by the dashed lines.

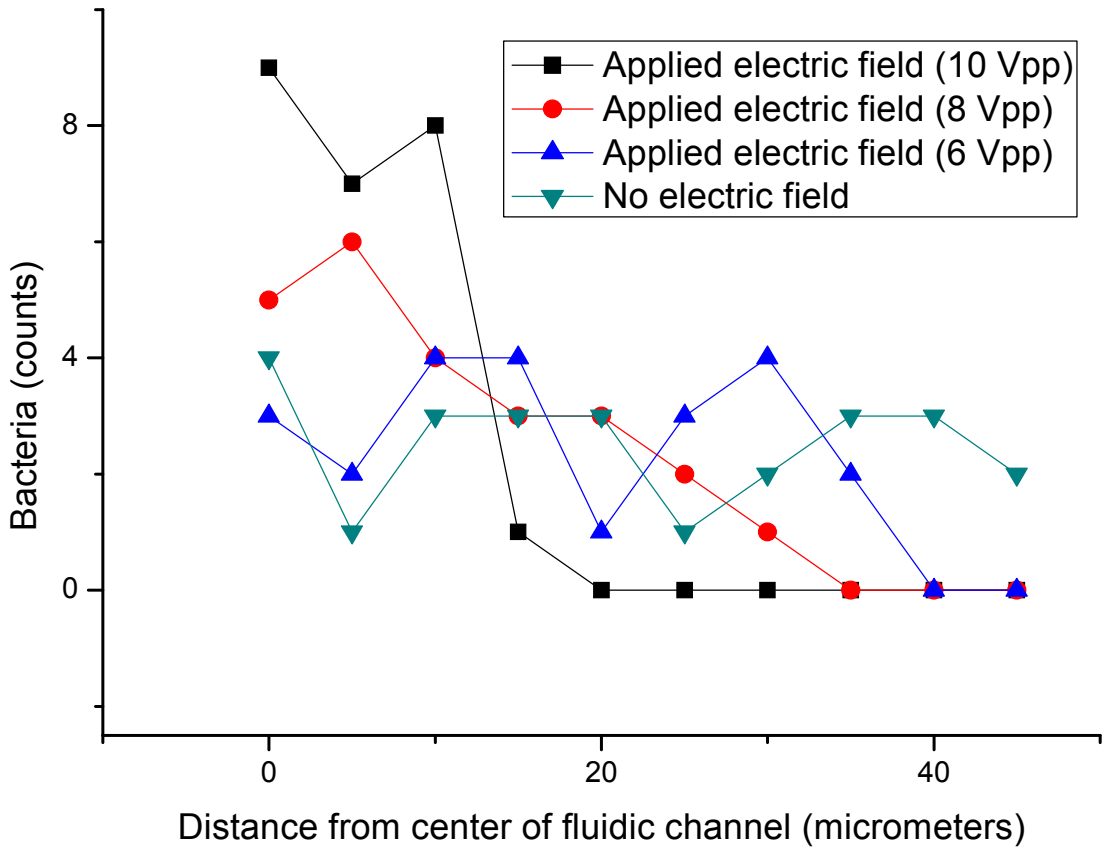

Figure 35. Data showing bacteria concentration with respect to applied electric field strength. As each bacteria enters the picture, the distance from the center of the fluidic channel is measured. Note that most bacteria are concentrated to within 10 μm of the center when the electric field is applied at 10 Vpp compared to a random distribution when no electric field is applied. Voltages lower than 4 Vpp resulted in a similar profile to no electric field.

E. References

1. World Health Organization, 2003 Annual Report.
2. Conventional methods of E coli detection, image of an urine culture test and dipstick test, http://labmed.bwh.harvard.edu/microbiology/teaching/cases/bacteriology/ecoli/.
3. Conventional methods of E coli detection, image of a dipstick test, http://www.brooksidepress.org/.
4. Iris Diagnostics iQ 200 Series Automated Urinalysis System.
5. Gunasekera TS, Attfield PV, Veal DA. A flow cytometry method for rapid detection and enumeration of total bacteria in milk. Applied and Environmental Microbiology 66, 1228–1232 (2000).
6. Sloper AN, Deacon JK, Flanagan MT. A planar indium phosphate monomode waveguide evanescent field immunosensor. Sensors and Actuators B: Chemical 1, 285–297 (1990).
7. Cullen DC, Brown RGW, Lowe CR. Detection of immune-complex formation via surface plasmon resonance on gold-coated diffraction gratings. Biosensors 3, 211–225 (1987–1988).
8. Schneider BH, Edwards JG, Hartman NF. Hartman interferometer: versatile integrated optic sensor for label-free, real time quantification of nucleic acids, proteins, and pathogens. Clinical Chemistry 43, 1757–1763 (1997).
9. Wyatt PJ, Phillips, DT. Structure of single bacteria from light scattering. Journal of Theoretical Biology 37, 493–501 (1972).
10. Katz A, Alimova A, Xu M, Rudolph E, Shah MK, Savage HE, Rosen RB, McCormick SA, Alfano RR. Bacteria size determination by elastic light scattering. IEEE Journal of Quantum Electronics 9, 277–287 (2003).
11. Brunsting A, Mullaney PF. Differential light scattering from spherical mammalian cells. Biophysical Journal 14, 439–453 (1974).
12. Perelman LT, Backman V, Wallace M, Zonios G, Manoharan R, Nusrat A, Shields S, Seiler M, Lima C, Hamano T, Itzkan I, Van Dam J, Crawford JM, Feld MS. Observation of periodic fine structure in reflectance from biological tissue: a new technique for measuring nuclear size distribution. Physical Review Letters 80, 627–630 (1998).
13. Finnigan JA, Jacobs DJ. Light scattering by ellipsoidal particles in solution. Journal of Physics D: Applied Physics 4, 72 (1971).
14. Gomez-Sjoberg R, Morisette DT, Bashir R. Impedance microbiology-on-a-chip: microfluidic bioprocessor for rapid detection of bacterial metabolism. IEEE J MEMS 14, 829–838 (2005).

15. Bhunia AK, Lathrop A. Pathogen Detection, Food-borne (McGraw-Hill, New York, NY, 2003).

16. Homola J, Yee SS, Gauglitz G. Surface plasmon resonance sensors: review. Sens. Actuators B 54, 3–15 (1999).

17. Gauthier C, St-Pierre Y, Villemur R. Rapid antimicrobial susceptibility testing of urinary tract isolates and samples by flow cytometry. J. Med. Microbiol. 51, 192–200 (2002).

18. Roberts K, Parameswaran M, Moore M, Muller RS. A silicon microfabricated aperture for counting cells using the aperture impedance technique. Can. J. Elect. Comput. Eng. 24, 109–113 (1999).

19. Pezzlo M. Detection of urinary tract infections by rapid methods. Clin. Microbiol. Rev. 1, 268–280 (1988).

20. Whitesides GM. The origins and future of microfluidics. Nature 442, 368–373 (2006).

21. Psaltis D, Quake SR, Yang C. Developing optofluidic technology through the fusion of microfluidics and optics. Nature 442, 381–386 (2006).

22. Unger MA, Chou HP, Thorsen T, Scherer A, Quake SR. Monolithic microfabricated valves and pumps by multilayer soft lithography. Science 288, 113–116 (2000).

23. Thorsen T, Maerkl SJ, Quake SR. Microfluidic large-scale integration. Science 298, 580–584 (2002).

24. Erickson D, Li D. Integrated microfluidic devices. Anal. Chim. Acta 507, 11–26 (2004).

25. Yamahata C, Chastellain M, Parashar VK, Petri A, Hofmann H, Gijs MAM. Plastic micropump with ferrofluidic actuation. J. Microelectromech. Syst. 14, 96–102 (2005).

26. Darhuber AA, Valentino JP, Troian SM, Wagner S. Thermocapillary actuation of droplets on chemically patterned surfaces by programmable microheater arrays. J. Microelectromech. Syst. 12, 873–879 (2003).

27. Stone HA, Stroock AD, Ajdari A. Engineering flows in small devices. Annu. Rev. Fluid Mech. 36, 381–411 (2004).

28. Boyd DA, Adleman JR, Goodwin DG, Psaltis D. Chemical separation by bubble-assisted interphase mass transfer. Anal. Chem. 80, 2452–2456 (2008).

29. Krishnan M, Park J, Erickson D. Optothermorheological flow manipulation. Opt. Lett. 34, 1976–1978 (2009).

30. Park BY, Madou MJ. 3-D electrode designs for flow-through dielectrophoretic systems. Electrophoresis 26, 3745–3757 (2005).

31. Wang L, Flanagan LA, Monuki E, Jeon NL, Lee AP. Dielectrophoresis switching with vertical sidewall electrodes for microfluidic flow cytometry. Lab on a Chip 7, 1114–1120 (2007).

32. Jones TB. Basic theory of dielectrophoresis and electrorotation. IEEE Engineering in Medicine and Biology Magazine 22, 33–42 (2003).

33. Miller RD, Jones TB. Electro-orientation of ellipsoidal erythrocytes. Biophys. J. 64, 1588–1595 (1993).

34. Gascoyne P, Mahidol C, Ruchirawat M, Satayavivad J, Watcharasit P, Becker FF. Microsample preparation by dielectrophoresis: isolation of malaria. Lab on a chip 2, 70–75 (2002).

35. Yang L, Banada PP, Chatni MR, Lim KS, Bhunia AK, Ladisch M, Bashir R. A multifunctional microfluidic system for dielectrophoretic concentration coupled with immunocapture of low numbers of Listeria monocytogenes. Lab on a chip 6, 896–905 (2006).

36. Choi JW, Pu A, Psaltis D. Optical detection of asymmetric bacteria utilizing electro orientation. Opt. Express 14, 9780–9785 (2006).

37.Jamshidi A, Pauzauskie PJ, Schuck PJ, Ohta AT, Chiou PY, Chou J, Yang P, Wu MC. Dynamic manipulation and separation of individual semiconducting and metallic nanowires. Nature Photonics 2, 86–89 (2008).

38. Choi W, Nam SW, Hwang H, Park S, Park JK. Programmable manipulation of motile cells in optoelectronic tweezers using a grayscale image. Appl. Phys. Lett. 93, 143901 (2008).

39. Lu ZX, Wood LF, Ohman DE, Collinson MM. Bio-inspired chemical reactors for growing aligned gold nanoparticle-like wires. Chem. Commun. 28, 4200–4202 (2009).

40. Iliescu C, Xu GL, Samper V, Tay FEH. Fabrication of a dielectrophoretic chip with 3D silicon electrodes. J. Micromech. Microeng. 15, 494–500 (2005).

41. Yu C, Vykoukal J, Vykoukal DM, Schwartz JA, Shi L, Gascoyne PRC. A three-dimensional dielectrophoretic particle focusing channel for microcytometry applications. J. Microelectromech. Syst. 14, 480–487 (2005).

42. Nichols KP, Eijkel JCT, Gardeniers HJGE. Nanochannels in SU-8 with floor and ceiling metal electrodes and integrated microchannels. Lab on a chip 8, 173–175 (2008).

43. Duffy C, McDonald JC, Schueller OJA, Whitesides GM. Rapid prototyping of microfluidic systems in polydimethylsiloxane. Anal. Chem. 70, 4974–4984 (1998).

44. Stark RW, Stalder MS, Stemmer A. Microfluidic etching driven by capillary forces for rapid prototyping of gold structures. Microelectron. Eng. 67-68, 229–236 (2003).

45. Rosset S, Niklaus M, Dubois P, Shea H. Mechanical characterization of a dielectric elastomer microactuator with ion-implanted electrodes. Sens. Actuators, A 144, 185–193 (2008).

46. Rosset S, Niklaus M, Dubois P, Shea HR. Metal ion implantation for the fabrication of stretchable electrodes on elastomers. Advanced Functional Materials 19, 470–478 (2009).

47. Mark, JE., editor. Polymer data handbook, 2nd edition (Oxford University Press, New York, NY 2009).

48. CRC Handbook of Chemistry and Physics 89th edition (CRC Press, Boca Raton, FL 2008).

49. Minoura I, Muto E. Dielectric measurement of individual microtubules using the electroorientation method Biophys. J. 90, 3739–3748 (2006).

IV. Plasmonic optofluidics

A. Introduction

In the previous chapter, we discussed detection schemes of bacteria and some methods of pre-concentration and arbitrary alignment. In bacteria manipulation, active fluidic pumping is a key component [1, 2]. The motion of the fluid allows for additional bacteria to be moved into the active region. Traditionally in soft-lithography-compatible microfluidics, solenoid pumps control valves and fluids [3, 4]. These solenoid pumps are large, bulky devices that are usually larger than the size of the chip themselves. In the quest for further miniaturization, integrated means of pumping liquids have been sought. These alternative methods have focused on optical, electrical, magnetic, and thermal means, as well as various combinations of the above-mentioned methods [5–18]. In this chapter, development of optical methods of fluidic control with plasmonic nanoparticles will be discussed.

1. Plasmonic nanoparticles as thermal sources

Classically, plasmons are the oscillation of electrons with respect to fixed positive ions in a metal. In metals, there is damping of the oscillation of the electrons. This damping results in degeneration of input energy into thermal energy. To maximize the conversion efficiency of the input energy to the heat, it is ideal to match the input energy source to the plasmon resonance of the metal. At the resonance, the electrons can follow the electric field of the input laser source and the conversion efficient to heat is maximized.

For use with visible lasers, spherical gold nanoparticles are ideal, as their absorption is maximum at about 510–550 nm, depending on their size. For particles larger than about 35 nm, scattering is much larger than absorption, whereas, for particles smaller than 15 nm, absorption dominates. For use with infrared lasers, gold nanorods are ideal, as the plasmon resonance is dependent on the longer axis of the nanorod. Common values for absorption maximum for gold nanorods can be found for 750–900 nm which have lengths of 35–50 nm. [19]

2. Optically controlled fluidic valves

In similar lines to the interest in controlling colloids within channels, optofluidics [1] has resulted in several methods of controlling fluidics utilizing optical methods [5–9]. An optical method for providing this circuitry can ease the design criteria of these lab-on-a-chip applications if the fluidic valves do not need to be created during device fabrication. An optically controlled fluidic valve can be opened and closed as well as rapidly reconfigured, by manipulating the optical beam. Optically controlled fluidic valves have been created utilizing photothermal nanoparticles [5], an IR-based laser [6], plasmonic nanoparticles coated on the substrate [7], and fluidic gelation through energy transfer from an optically absorbing substrate [8, 9]. In this chapter, we focus on the biological and chemical compatibility of plasmonic nanoparticles as thermal source used in [5]. The technology used in this particular example of the optofluidic pump is described in further detail in Figure 36.

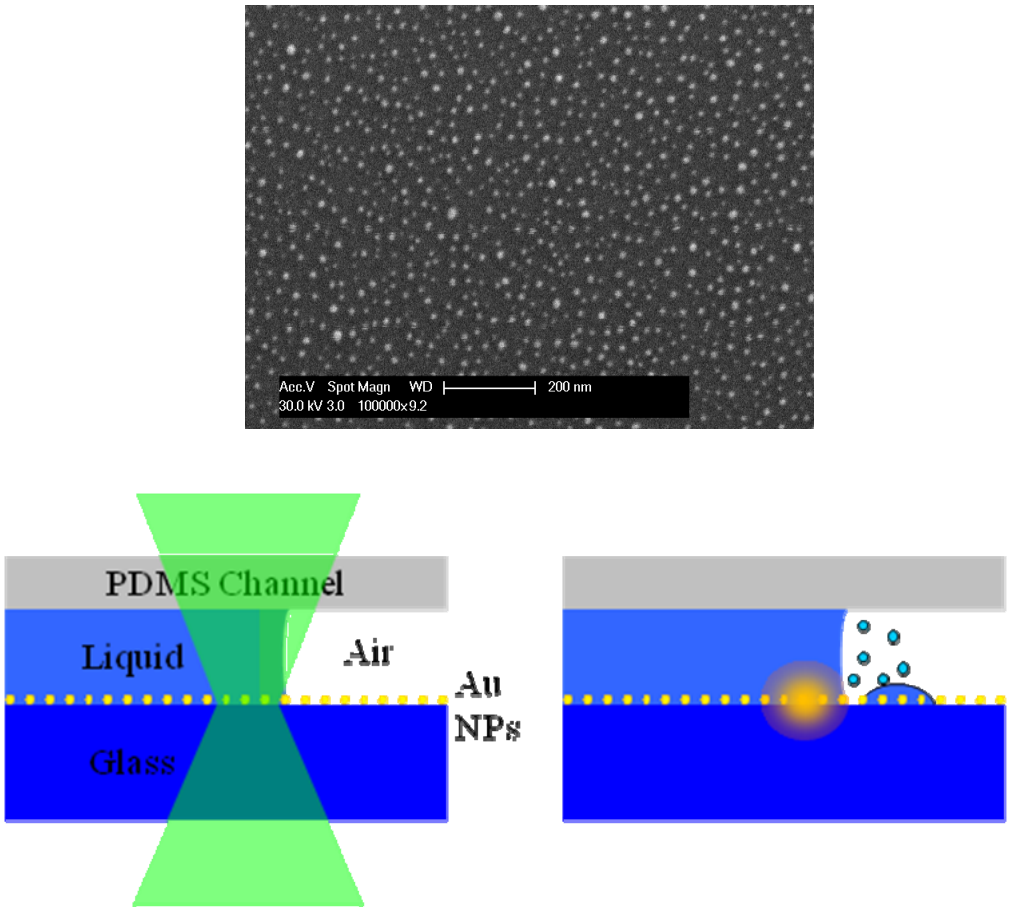

Figure 36. Technology used in the optofluidic pump. Block copolymer lithography is used to create a single monolayer of approximately 15 nm gold nanoparticles. They are spaced approximately 40 nm apart from each other due to an organic polymer between each pair of nanoparticles. The organic polymers are removed using oxygen plasma. The resulting scanning electron microscope image is shown on top. When liquid is flowed over this substrate in a confined space such as a microfluidic channel, we are able to change the temperature, which in turn changes the vapor pressure. The differential vapor pressure causes evaporation to occur near the laser spot and condensation away from the laser spot.

B. Biological compatibility of plasmonic optofluidic valves

1. Optofluidic pump background

The schematic diagram and creation of a vapor bubble with the optofluidic pump is shown in Figure 37 and Figure 38. The microfluidic chip is a standard microfluidic channel, 30 microns wide by 10 microns tall. The green laser is integrated into the microscope. The thermal energy transfer from the green laser to the liquid is enhanced by depositing a monolayer of gold nanoparticles at the floor of the fluidic channel. The plasmon resonance of the particles matches the green laser wavelength.

In a previous work [7], single fluidic valves were created where liquid was pumped using these optothermal particles. A key component in these fluidic pumps is the necessity of a vapor pressure change with respect to temperature for the primary liquid utilized. While water, ethanol, and various other organic solvents can be pumped using this technique, most chemicals and biological compounds will become concentrated or diluted at the interface [20, 21].

In this section, we show how these fluidic valves can be used to increase complexities and to concentrate bacteria. In Figure 39, we show the different complexities that are possible. After the bacteria are concentrated to an acceptable number, we use our previous method of aligning the bacteria and detect the optical scattering signal from the bacteria to quantify the concentration.

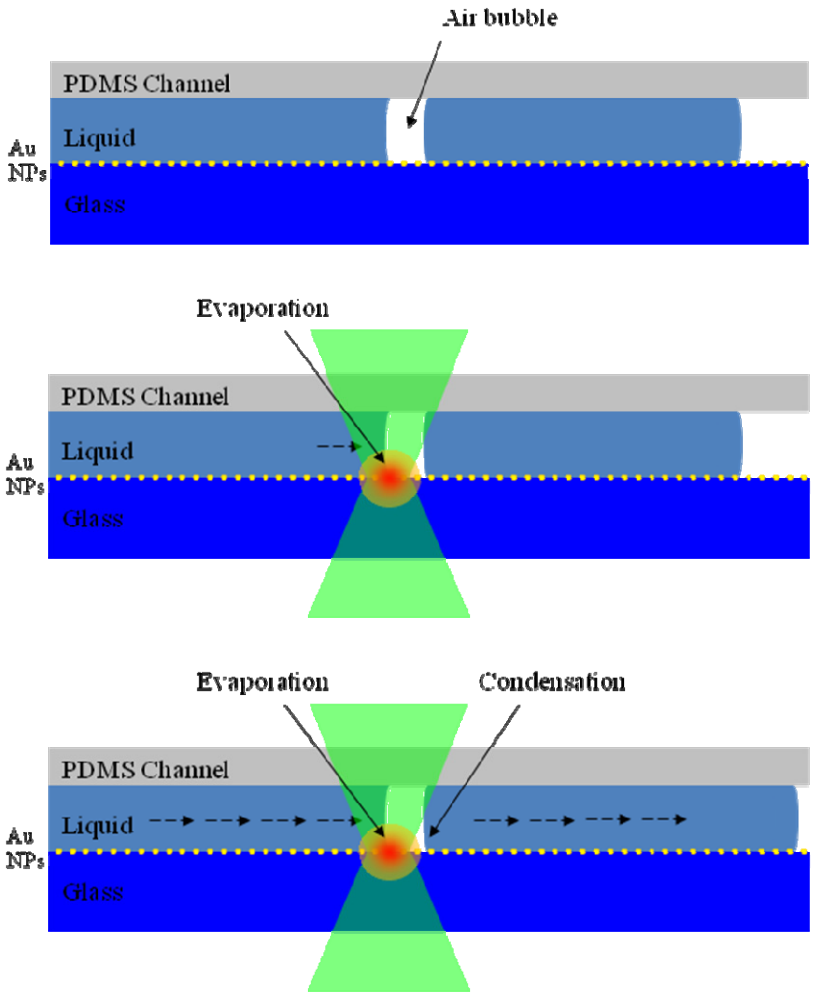

Figure 37. Schematic of optofluidic pump. After the air bubble is created, liquid exists on both sides of the air bubble with the left-hand side connected to a reservoir of liquid (top image). When the laser is located at one of the interfaces, there is a thermal gradient corresponding to the laser spot (central image). This creates a different vapor pressure on the two interfaces. This leads to mass transfer of water from one interface (with the laser spot) to the other spot (without the laser spot). This results in liquid pumping action (bottom image).

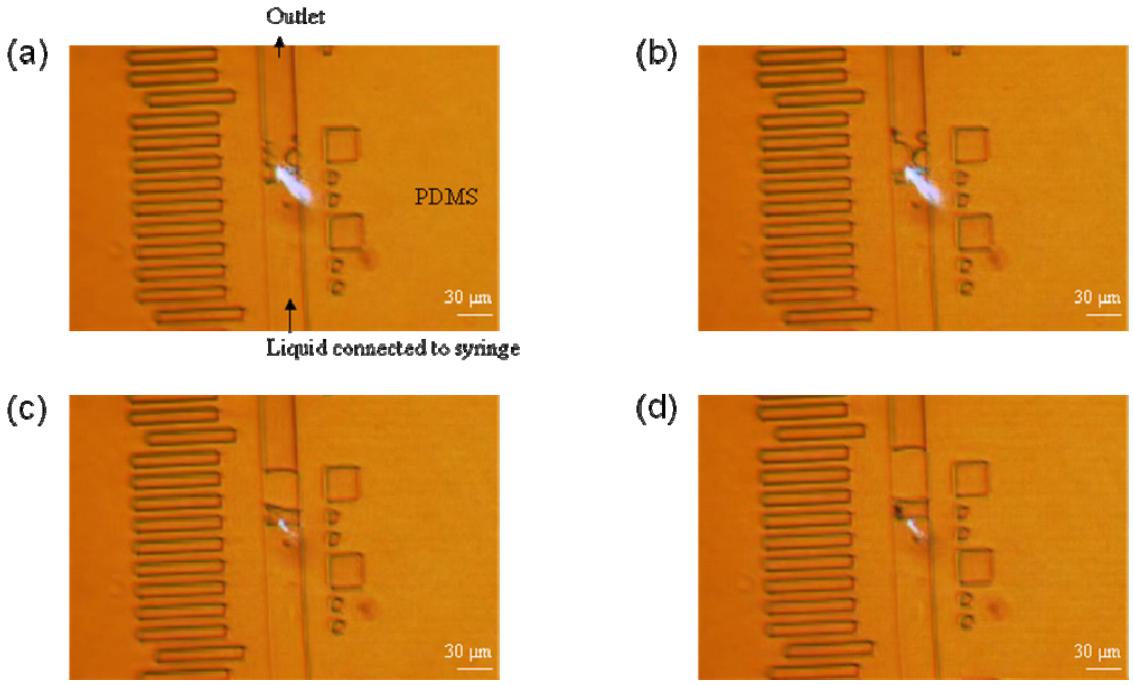

Figure 38. Image showing the creation of the vapor bubble. The fluidic channel is in the center, approximately 30 microns wide and 10 microns tall. On the left are markers, 10 microns wide each, with a displaced marker every 200 microns. On the right are additional markers. They are used to evaluate how far the liquid moves. The liquid, which comes from a syringe, is connected at the bottom of the picture. On the top of the pictures, there is air and there is an interface between the liquid and the air at the location of the laser spot. (a) Condensed droplets of water appear on the air side of the water-air interface. (b) More water is transferred across the interface as the water droplets get larger. (c) The droplets connect to each other. (4) Water is pumped across the interface as the vapor bubble remains relatively stable.

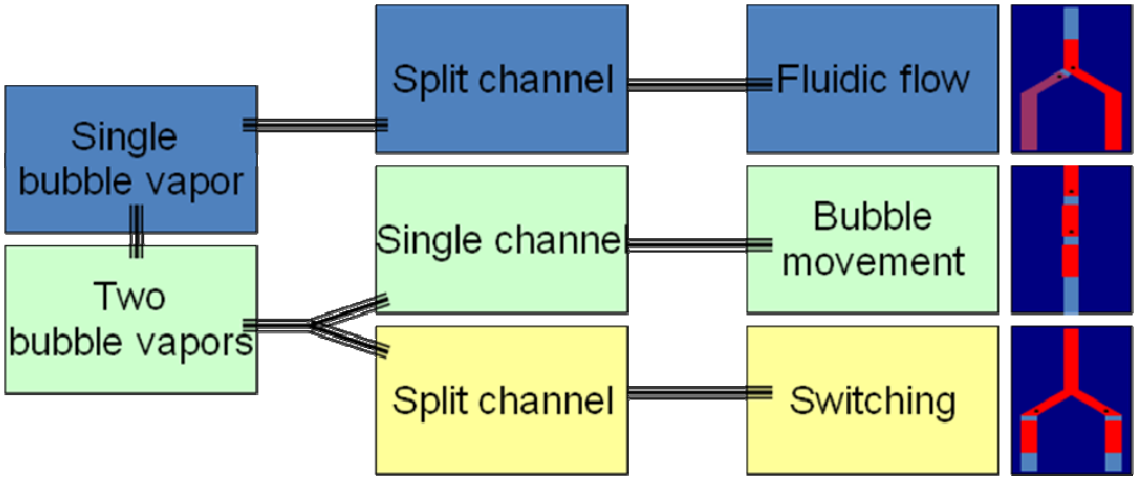

Figure 39. Increasing complexities taking advantages of the unique properties of the optofluidic pump. With a single bubble, in a split-channel (Y-channel) structure with two liquid reservoirs, the chip can achieve bidirectional fluidic flow and chemical concentration gradients. With two bubbles, several different functionalities can be shown. In a single-channel structure, bubble motion can be shown by adjusting laser power and liquid reservoir pressure. In a split-channel structure, fluidic switching of two liquids is possible.

2. Chip synthesis

We utilize block copolymer lithography to deposit a monolayer of gold nanoparticles [22]. The gold nanoparticles are generated utilizing the following compounds: toluene (Sigma-Aldrich), gold chloride hydrate (Sigma Aldrich), and polystyrene-b-2-vinyl pyridine (PolymerSource). In a dark, nitrogen-filled environment, 5 mL toluene is mixed with 25 mg polystyrene-b-2-vinyl pyridine for 24 hours. About 8 mg gold chloride hydrate was added to the solution and mixed for 3 days. This solution was spin coated onto a glass slide at 2000 rpm. Afterwards, the gold nanoparticle coated glass slide is placed in an oxygen plasma etcher for 10 minutes at 50 W. A scanning electron microscope image of the nanoparticles on a silicon wafer indicates that particles are about 15 nm in size with a separation between each nanoparticle of about 45 nm. The absorption peak of the gold nanoparticles occurs at about 500 nm, which is the approximate wavelength of the laser (514 nm).

The microfluidic channel is produced utilizing a replica molding process with polydimethylsiloxane (PDMS). The master mold of a single fluidic channel of 30 microns in width and 10 microns in height is produced utilizing UV lithography with 10-micron-thick SU-8 (GM-1040, Gerstelec) on a silicon wafer. After trimethylchlorosilane (Sigma Aldrich) treatment of the mold for 5 minutes, the PDMS (Dow Corning Sylgard 184) is poured onto the mold with a 10:1 base-to-curing-agent ratio. After curing in an oven at 80ºC for 1 hour, the silicone is released from the mold. Inlet and outlet ports are punched with a hole-punching machine and the silicone is given the oxygen plasma

treatment for 20 seconds at 50 W. Immediately afterwards, the silicone is bonded to the glass slide. The dimensions of the finished device are approximately 3 cm by 2 cm.

Under a microscope setup with 10x or 40x objectives, we focus a 514 nm Argon laser to about 10 microns in diameter. The laser energy is transferred into heat in this small region near the laser spot. The heat transferred to the liquid causes increased evaporation. The vapor re-condenses away from the laser spot, initially forming a vapor bubble and then pumping liquid from one side of the bubble to the other. A key feature of these optically controlled fluidic valves is that the initial liquid-vapor interface remains pinned.

3. Bacteria concentration

In this section, we look at the biocompatibility of these fluidic valves. Specifically, we demonstrate that optically controlled fluidic valves can be used to concentrate and detect bacteria. As demonstrated previously, only liquid is transported across the vapor bubble [7]. Therefore, bacteria and other compounds which do not experience a significant vapor pressure change with small thermal changes are not transported. They accumulate at the interface as shown in Figure 40. The 15 mW 514 nm laser beam is focused to a spot that is approximately 10 microns in size.

We probe these concentrated asymmetric bacteria by detecting the change in their scattering when they align to an electric field with a 5 mW 632 nm laser [23]. We notice that a single live asymmetric bacterium causes up to a 5% change in the scattered red laser signal when they are aligned to the electric field as opposed to when there is no field applied, due to a lack of alignment without a field. This allows for an improvement in the threshold of the detection capability of asymmetric bacteria, which is dependent on the amount of fluid that is pumped across the vapor bubble. As reported previously, the thermal gradient generated is less than 2 degrees Celsius [7] and the asymmetric bacteria remained alive within the fluidic channel throughout the several hours of the utilization of the optofluidic pump [24].

The potential capability of this concentrator is dependent on the amount of liquid that can be transferred through the vapor bubble. Previous studies showed that there is no noticeable change in the flow rate with respect to time [7]. Therefore, the concentration is dependent simply on time. Assuming some uniform concentration of bacteria at x

bacteria/mL and a flow rate of the vapor bubble at y mL/sec, we will be able to concentrate x•y bacteria/sec at the vapor bubble interface. Figure 41 shows the time elapsed to concentrate bacteria solution that was at an initial concentration of 10^7 bacteria/mL. Every minute, we concentrate 4–5 bacteria at the liquid-vapor interface. Saturation occurs when liquid reaches the output port of the microfluidic channel. For a 1-cm-long microfluidic channel, this occurs in about 30 minutes. We were able to concentrate about 100–150 bacteria at the interface during this time.

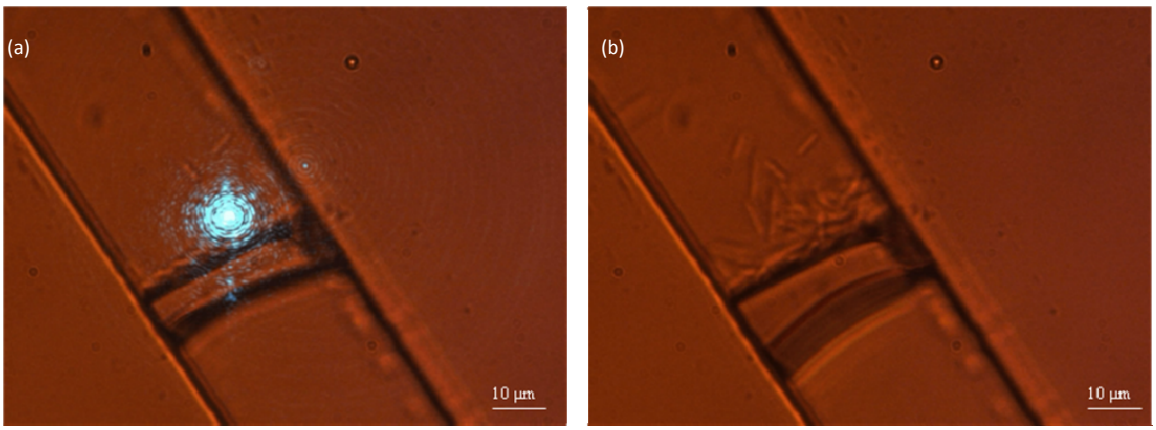

Figure 40. Bacteria concentration using the optofluidic pump. The input to the liquid with the bacteria is from the top left of the image. The bottom right of the image is connected to the output. (a) The vapor bubble is located in between, with the laser spot on the input side interface. (b) After several minutes, the bacteria is concentrated on one side of the vapor bubble interface. At this concentration of bacteria (~ 10^7 bacteria/mL), there are about 3 bacteria after about 1 minute of concentration, during which the water moves about 100 microns (the channel is 30 microns wide by 10 microns tall).

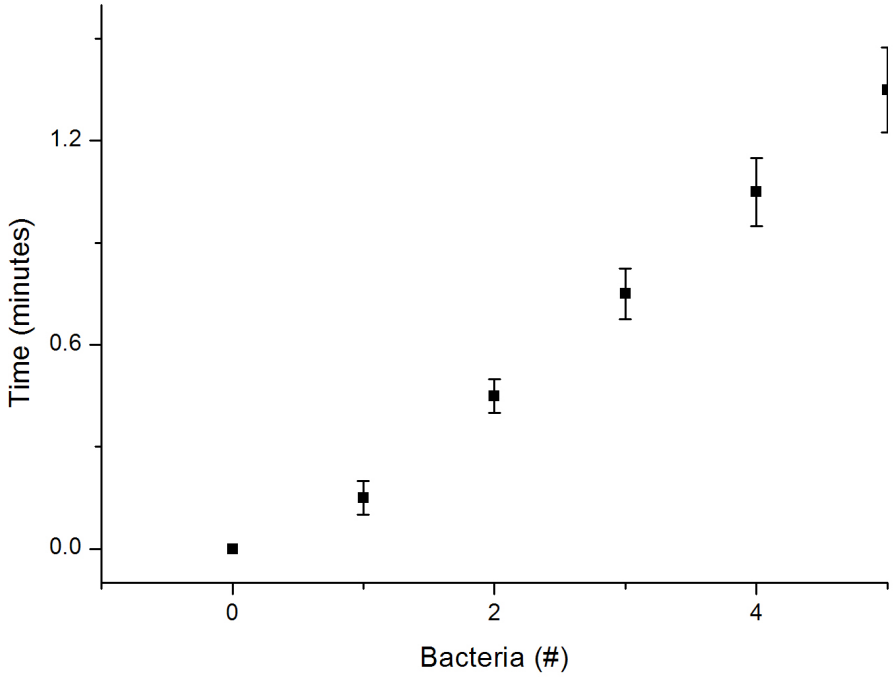

Figure 41. Arrival of bacteria with respect to time. The device starts with zero bacteria at the interface. Over an average of 10 pumps where the bacteria are uniformly distributed, the time required to trap each additional bacteria is measured. The fifth bacteria came in at approximately 1.2−1.5 minutes for 10^7 bacteria/mL concentrated solution. In the solution, notice that the bacteria slightly repel each other, which explains their uniform distribution within the solution [25].

4. Two bubbles in a single fluidic channel

Increasing complexity with vapor bubbles in a single fluidic channel naturally leads to increasing the number of vapor bubbles to manipulate droplets of liquids in a two-phase system surrounded by air. In this section, we explore the motion of the fluidic valves and droplets. In Figure 42, the general schematic with two vapor bubbles in a single fluidic channel is shown. The flow rate of each vapor bubble is controlled by the laser intensity and the distance from the laser spot to the liquid-air interface.

Since the size of the vapor bubble may not be changed, all the different possibilities of vapor bubble and droplet motion can be simplified into three specific actions. First, the first vapor bubble may be moved towards to the inlet. Second, the first vapor bubble may be moved towards the outlet, decreasing the droplet size. Third, the second vapor bubble may be moved towards the outlet, increasing the droplet size. Any other combination of vapor bubble motion with droplet size change may be achieved with the combination of the above mentioned actions. These scenarios are described in Figure 43.

Of note in the normal optofluidic pump is that the input reservoir is left at a state in which there is a slight amount of pressure. Even with the pressure, the water-air interface remains stable due to the hydrophobicity within the channel. When the laser spot is kept stable, the capillary pressure replaces the liquid that is transferred across the vapor bubble. However, for vapor bubble motion, the laser spot must be moved continuously with respect to the water-air interface. In the scenario where the vapor bubble is moved towards the inlet, the flow rate across the interface must be increased

such that it is higher than the capillary water replacement rate. This means that the input laser power is increased, the distance between the laser spot and water-air interface is decreased, or the input reservoir pressure is decreased.

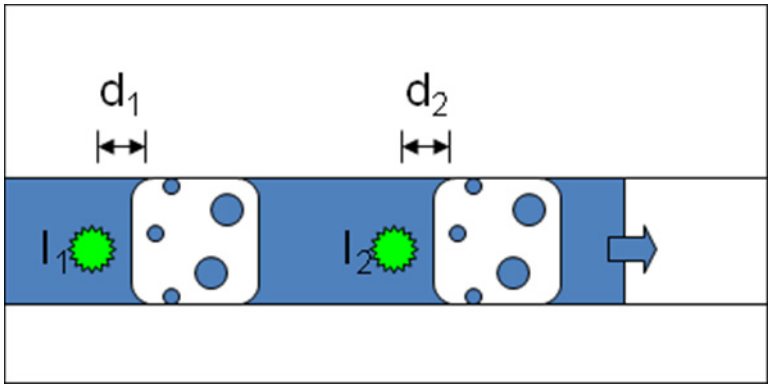

Figure 42. General configuration with two vapor bubbles in a single fluidic channel. There are two laser spots of two possibly different intensities, I1 and I2, each at distance d1 and d2 from the interface, respectively. When I1=I2 and d1=d2, there is no motion in the vapor bubble and there is mass transfer with the rightmost liquid-air interface moving to the right. The total flow rate is controlled by I and d such that there are more conditions in which the vapor bubble doesn't move when I1≠I2 and d1≠d2. The amount of motion in each interface is measured where we assume d1=d2 in the following cases.

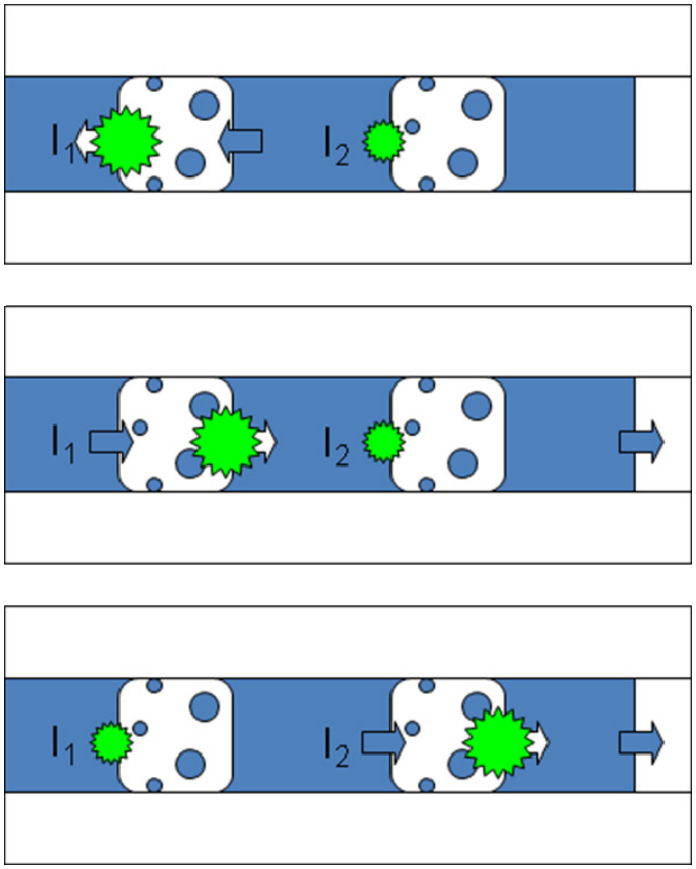

Figure 43. The three different possibilities of motion. If I1>I2, there is a distinct motion to the left of the leftmost interface. For continuous motion of the first vapor bubble, the laser spot at I1 must be moved to maintain d1. Similarly, when the location of I1 is moved to the other interface (second leftmost), the left vapor bubble moves to the right. Once again, for continuous motion, the laser spot I1 must be moved to maintain d1. In the last case, when I2>I1, there are two possibilities. If the laser spot is on the left hand side interface of the right vapor bubble, there is no difference from the above case (flow rate is limited by the rate on the left vapor bubble). If the laser spot is on the right hand side interface of the right vapor bubble, we can move the right vapor bubble. Continuous motion requires motion of the laser spot.

5. Fluidic switch

Next, we investigate fluidic switching using optically controlled vapor bubbles. In an extension to the previous work [7], we demonstrate the relative ease of parallelization of fluidic valves using multiple focused laser spots. We introduce a vapor bubble into both branches of the Y junction fluidic channel (Figure 44). The fluidic valves are stationary due to the pinning of the liquid air interface. The inlet channel junction is approximately 100 microns below the visible field of the microscope. Liquid is provided at the inlet via a syringe, while the two output ports are open and unconnected.

The flow rate across the vapor bubble is influenced by both the power and position of the focused laser beam. We use a spatial light modulator (SLM) to independently control these parameters for each fluidic valve. It is possible to maintain a vapor bubble without any movement in any of the liquid-vapor interfaces by decreasing either the intensity of the beam or moving the position of the laser beam. There is also a maximum pumping rate, as too much laser power intensity close to the liquid-vapor interface causes unstable vapor bubble formation. The maximum pumping rate is dependent on the size of the fluidic channel. For 30-micron-wide by 10-micron-tall channels, this occurs at a pumping rate of approximately 9 picoliters per second (30 microns per second). By utilizing the difference in pumping rates in the two fluidic valves, we can selectively switch the liquid into either channel.

Figure 45 shows a graph of flow rate for each vapor bubble with respect to the percentage of power in each vapor bubble. We assume that the total input laser power is placed to either vapor bubble. Note the nonlinear nature of the pumping rate since the

total flow rate when the power is split into two is less than when one vapor bubble is pumped. This relationship is also shown in previous work and is due to the nonlinear relationship of the differential vapor pressure at different thermal gradients [7].

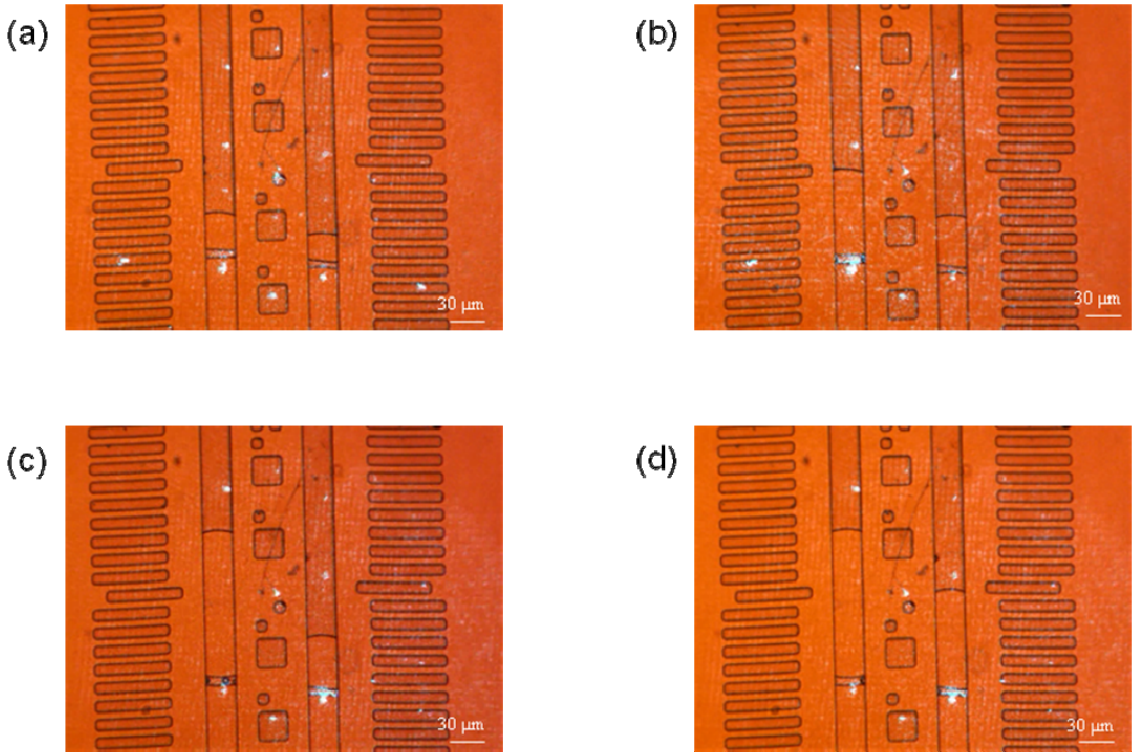

Figure 44. Images of fluidic switching. There are two fluidic channels surrounded by 3 sets of markers, symmetric about the middle. The two channels are connected below the image in a Y-junction, leading to a single input fluidic channel, connected to a reservoir of liquid. The two vapor bubbles already exist and the laser spots are on the lower side of the vapor bubbles. (a) Initial image showing the two initial vapor bubbles. (b) The laser power on the left-side vapor bubble is increased. (c) There is mass transfer of the liquid on the left-side vapor bubble while the right side remains stable. The laser power is now decreased on the left side and increased on the right side. (d) There is mass transfer of liquid on the right-side vapor bubble while the left side remains stable.

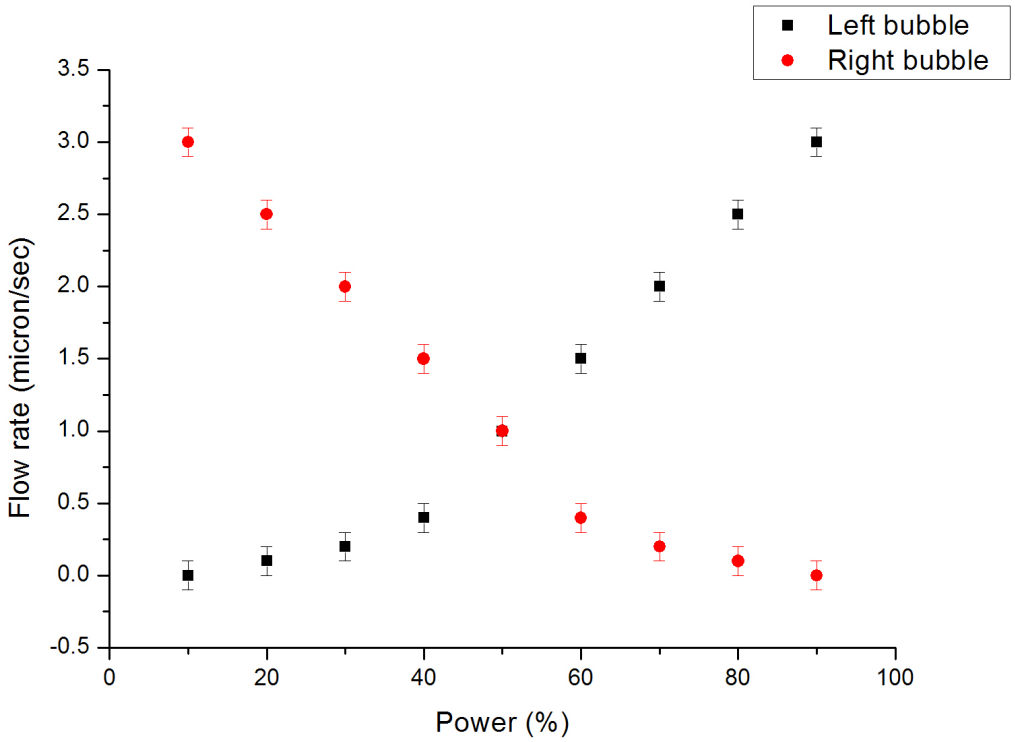

Figure 45. Power in each vapor bubble versus flow rate. Using the spatial light modulator, we can control the power in each vapor bubble. We measured the flow rate with respect to the power in each vapor bubble. Note that the curve is not quite linear. This is due to the vapor pressure curve with respect to temperature not being quite linear, as well as to some nonlinearity in the system.

C. Bidirectional flow using plasmonic optofluidic valves

1. Chip design

The schematic diagram of our experimental setup is shown in Figure 46. The microfluidic chip is a Y-junction where two channels combine into a single channel. A SLM is used to illuminate specific areas of the chip in order to create optothermal valves. As before, the thermal energy transfer from the laser to the liquid is enhanced by depositing a monolayer of gold nanoparticles at the floor of the fluidic channel. The plasmon resonance of the particles matches the laser wavelength.

In this section, we create a single fluidic valve where both interfaces of the valve are connected to independent liquid reservoirs. In Figure 46, there are two parallel, vertically orientated microfluidic channels connecting to a single channel in a Y-junction. The two independent liquid reservoirs are connected by a syringe through inlet ports not shown in the bottom of the image. The upper microfluidic channel acts as a release valve for the pressure as the liquid is filled into the two microfluidic channels from the bottom. The two liquid-vapor interfaces remain pinned and stable without a laser beam.

When a laser beam is focused on one of the liquid-vapor interfaces, water is vaporized across the interface and pumped to the other interface. This pumping rate can be modified by changing either the position of the laser beam from the interface or the intensity of the laser beam. This fluidic pump effect occurs when the laser beam is placed on either interface, allowing us to flow fluid in either direction simply by changing the

position of the laser beam. We utilize a spatial light modulator (SLM) in the input laser beam before the microscope to manipulate the intensity and position of the beams.

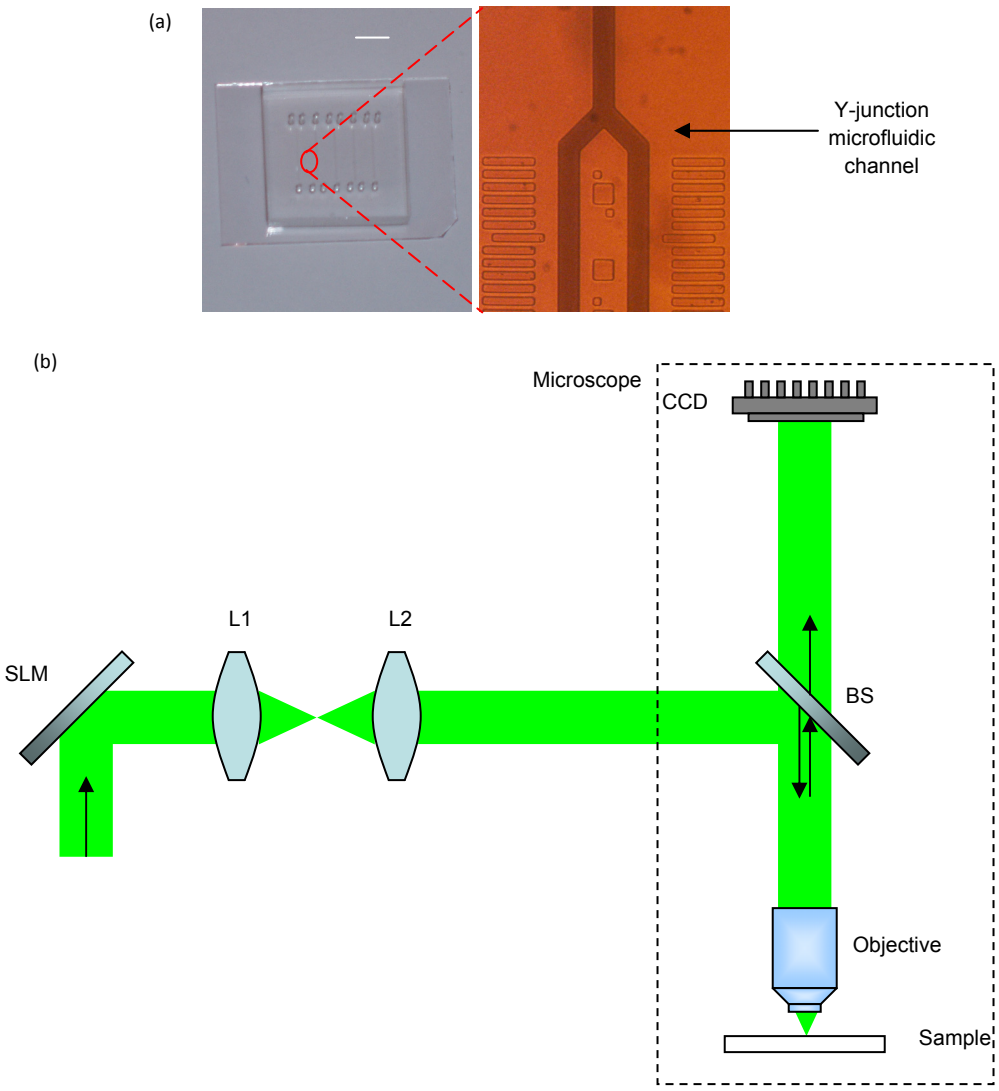

Figure 46. Picture and diagram of the device with schematic of optical setup. (a) There are five parallel Y-junction channel devices with one input port and two output ports. The glass slide has a monolayer coating of gold nanoparticles which resonate at about 500 nm. Close-up image is taken with a 4x magnification objective lens. (b) The SLM is tilted at 45 degrees with the focal lengths of L1 and L2 chosen to match the beam width to the objective exit pupil.

2. Chemical concentration gradient

Bidirectional fluidic flow is visually demonstrated by using two separate liquid-filled syringes in Figure 47; the channel on the left is filled with pH 7 deionized water and the channel on the right is filled with 10% ammonium hydroxide solution and approximately 1 mg/mL thymol blue pH indicator dye. Thymol blue pH indicator is dark blue when the pH of the solution is above 9.6 and becomes nearly transparent with a slight yellow tint when the pH of the solution falls below 8. Initially, the channel filled with the pH indicator is slightly opaque. When the fluidic valve is utilized to pump water from the right to the left, the channel on the right becomes darker due to the increasing pH, as shown in Figure 47(a). When the position of the laser beam is changed such that the fluidic valve is utilized to pump water from the left to the right, the channel on the right becomes lighter due to the decreasing pH, as shown in Figure 47(b) and (c).

Extending the concentration capabilities to perform dilution can serve useful in many biological or chemical studies. Active chemical concentration gradients can be generated with the complexity of these gradients limited by the number of liquid-vapor interfaces. The profile of the chemical gradient that can be generated is dependent on the speed of the fluidic valve and the diffusion coefficient of the chemical. In cases where the characteristic diffusion length of the chemical is much longer than the system size ($L_d = \sqrt{4Dt} >> L$, where D is the diffusion coefficient, t is the time, and L is the length of liquid transported across the fluidic valve), the concentration profile is essentially linear. This is the case for most ionic compounds in the liquid when D ~ 10^{-9} m^2/s, as is true for the example shown in Figure 47. On the other hand, this is no longer true for many

biological compounds where D ~ 10^{-11} m^2/s and the length scales with the amount of fluidic transport. In this case, we are capable of generating very large gradients with the concentration being highly time-dependent, and changing the laser intensity will allow us to rapidly change the chemical concentration nearby. We envision the possibility of using bidirectional fluidic flow with a single fluidic valve for chemotaxial studies of biological and chemical compounds, as well as for replacing simple microfluidic functionalities.

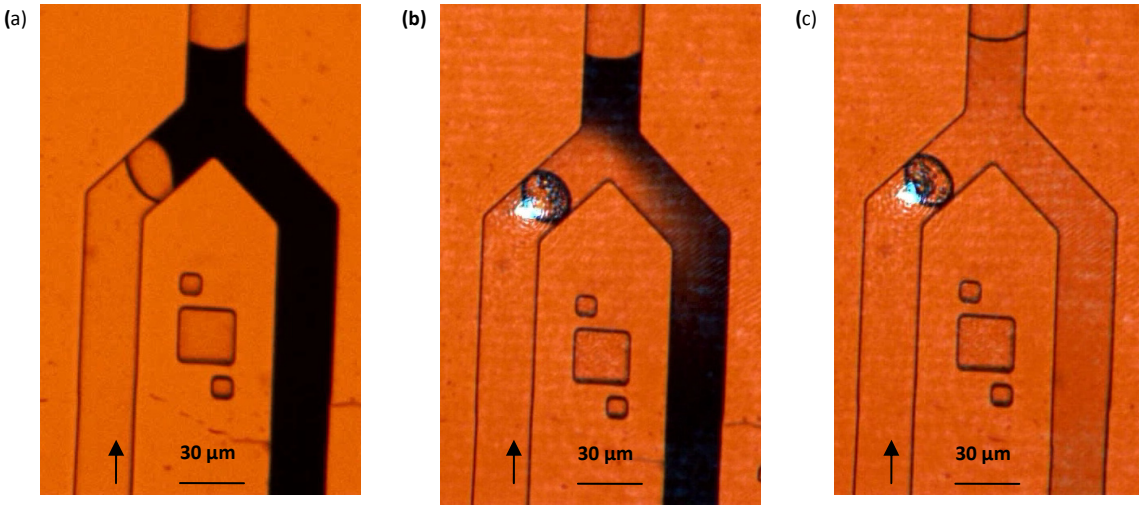

Figure 47. Demonstration of bidirectional fluidic flow. (a) shows the concentration of base in the right-hand liquid column due the transport of water to the left-hand side. (b) shows the partial dilution of the base as the transport of water is conducted in the opposite direction after 5 seconds. (c) shows the complete dilution of the base after 10 seconds. pH indicator is used to visualize the pH change (dark at pH > 9.6 and clear at pH < 8).

3. Latex bead particle motion control

A natural extension for bidirectional fluidic control is to manipulate a sample of interest to move it over a specific region within the chip where the sensing occurs [1, 26]. The sensing can be improved by passing the same object over this sensor. Controlling the speed of the particle motion is important as well. We demonstrate this capability with our fluidic valves using 1 micron latex bead particles.

In Figure 48, both channels are filled with water with 0.1% by weight of 1 micron latex bead particle. Particle solutions can be both concentrated and diluted at the same time. Individual motion of the particles during fluidic pumping can be tracked as well. The bidirectional motion control is demonstrated in Figure 48(a) and (b). The overall motion of the particles with respect to laser power is shown in Figure 49. Particle velocity from about 1 microns/second to 10 microns/second can be controlled by changing laser power with errors of around 10%. This speed is dependent on the position of the particle within the channel. Due to the no-slip condition within microfluidic channels, particles within the middle of the channel move at higher speeds than near the walls of the channel.

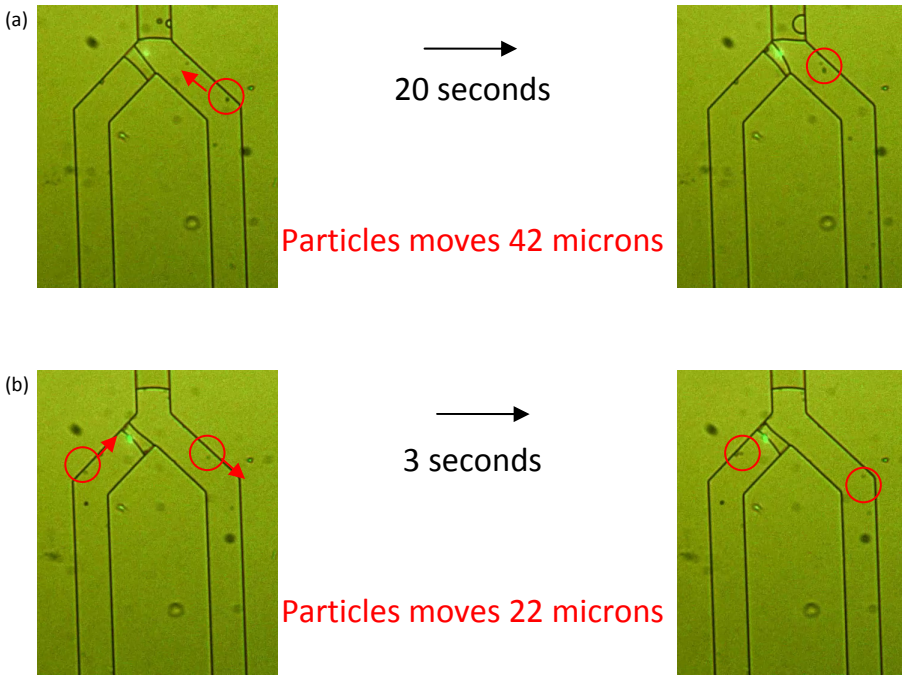

Figure 48. Demonstration of latex bead particle motion control. (a) shows the motion of 1 micron latex beads from the reservoir on the right-hand side to the liquid-vapor interface by transporting the water in the right-hand-side solution to the left-hand-side solution. (b) shows the motion of the particles from the liquid-vapor interface to the reservoir on the right-hand side by transporting the water in the left-hand-side solution to the right-hand-side solution.

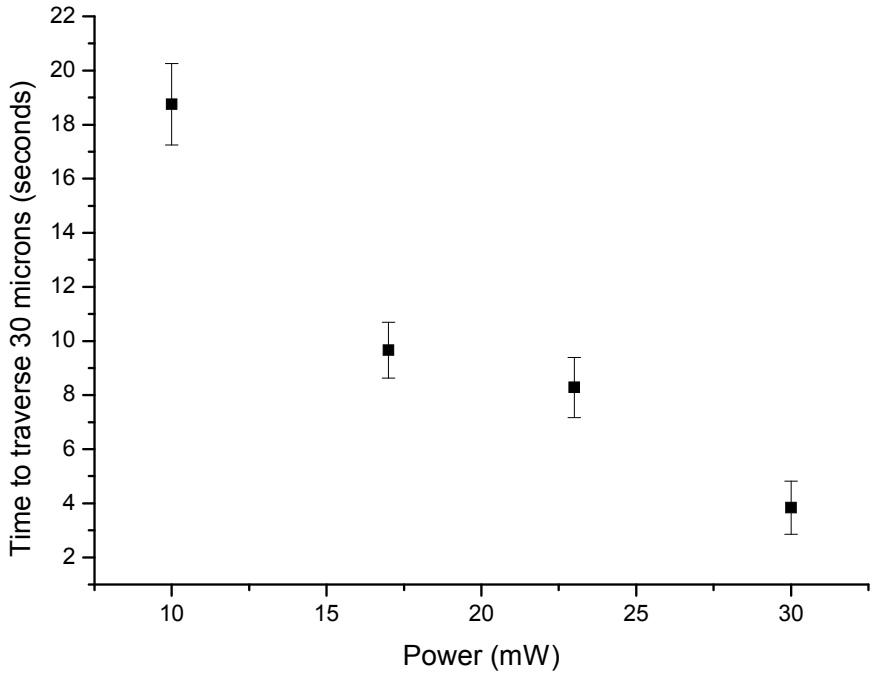

Figure 49. Curve showing particle motion control by changing laser power. The particle velocity is highly dependent on the location of the particle within the channel due to no-slip conditions of the fluid within the microfluidic channel.

4. Bacteria motion control

Next, we attempt to control *E. coli* K12 bacteria with the bidirectional fluidic valve. A key component of this demonstration was to show that the temperatures utilized to operate the bidirectional fluidic valve would not kill the bacteria. Previously, it was demonstrated that the valve operates with less than a 4 C change in temperature, which should not affect the bacteria's viability at room temperature [27]. The bacteria were labeled with red fluorescence and suspended in deionized water. The solution of *E. coli* K12 bacteria was loaded into the left-hand-side channel and deionized water in the right-hand-side channel. We apply the fluidic valve to either side of the channel at different rates to determine the amount of motion that the bacteria experience on the left-hand-side channel. Figure 50 and Figure **51** show the motion of bacteria with the application of the bidirectional fluidic valve. There is good correlation of the average motion of a group of bacteria when compared to the amount of fluid that has been transferred by the fluidic valve. We note that there is some side-to-side motion from the bacteria. The bacteria remain viable throughout the entire experiment, which can be confirmed visually due to their motion as well as their reproductive capabilities.

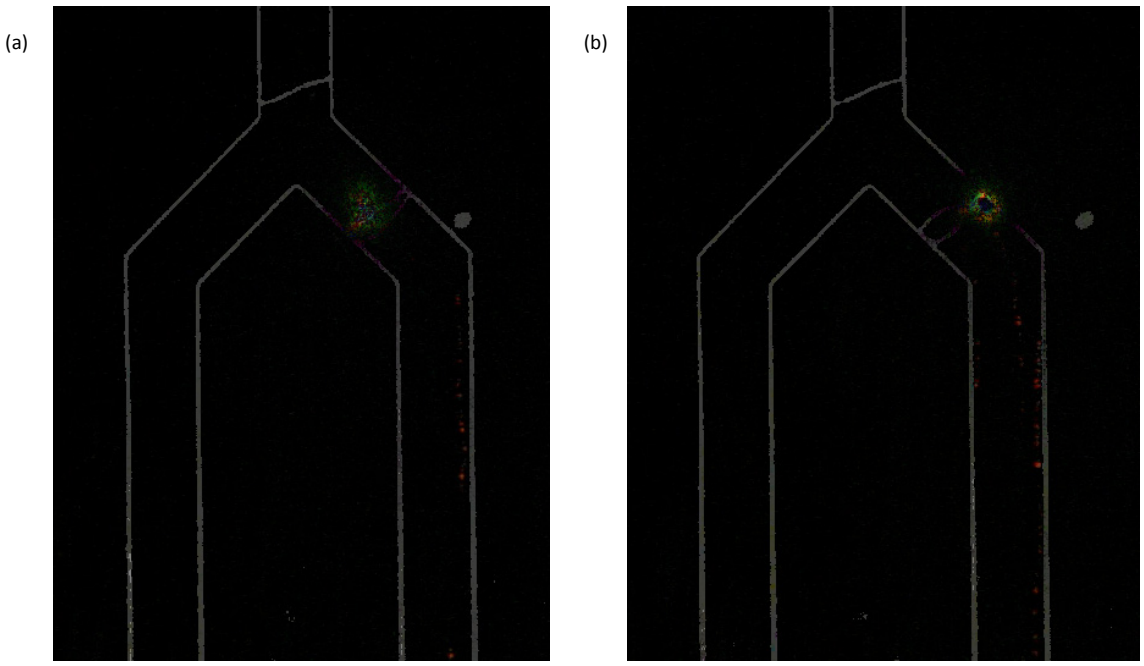

Figure 50. Demonstration of bacteria motion control. (a) shows the motion of the bacteria from the reservoir on the right-hand side to the liquid-vapor interface by transporting the water in the right-hand-side solution to the left-hand-side solution. (b) shows the motion of the bacteria from the liquid-vapor interface to the reservoir on the right-hand side by transporting the water in the left-hand-side solution to the right-hand-side solution.

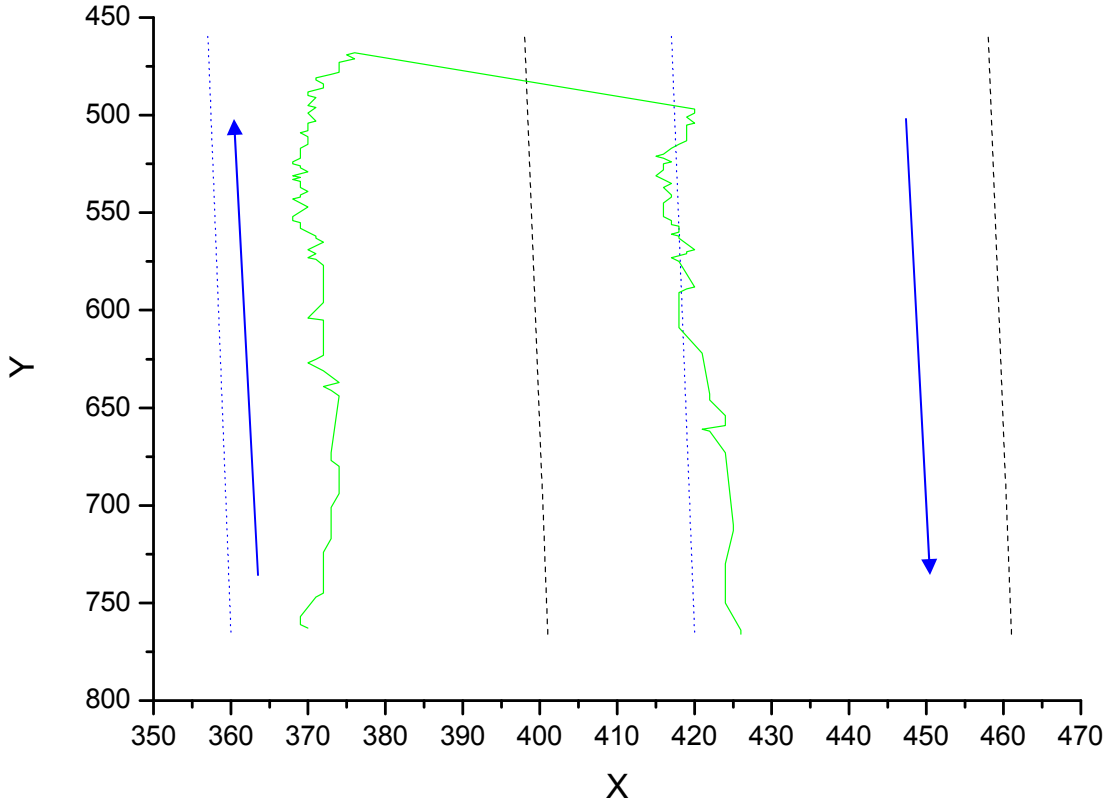

Figure 51. Demonstration of bacteria motion control. This curve shows the motion of a single bacterium as it is first moved towards the valve then moved away from the valve. The valve is located at Y~400. The bacterium starts away from the valve, at Y~770, and approaches the valve. When the bacterium reaches Y~470, the chip is moved with the laser beam focused on the other interface. The bacterium flows away from the valve. The dashed lines indicate the two pairs of channel walls (dotted when the bacterium is moving towards the valve, at X~360 and X~420, and dashed when the bacterium is moving away from the valve, at X~400 and X~460).

D. References

1. Psaltis D, Quake SR, Yang CH. Developing optofluidic technology through the fusion of microfluidic and optics. Nature 442, 381–386 (2006).
2. Whitesides GM. The origins and the future of microfluidics. Nature 442, 368–373 (2006).
3. Unger MA, Chou HP, Thorsen T, Scherer A, Quake SR. Monolithic microfabricated valves and pumps by multilayer soft lithography. Science 288, 113–116 (2000).
4. Thorsen T, Maerkl SJ, Quake SR, Microfluidic large scale integration. Science 298, 580–584 (2002).
5. Liu GL, Kim J, Lu Y, Lee LP. Optofluidic control using photothermal nanoparticles. Nat. Mat. 5, 27–32 (2006).
6. Stone HA, Stroock AD, Ajdari A. Engineering flows in small devices: microfluidics toward a lab-on-a-chip. Annu. Rev. Fluid Mech. 36, 381–411 (2004).
7. Boyd DA, Adleman JR, Goodwin DG, Psaltis D. Chemical separations by bubble-assisted interphase mass-transfer. Anal. Chem. 80, 2452–2456 (2008).
8. Krishnan M, Park J, Erickson D. Opto-thermorheological flow manipulation. Optics Letters 34, 1976–1978 (2009).
9. Sershen SR, Mensing GA, Ng M, Halas NJ, Beebe DJ, West JL. Independent optical control of microfluidic valves formed from optomechanically responsive nanocomposite hydrogels. Adv. Materials 17, 1366 (2005).
10. Erickson D, Li D. Integrated microfluidic devices. Anal. Chim. 507, 11–26 (2004).
11. Blakely JT, Gordon R, Sinton D. Flow-dependent optofluidic particle trapping and circulation. Lab on a Chip 8, 1350–1356 (2008).
12. Yamahata C, Chastellain M, Parashar VK, Petri A, Hofmann H, Gijs MAM. Plastic micropump with ferrofluidic actuation. J. MEMS 14, 96–102 (2005).
13. Darhuber AA, Valentino JP, Troian SM, Wagner S. Thermocapillary actuation of droplets on chemically patterned surfaces by programmable microheater arrays. J. MEMS 12, 873–879 (2003).
14. Thamdrup LH, Larsen NB, Kristensen A. Light-induced local heating for thermophoretic manipulation of DNA in polymer micro- and nanochannels. Nano Letters 10, 826–832 (2010).
15. Choi JW, Rosset S, Niklaus M, Adleman JR, Shea H, Psaltis D. 3-dimensional electrode patterning within a microfluidic channel using a metal ion implantation. Lab on a Chip 10, 783–786 (2010).
16. Kuhn S, Lunt EJ, Philips BS, Hawkins AR, Schmidt H. Ultralow power trapping and fluorescence detection of single particles on an optofluidic chip. Lab on a Chip 10, 189 (2010).

17. Choi W, Nam SW, Hwang H, Park S, Park JK. Programmable manipulation of motile cells in optoelectronic tweezers using a grayscale image. Applied Physics Letters 93, 143901 (2008).

18. Li D. Electrokinetics in microfluidics (Academic Press, 2004).

19. http://www.nanopartz.com.

20. Hartman RL, Sahoo HR, Yen BC, Jensen KF, Distillation in microchemical systems using capillary forces and segmented flow. Lab on a chip 9, 1843–1849 (2009).

21. Zhang YP, Kato S, Anazawa T. Vacuum membrane distillation by microchip with temperature gradient. Lab on a chip 10, 899–908 (2010).

22. Jaramillo TF, Baeck SH, Cuenya BR, McFarland EW. Catalytic activity of supported Au nanoparticles deposited from block copolymer micelles. J. Am. Chem. Soc. 125, 7148–7149 (2003).

23. Choi JW, Pu A, Psaltis D. Optical detection of asymmetric bacteria utilizing electro orientation. Optics Express 14, 9780–9785 (2006).

24. Choi JW, Adleman JR, Psaltis D. Bacteria manipulation with optically controlled fluidic valves. CLEO 2009.

25. Berg HC. Bacterial behavior. Nature 254, 389–392 (1975).

26. Pang S, Cui X, DeModena J, Wang YM, Sternberg P, Yang C. Implementation of a color-capable optofluidic microscope on a RGB CMOS color sensor chip substrate. Lab on a chip 10, 411–414 (2010).

27. Mille Y, Beney L, Gervais P. Viability of Escherichia coli after combined osmotic and thermal treatment: a plasma membrane implication. Biochimica et Biophysica Acta — Biomembranes 1567, 41–48 (2002).

V. Nanowire light sources

A. Introduction

In the previous chapters, fluorescent labeling of the bacterium enabled clearer visualization of single bacterium with an optical system. This specific labeling of biological and chemical compounds has resulted in the capability of studying the properties and interactions of these compounds with greater complexity. Fluorescent imaging deals with the field of labeling the component of interest with fluorophores such as fluorescent molecules [1], fluorescent proteins [2], or quantum dots [3]. Many interesting problems have been tackled by these imaging probes, however, there is a certain subset of questions which cannot be resolved using these techniques due to the limitations in these fluorescent markers. These disadvantages include photobleaching, blinking, and the lack of coherence [4]. To complement these fluorescent markers, second harmonic radiating imaging probes (SHRIMPs) have been developed [4]. In this chapter, we demonstrate the ability to manipulate these types of probes with electric fields and its applicability to help in long term studies with bacteria.

1. Second harmonic radiating imaging probes (SHRIMP)

Second harmonic radiation is a process that occurs due to two distinctly different processes. First, when the material has a noncentrosymmetric structure, there is bulk second harmonic generation. Second, when there are asymmetries in interfaces, there is surface second harmonic generation. [5] For large particle sizes, the bulk component dominates the surface component, as volume scales with the third power of radius, whereas the surface area scales with the second power of radius. The bulk component is described in the equation below:

$$P_{eff}(2\omega) = d \cdot E(\omega) \cdot E(\omega).$$

There are two interesting components with regard to the second harmonic signal generated. It is dependent on both the polarization of the incoming electric field and the orientation of the crystal. For nanoparticles and nanowires below the scattering limit, the specific orientation of the particle can be determined by looking at the second harmonic signal without visualization of the particle [6]. Some experiments with the application of electric fields as well as some applications with regards to bacteria behavior will be proposed.

2. Dielectrophoresis and electro-orientation

Applied electric fields can move colloids within liquids. There are two different forces that can be used to manipulate colloids. First, in non-uniform electric fields, particles move such that the total energy in the system is maximized. This manipulation occurs due to the difference in the dielectric permittivity between the medium and the particle. When the particles' dielectric permittivity is lower than the medium, the particles move away from the locations with the highest electric fields. On the other hand, when the particles' dielectric permittivity is higher than the medium, the particles move towards the locations with the highest electric fields. This effect is termed dielectrophoresis [7]. Next, in uniform electric fields, asymmetric particles may be manipulated. Similar to before, when the particles' dielectric permittivity is lower than the medium, the particle will be aligned perpendicular to the electric field. On the other hand, when the particles' dielectric permittivity is higher than the medium, the particle will align parallel to the electric field. This effect is termed electro-orientation [8].

B. Dielectric manipulation with optical sources

1. Introduction

Lithium and potassium niobate are some of the most versatile optical and electronic materials, being simultaneously nonlinear-optic, electro-optic, acousto-optic, ferroelectric, piezoelectric, and photorefractive. Use of lithium and potassium niobate have been constantly growing in engineering applications. They have been used in the telecom industry for frequency conversion and electro-optic modulation [9, 10]. In the past decade, significant interest has been focused on the synthesis of nanoscale materials due to their interesting properties emerging from the dimensional confinement, which has great potential application in devices.

Many synthesis routes are being developed for both lithium and potassium niobate crystals at the nanoscale, resulting in different sizes, shapes and crystalline qualities. These nanoparticles have been previously produced by milling [11], nonaqueous route [12], sol-gel method [13], or hydrothermal route [14, 15]. An array of polycrystalline nanotubes have also been reported [16], as well as a solution-phase synthesis that produces rod-like structures among other multiple structures [17]. We study the second harmonic generation (SHG) properties of these nanowires and show that nanowires are an efficient nanoscale second harmonic light source. The SHG study also reveals the orientation of the crystal structure, paving the way for future applications of the unique crystal properties of these nanowires. As one particular example, we demonstrate the manipulation of the nonlinear optical response of a single nanowire using external electric fields in microfluidic channels, while simultaneously monitoring its

SHG signal. Indeed, these nanowires can be used as imaging probes [18], as nanoscale electro-optical devices like localized photon sources, or as components of nanomachines.

2. Measuring SHG signal

To perform correlated scanning electron microscope (SEM) and SHG studies, we locate a single potassium niobate wire of 50 nm diameter and 700 nm long. The same nanowire is then located again for SHG investigation under a white-light transmission microscope using prescribed markers on the ITO glass slide. The laser source is a Ti:sapphire oscillator operated at 800 nm wavelength, with 150 fs pulse and 76 MHz repetition rate, focused down to 20 μm diameter on the sample at an average power of 160 mW. The SHG signal at 400 nm is then collected with an oil immersion microscope objective (100x, NA 1.4) and recorded on an electron multiplying charge coupled device (EMCCD) after filtering out the fundamental pump wavelength. The polarization of the pump beam is rotated with a half-wave plate to obtain polarization-dependent SHG response. Figure 52 shows the polarization-dependent response of the SHG emission for the single nanowire. At different incident polarization angles, the SHG intensities are recorded.

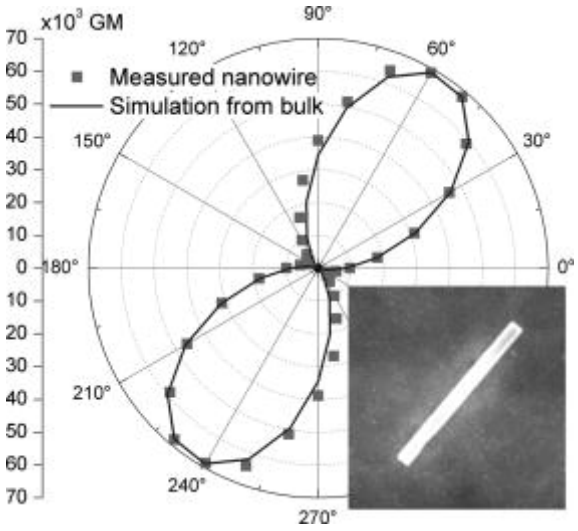

Figure 52. Polarization response of SHG from a single potassium niobate nanowire with corresponding SEM image. Nanowire is 50 nm wide and 700 nm long. Note how the maximum second harmonic generation is measured along the axis of the nanowire. Therefore, by determining the maximum output signal, the user can determine the orientation of the wire for objects below the diffraction limit.

3. Electro-orientation of nanowires

As a potential application of the unique SHG property of these nanowires, we demonstrate the electrical manipulation of the SHG signal in a fluidic setup. We manipulate the orientation of an optically trapped nanowire in a fluidic environment using an externally applied electric field and monitor its SHG response. As shown in Figure 53, the optical tweezer is constructed using a femtosecond Ti:sapphire laser operated at 800 nm wavelength. The nanowire under investigation is suspended in a aqueous fluid supported on a glass substrate that is patterned with ITO electrodes [19]. The focus of the tweezer beam is located between the two electrodes and slightly outside the fluid region so that the nanowire is pressed on the substrate and is oriented orthogonally to the beam propagation. Figure 54 shows white light images (a, c) and SHG signals (b, d) of the nanowire suspended in deionized water. When no external electric field (E=0 V_{pp}) is applied (Figure 54 (a, b)), the nanowire is oriented along the electrode within the plane of the substrate following the polarization of the tweezer beam only. When an external electric field (E=10 V_{pp}) is applied to the nanowire using the electrodes (Figure 54 (c, d)), an additional electro-orientation force results due to the dielectrophoretic (DEP) response of the nanowire. The torque on the nanowire due to the external electric field (10^6 V/m) is more than ten times greater in magnitude than the torque on the nanowire due to the optical polarization of the laser for 3 mW power and 10 micron beam radius at the sample position (10^5 V/m). Under this 10 V_{pp} electric field with a frequency of 150 kHz in a fluid of 170 μS/cm conductivity, the nanowire is aligned with the field due to positive DEP forces. Note that the orientation of the

nanowire in the external electric field is mostly influenced by its shape and not by the different permittivities of the crystal.

Due to the polarization dependency of the wire, the SH signal is strongly attenuated in Figure 54(d) compared to Figure 54(b), allowing for monitoring the position of the wire. Increasing the conductivity of the suspension as well as changing the frequency of the applied electric field can change the type of DEP force on the nanowire which will result in the nanowire not being aligned with the field [20]. We notice the crossover between negative and positive DEP when the conductivity of the solution is around 170 μS/cm.

DEP forces have already been used to orient and manipulate several different types of dielectric nanowires [21]. In our case, besides the external applied field for DEP, the use of the 800 nm laser brings two advantages: maintaining the nanowire in a certain position with the trapping property and generating the second-harmonic signal that helps locate the nanowire, especially when the particle is sub-wavelength in size and cannot be optically resolved. The combination of the applied external electric field and the polarization of the laser beam is useful for several applications. First, a rough estimate of the conductivity near the nanowire may be obtained; for example if there is a conductivity gradient in the sample [22]. Second, a capability to determine the hydrodynamic conditions is possible within a fluidic environment [23]. The SHG from these nanowires allows for high signal-to-noise response and interferometric detection for sub-wavelength size structures due to the coherence of the SHG process. Third, the electrical manipulation makes the integration of several of these nanowires possible in

order to create massively parallel devices [24]. Optical means would be used to probe individual nanowires and electrical means to manipulate several of the nanowires at once.

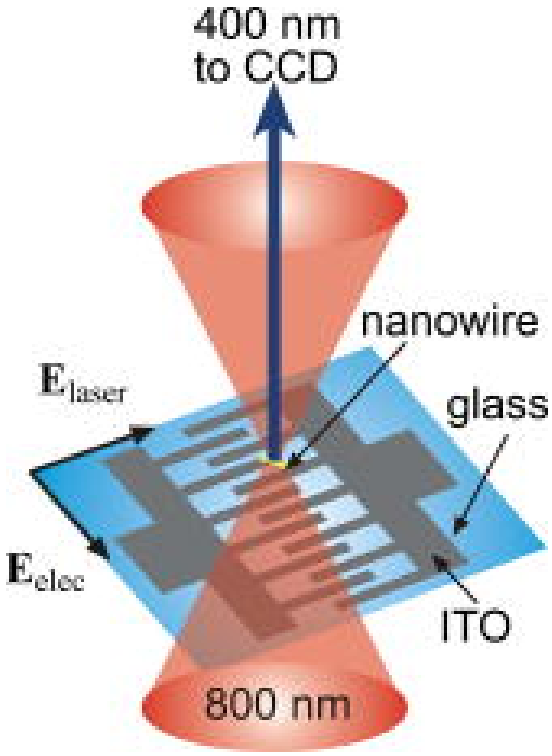

Figure 53. Schematic of the setup for the electrical and optical manipulation. Two torques attempt to orient the nanowire: the electric field due to the polarization of the 800 nm laser (E_{laser}) and the external applied electric field (E_{elec}).

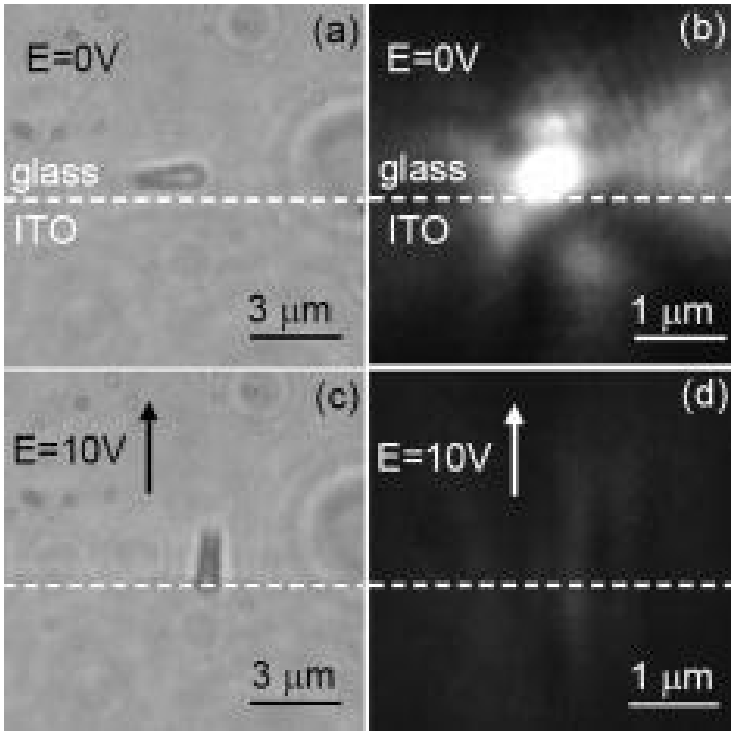

Figure 54. DEP response of a nanowire suspended in 170 uS/cm conductivity deionized water without (a, b) and with (c, d) an electric field of 10 V_{pp} at 150 kHz; (a, c) White light images, (b, d) SHG response

C. Long term bacteria behavior targeting

1. Introduction

A natural subset of biological experiments which are currently not possible with fluorophores is long term behavior targeting of biological cells and chemicals. These experiments are not possible due to photobleaching of fluorophores. Long term in vivo experiments with second-harmonic-generating nanoparticles have been demonstrated [25] and we propose the capability of using these markers for studying bacterial vitality.

2. Bacteria motility

Aging of single celled organisms which reproduce by symmetric division can be difficult to distinguish. There is a model for the trade off within a bacterium between reproduction and survival for aging organisms where it may sacrifice reproduction simply to increase its own survival [26]. However, when aging is defined simply by the lack of reproduction, it can be easier to conduct an experiment [27]. Another means of defining aging could be looking at the motility of the organism to different stimuli as it ages rather than simply looking at reproductive capabilities. With current fluorescent technologies, this may be fairly difficult due to the limited number of photons before particle bleaching. A method using the distinct advantages of second harmonic nanoprobes can serve this purpose.

First, the nanoprobe will be functionalized to attach to either the flagella or the cell membrane of the *Escherichia coli* (*E. coli*) [28], as shown in Figure 55. Then, the motility of the *E. coli* to the chemical source will be measured. The motility of the *E. coli* will be measured continuously to determine the standard deviation of the motion. There is an inherent difficulty in determining accurate z positioning as well as clockwise or counterclockwise rotation without lateral motion with normal fluorophores. However, due to the orientation detection properties of these nanoprobes, this will not be a problem. After a cycle of reproduction (approximately every 60 minutes at room temperature), the motility of the *E. coli* will be measured. Fresh food will be flushed in. Similar to [27], by looking at the originally labeled *E. coli* after several generations of reproduction, the motility of the *E. coli* can be measured and quantified.

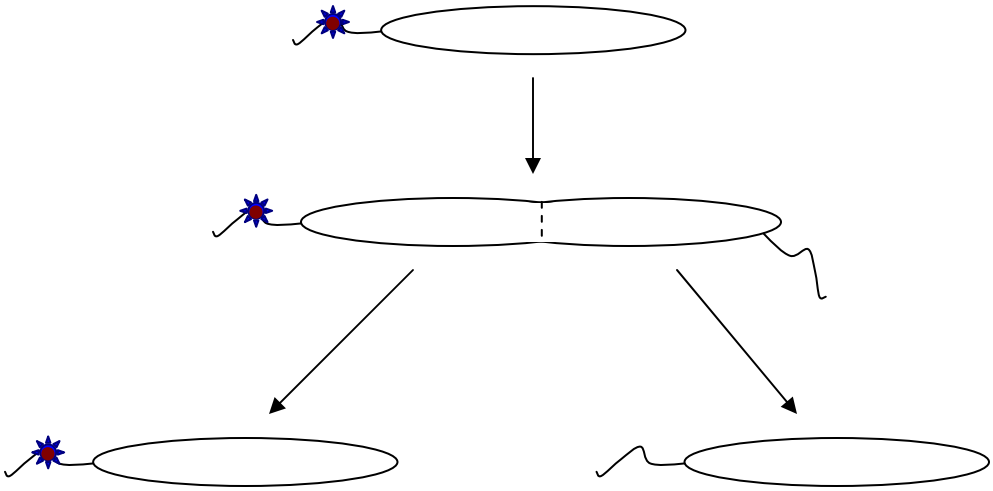

Figure 55. *E. coli* reproduction with nanoprobe. The nanoprobe is attached to either the flagellum or the cell membrane of the bacteria. As the *E. coli* reproduces, the older *E. coli* will be defined by the nanoprobe. Newer portions of the *E. coli* will not be labeled. Under the confocal microscope, only the older *E. coli* with the nanoprobe will be continuously monitored for its motion. As the *E. coli* ages, the change in the amount of clockwise and counterclockwise motion as well as the chemotaxial properties will be monitored.

3. Labeled bacteria

As a simple experiment of the toxicity of these nanoprobes with the *E. coli*, we perform a confocal imaging experiment of the fluorescently labeled bacteria with nanoprobes. In Figure 56, the bacterium is tracked for several minutes until the fluorescent label is bleached. However, the second harmonic generation from the nanoprobe remains at a consistent level. Also, there seems to be no effect with regards to motility due to the attached nanoprobe (which is approximately 200 nm in diameter) in comparison to other fluorescently labeled bacterium without a second harmonic generating nanoprobe.

4. Discussion

As the nanoprobe is functionalized to a specific flagellum, the age of the bacteria will be defined by the age of the flagellum. A control experiment would look at the bacteria motility as the bacteria concentration increases. Normally, the number of bacteria will increase as time increases and this interaction may lead to a change in motility. In this study, we wish to disprove a relationship between the concentration of bacteria with respect to the motility of a single bacterium which may occur due to the tradeoff between reproduction and survival [26].

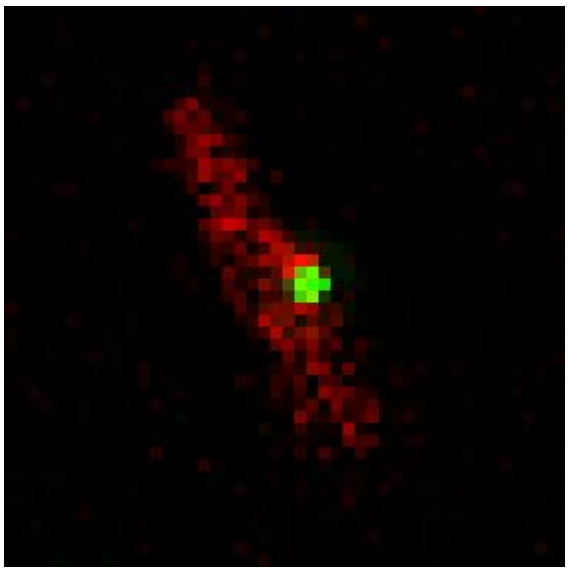

Figure 56. Labeled *E. coli* with nanoprobe. The *E. coli* cell membrane and flagella are fluorescently labeled in red. The nanoprobe is attached to the cell membrane of the *E. coli*, labeled in green. The sample is monitored under a two-photon confocal microscope setup with an excitation pump wavelength at approximately 900 nm. The second harmonic generated from the nanoprobe is at approximately 450 nm and the fluorescence is at approximately at 620 nm. After tracking the bacteria for approximately 5 minutes at 3 Hz, the fluorescent label is bleached. The second harmonic generated from the nanoprobe remains at the same intensity while the particle remains in focus and at the appropriate orientation to the detector.

D. References

1. Smith LM, Sanders JZ, Kaiser RJ, Hughes P, Dodd C, Connell CR, Hiener C, Kent SBH, Hood LE. Fluorescence detection in automated DNA sequence analysis. Nature 321, 674–679 (1986).
2. Chalfie M, Tu Y, Euskirchen G, Ward WW, Prasher DC. Green fluorescent protein as a marker for gene expression. Science 263, 802–805 (1994).
3. Chan WCW, Nie S. Quantum dot bioconjugates for ultrasensitive nonisotopic detection. Science 281, 2016–2018 (1998).
4. Hsieh CL, Grange R, Pu Y, Psaltis D. Three-dimensional harmonic holographic microscopy using nanoparticles as probes for cell imaging. Optics Express 17, 2880–2891 (2009).
5. Dadap JI, Shan J, Eisenthal KB, Heinz TF. Second harmonic Rayleigh scattering from a sphere of centrosymmetric material. Physical Review Letters 83, 4045–4049 (1999).
6. Hsieh CL, Pu Y, Grange R, Psaltis D. Second harmonic generation from nanocrystals under linearly and circularly polarized excitations. Optics Express 18, 11917–11932 (2010).
7. Jones TB. Basic theory of dielectrophoresis and electrorotation. IEEE Engineering in Medicine and Biology Magazine 22, 33–42 (2003).
8. Miller RD, Jones TB. Electro-orientation of ellipsoidal erythrocytes. Biophys. J. 64, 1588–1595 (1993).
9. Fluck D, Gunter P. Second harmonic generation in potassium niobate waveguides. IEEE Journal of Selected Topics in Quantum Electronics 6, 122–131 (2000).
10. Wooten EL, Kissa KM, Yi-Yan A, Murphy EJ, Lafaw DA, Hallemeier PF, Maack D, Attanasio DV, Fritz DJ, McBrien GJ, Bossi DE. A review of lithium niobate modulators for fiber-optic communication systems. IEEE Journal of Selected Topics in Quantum Electronics 6, 69 (2000).
11. Schwesyg JR, Eggert HA, Buse K, Sliwinska E, Khalil S, Kaiser M, Meerholz K. Fabrication and optical characterization of stable suspensions of iron or copper doped lithium niobate nanocrystals in heptanes. Applied Physics B—Lasers and Optics 89, 15 (2007).
12. Niederberger M, Pinna N, Polleux J, Antonietti M. A general soft chemistry route to perovskites and related materials: syntehsis of barium titanate, barium zirconate and lithium niobate nanopartiocles. Angewandte Chemie—International Edition 43, 2270 (2004).
13. Wang LH, Yuan DR, Duan XL, Wang XQ, Yu FP. Synthesis and characterization of fine lithium niobate powders by sol gel method. Crystal Research and Technology 42, 321 (2007).

14. An CH, Tang KB, Wang CR, Shen GZ, Jin Y, Qian YT. Characterization of lithium niobate nanocrystals prepared via a convenient hydrothermal route. Materials Research Bulletin 37, 1791 (2002).

15. Magrez A, Vasco E, Seo JW, Dieker C, Setter N, Forro L. Growth of single crystalline potassium niobate nanostructures. Journal of Physical Chemistry B 110, 58 (2006).

16. Zhao LL, Steinhart M, Yosef M, Lee SK, Schlecht S. Large scale template assisted growth of lithium niobate one dimensional nanostructures for nano sensors. Sensors and Actuators B—Chemical 109, 86 (2005).

17. Wood BD, Mocanu V, Gates BD. Solution phase synthesis of crystalline lithium niobate nanostructures. Advanced Materials 20, 4552 (2008).

18. Hsieh CL, Grange R, Pu Y, Psaltis D. Three dimensional harmonic holographic microscopy using nanoparticles as probes for cell imaging. Opt. Express 17, 2880 (2009).

19. Choi JW, Pu A, Psaltis D. Optical detection of asymmetric bacteria utilizing electro orientation. Optics Express 14, 9780 (2006).

20. Green NG, Morgan H. Dielectrophoretic investigations of submicrometre latex spheres. Journal of Physics D—Applied Physics 30, L41 (1997).

21. Burke PJ. In Encyclopedia of Nanoscience and Nanotechnology (edited by Nalwa, HS.). 6, 623 (2004).

22. Markx GH, Dyda PA, Pethig R. Dielectrophoretic separation of bacteria using a conductivity gradient. Journal of Biotechnology 51, 175 (1996).

23. Keshoju K, Xing H, Sun L. Magnetic field driven nanowire rotation in suspension. Applied Physics Letters 91 (2007).

24. Li MW, Bhiladvala RB, Morrow TJ, Sioss JA, Lew KK, Redwing JM, Keating CD, Mayer TS. Bottom-up assembly of large-area nanowire resonator arrays. Nature Nanotechnology 3, 88 (2008).

25. Pantazis P, Malone J, Wu D, Fraser SE. Second harmonic generating (SHG) nanoprobes for in vivo imaging. PNAS 107, 14535–14540 (2010).

26. Nystrom T. Aging in bacteria. Curr Opin in Microbiology 5, 596–601 (2002).

27. Stewart EJ, Madden R, Paul G, Taddei F. Aging and death in an organism that reproduces by morphologically symmetric division. PLoS Biol 3, 295–300 (2005).

28. Park H, Pontius W, Guet CC, Mark JF, Emonet T, Cluzel P. Interdependence of behavioural variability and response to small stimuli in bacteria. Nature 468, 819–823 (2010).

VI. Conclusion/Outlook

In this thesis, we have explored the possibility of manipulating surfaces within the concept of optofluidics for biosensor applications. These techniques have been applied to the study of many bacteria in liquids, as well as proposed for the study of single bacterium in varying environments. The techniques are developed from various topics: application of external electrical fields, heating through plasmonic optofluidics, and imaging with second harmonic probes. Compartmentalization of biological detection from the optics and electronics allows for the creation of a use-once-and-throw-away lab-on-a-chip biosensor. However, within microfluidics, there is a concept of moving from the study of bacteria in the bulk liquid to the idea of studying the behavior of a single bacterium. Miniaturization of the fluidic control through plasmonic optofluidics offers great flexibility and adaptability, eliminating the necessity of prepatterning of specific valves. The necessity of imaging the long term behavior of bacterium results in the need for new types of probes. Finally, a method to manipulate the light source is proposed. In all these concepts, the adaptability of surfaces in optofluidics presents great flexibility and variability in the types of technologies that may be controlled. However, there is still a key weakness in that these components must communicate through external electronic means, whether to control the laser position and intensity, provide decision making regarding bacteria detection, detect the second harmonic, or in the activation of electric fields for the purposes of applying electrowetting, electro-orientation, and dielectrophoretic forces. Further work will be needed to provide the necessary framework

for constructing a truly self-contained lab-on-a-chip system that is a handheld mobile, portable device.

Appendix

A. Making superhydrophobic surfaces

1. Clean substrate (acetone, methanol or isopropanol, and deionised water). If substrate is of oxide, skip to step 5.
2. Spincoat Honeywell Spin-on-glass xx1 at 3 krpm.
3. Using the annealer, in a nitrogen filled environment, heat the substrate to 425 °C. This will be done in stages as to prevent thermal shock. Heat to 85 °C, let it remain stable for 1 minute, next at 150 °C, then at 250 °C, and then finally 425 °C for 1 hour.
4. Turn off the heater. The solvent in the SOG will have evaporated and there should be a ~ 100-nm-thick oxide layer covering the substrate. Let it cool.
5. Spincoat fluoropolymer adhesion promoter at 2 krpm. The promoter contains two different ends, one of silane and the other is fluorine. The silane will stick to the oxide surface and the fluorine will bond with the fluorine in the fluoropolymer.
6. Heat at 80 °C for 30 minutes. This is an annealing step which causes a monolayer to form. Remove excess using soapy water and gentle scrubbing. Clean with deionised water.
7. Spincoat Teflon AF solution. For ~ 1-micron-thickness, mix 0.5–1% Teflon AF 1600 by weight in fluorinated solvent, usually Fluorinet FC-40 or FC-75. Different thickness layers can be achieved by mixing different amounts of the solid fluoropolymer in the fluorinated solvent.
8. Heat at 200 °C for 1 hour. This will remove the solvent in the mixture and anneal the Teflon layer.
9. For plastic substrates, lower temperatures can be substituted with longer baking times to remove the solvent, or different solvents with lower evaporation

temperatures may be used. Normally, the surfaces end up being rougher due to the lack of an annealing process, resulting in greater hydrophobicity.

B. Photolithography

1. Prepare substrate by cleaning with acetone and methanol or isopropanol, followed by a wash in deionised water. Substrate is heated to 200 °C.
2. Treat with hexamethyldisiloxane vapor for 1 minute to improve adhesion with positive photoresist (SPR220-7 or S18xx series).
3. Spin photoresist at appropriate speeds to achieve required thickness. SPR220-7 results in an approximately 7-micron-thick resist layer. S18xx results in an approximately x.x-micron-thick resist layer, i.e., S1813 is approximately 1.3 microns thick and S1805 is approximately 0.5 microns thick. For SU8-2xxx, it results in approximately xxx-micron-thick layer, i.e., SU8-2010 is 10-microns-thick and SU-2001 results in a 1-micron-thick layer. For the Gerstelec GM 10xx photoresists, a look up table was utilized to create thicknesses of 0.1 micron to 100 microns thick.
4. Soft bake the photoresist such that a significant amount of the solvent in the photoresist evaporates. The solvent is utilized to reduce the viscosity of the liquid which allows creation of a thinner layer when spinning the photoresist on the substrate.
5. Expose the substrate with the photoresist with a mask aligner to ultraviolet light using a mask with patterns marked by dark and clear areas. Time is dependent on thickness of the photoresist layer and the light intensity.
6. For negative photoresists (SU8-2xxx or Gerstelec GM 10xx), post bake the mold. The exposed regions of the photoresist will be resistant to most chemical solvents, becoming similar to glass.
7. Develop the sample. This causes exposed regions to dissolve for positive photoresists whereas unexposed regions dissolve for negative photoresists.
8. After development, the mold is hard baked. This is done at a temperature such that the mold can slightly reflow. This can result in rounded corners, especially for positive photoresists.

C. Polydimethylsiloxane chip manufacture

1. Expose the mold to methyltrichlorosilane vapor for several minutes. This creates a monolayer on the mold which prevents adhesion of polydimethylsiloxane to the mold.
2. Mix 10 parts of GE RTV A to 1 part of GE RTV B (can use Sylgard 184 polymer and curing agent instead).
3. Pour the mixture onto the mold and use a vacuum to eliminate all air bubbles on the mold.
4. Bake for at least 30 minutes at 80 °C or 2 hours at 60 °C. Playing with the temperature is useful as it controls the amount of contraction the PDMS will experience in the oven with respect to room temperature.
5. Afterwards, remove the PDMS from the mold. Cut the devices with a knife. Punch holes with the punch tool from Technical Innovations.
6. Attach device to substrate and bake overnight. Otherwise, an oxygen plasma machine can be utilized to improve adhesion between the PDMS and substrate. Expose the PDMS to oxygen plasma for 20–30 seconds then immediately stick the PDMS chip and substrate together. Within a few minutes, permanent bonds should occur within the PDMS and substrate. This works especially well for glass or other PDMS surfaces. Metals and Teflon in general have very poor adhesive behavior in any of these methods.

D. Silver nanoparticle synthesis

1. AgNO3 or AgClO4 is dissolved in deionized H2O to create 0.03 M Ag+ solution and vigorously stirred.
2. This is mixed with chloroform containing phase transfer catalyst 0.2 M (C8H17)4NBr and stirred for 1 hour. Afterwards, the organic phase (chloroform) contains the silver ions, phase-separated from the aqueous phase (deionised water).
3. The surfaces of the silver ions are functionalized with dodecanethiol (1 mmol).
4. The silver ions are reduced by introducing 0.44 M NaBH4 to create the silver nanoparticles, and stirred for several hours.
5. Size-selective precipitation of the nanoparticle solution is used to reduce the size distribution of the nanocrystals.

E. Gold nanoparticle in micelle synthesis

1. P(S-2VP) is added to toluene and stirred vigorously. By picking the proper lengths for the styrene and vinyl-pyridine, the inner micelles are approximately 15 nm large and spaced 45 nm apart from each other.
2. HAuCl4.3H2O is added to this solution. The hydrophilic portion (vinyl pyridine) is replaced by the gold ions.
3. When this solution is spin coated or dip coated on to the substrate, the micelles form a monolayer of evenly spaced micelles.
4. The resulting polymers may be removed by oxygen plasma. This results in the gold ions remaining and reducing to form gold nanoparticles approximately 15 nm in diameter.

F. Gold nanoparticle synthesis

1. HAuCl4.3H2O is added to water to obtain the gold ions. NaBH4 is added to water to create the reducing agent.
2. The solution containing gold ions is heated to 100 °C and mixed vigorously.
3. The reducing agent is dropped into the gold ion solution and left to mix for 15 minutes. The ratio of gold ions to reductant determines the size of the gold nanoparticles.